THE UNIVERSITY OF CHICAGO

ALL-OPTICAL THIN FILM GATING WITH OXIDE SEMICONDUCTORS

A DISSERTATION SUBMITTED TO
THE FACULTY OF THE PRITZKER SCHOOL OF MOLECULAR ENGINEERING
IN CANDIDACY FOR THE DEGREE OF
DOCTOR OF PHILOSOPHY

BY
ERZSEBET CASS VINCENT

CHICAGO, ILLINOIS
DECEMBER 2021

There are burdens we must sometimes face that seem too much to bear:
they tear us up and drag us down, leave us the worse for wear;
there were so many days I thought I'd never get this far,
so when you're lying in the gutter, please keep looking at the stars.

**With apologies to Oscar Wilde for lifting the last line*

Table of Contents

LIST OF FIGURES vii

LIST OF TABLES ix

ACKNOWLEDGMENTS x

ABSTRACT xii

1 INTRODUCTION 1

2 FUNDAMENTAL SCIENTIFIC CONCEPTS 4
- 2.1 Introduction 4
- 2.2 Atoms and Electrons 5
- 2.3 Photons 9
- 2.4 Bonding 11
- 2.5 Crystal Lattices 13
  - 2.5.1 Explanation of Lattices 14
  - 2.5.2 Allotropes 14
  - 2.5.3 Crystal Orientation 15
  - 2.5.4 Defects 17
  - 2.5.5 Diffusion 18
  - 2.5.6 Annealing 19
- 2.6 Kinetic and Potential Energy 20
- 2.7 Current, Voltage, and Resistance 21
  - 2.7.1 Superconductivity 22

3 SEMICONDUCTOR PHYSICS 24
- 3.1 Band Structure 24
  - 3.1.1 Valence and Conduction Bands 25
  - 3.1.2 Band Gaps 25
  - 3.1.3 Direct vs. Indirect Band Gaps 26
  - 3.1.4 Dirac Cones 27
- 3.2 Fermi Level/Chemical Potential 27
  - 3.2.1 Work Function 28
  - 3.2.2 Electron Affinity 29
  - 3.2.3 Band Bending 29

3.2.4 Two-Dimensional Electron Gas . . . 30
3.3 Charge Carriers . . . 30
3.3.1 Electrons and Holes . . . 30
3.3.2 Mobility and Carrier Concentration . . . 31
3.3.3 Defect States . . . 32
3.3.4 p-, i-, and n-type materials . . . 33
3.3.5 p-n junctions . . . 33
3.4 Field-Effect Transistors . . . 34

4 MATERIALS . . . 35
4.1 Strontium Titanate . . . 35
4.1.1 Basics of STO . . . 35
4.1.2 Defects in STO . . . 37
4.1.3 Photo-Induced Effects in STO . . . 39
4.1.4 Impacts of Annealing on STO . . . 41
4.2 Two-Dimensional Materials . . . 42
4.2.1 Graphene . . . 43
4.2.2 Transition Metal Dichalcogenides: MoS_2 . . . 44
4.2.3 Other Materials . . . 46
4.3 Heterostructures . . . 46

5 TECHNIQUES . . . 49
5.1 Optical Gating . . . 49
5.1.1 Introduction . . . 49
5.1.2 Proposed Mechanism . . . 51
5.1.3 Optical Gating: A Literature Review . . . 53
5.2 Kelvin Probe Force Microscopy . . . 57
5.2.1 Mechanism . . . 57

6 OPTICAL GATING MEASUREMENTS . . . 61
6.1 Introduction . . . 61
6.2 Measurements . . . 62
6.3 Graphene . . . 63
6.3.1 Characterization . . . 63
6.3.2 Electrical Gating . . . 65
6.4 MoS_2 . . . 67
6.4.1 Characterization . . . 67
6.4.2 Persistence . . . 71
6.4.3 Ultraviolet Power Dependence . . . 73
6.4.4 Ultraviolet and Red Stepping . . . 75
6.4.5 Electrical Gating . . . 77
6.4.6 Mobility and Carrier Concentration Calculations . . . 79
6.4.7 Temperature Sweep . . . 80
6.5 Analysis . . . 82

7 KELVIN PROBE FORCE MICROSCOPY MEASUREMENTS 87
7.1 Introduction 87
7.2 Samples 88
7.3 Set-Up 88
7.4 Spatial Measurement of Contact Potential 89
7.5 Ultraviolet Dose Dependence 90
7.6 Comparison of Different Annealing Conditions 92
7.7 Comparison of Different Samples Under Annealing 95
7.7.1 Change in Absolute Contact Potential 97
7.7.2 Peak During Ultraviolet Excitation 101
7.7.3 Change in Contact Potential Before/After Illumination 103
7.7.4 Discussion of Iron-Doped Sample 103
7.7.5 Visual Differences Due to Annealing 104
7.7.6 Comparison with Literature Density Functional Theory Calculations 105
7.8 Effect of Red Illumination 107
7.9 Comparison of Different Crystal Orientations 109
7.10 Measurements of Graphene on STO 110
7.10.1 Spatial Measurement of Graphene on STO 110
7.10.2 Single-Point Measurements of STO and Graphene 111
7.10.3 The Effect of Red Illumination on Graphene 112
7.11 Analysis 114
7.12 Calibrations and Controls 119
7.12.1 Tip Calibration 119
7.12.2 Discounting Tip Interference 120
7.12.3 Confirming the KPFM Mathematical Model 122

8 CONCLUSIONS 124

9 IDEAS FOR FUTURE WORK 129
9.1 All-Optical Control of the T_c of FeSe/STO 129
9.2 Looking for Other Substrates 130
9.3 Gating van der Waals Heterostructures 132

REFERENCES 135

List of Figures

4.1 Crystal structure of strontium titanate 36

5.1 Figure depicting the mechanism of the KPFM technique 58

6.1 Photographs of MoS_2 and graphene samples 63
6.2 Graphene response to optical gating 64
6.3 Graphene response to electrical gating 66
6.4 MoS_2 response to optical gating 67
6.5 MoS_2 photocurrent onset 68
6.6 MoS_2 current decay after ultraviolet illumination cessation 69
6.7 MoS_2 current decay during red illumination 70
6.8 16 hour persistence of MoS_2 current 72
6.9 MoS_2 persistent current decay exponential fit 73
6.10 MoS_2 ultraviolet power density dependence 74
6.11 MoS_2 current stepping to ultraviolet and red illumination 76
6.12 MoS_2 response to electrical gating 78
6.13 MoS_2 ON and OFF state responses to temperature sweep 81

7.1 KPFM spatial measurements of STO surface potential in response to ultraviolet illumination 90
7.2 Ultraviolet dose dependence of contact potential response 91
7.3 Plot of KPFM response to ultraviolet pulse and absorption spectra for different annealing conditions 94
7.4 Ultraviolet pulse sequence for Samples 3, 4, and 5 96
7.5 Measured response of contact potential to ultraviolet pulse for different samples and different annealing conditions 98
7.6 Visual differences of STO samples due to annealing 104
7.7 Contact potential response to red illumination 108
7.8 Comparison of ultraviolet response for different crystal orientations 109
7.9 KPFM spatial image of graphene on STO 110
7.10 Contact potential response of graphene and STO to ultraviolet illumination . . . 111
7.11 Response of graphene contact potential to ultraviolet and red illumination . . . 113
7.12 Cartoon depicting hypothesized band bending during optical gating 115
7.13 Cartoon depicting hypothesized defect responses to different annealing conditions 117
7.14 Calibration of contact potential to work function 120

7.15 Comparison of contact potential as a function of different liftoff heights and measurement frequencies 121

List of Tables

7.1 Samples and annealing conditions used for multi-sample annealing study 95

Acknowledgments

I would like to acknowledge the endless support which has been provided by my parents, Kimberly Cass and Stephen Vincent, and my sister Alexia, as well as my brother-in-law Marcus, throughout my life and educational career. Their help, love, and encouragement has been crucial to my graduate experience, as well as to my growth as a human being. I am truly blessed to call them my family.

Friends have been critical in keeping a good sense of work-life balance throughout my graduate career, and particularly in keeping me grounded during the composition of my thesis. Accordingly, I would like to acknowledge by name a few of the friends who have made the last few years not only academically productive, but also personally vibrant: Victoria, Wil, Cristiana, Yoni, Elle, JJ, Nik, Patrick, Ishaan, Lexi, Tom, Arohan, Johannes, Aron, Sumiah, Mario, Sircedrick, Sasha, and David. I would also like to specifically thank my best friend, Courtney, who has been a rock of support through tough times and kept me artistically active even in the thick of a STEM education.

There are too many teachers for me to name here, at every level, who have guided me throughout my education. It is through their dedication that I have been able to learn and grow within an academic context. I am deeply grateful for all their instruction, help, and inspiration; it is my dream to someday live up to their excellence as educators.

I have had the privilege of working within the Awschalom lab for the last decade. Passion, dedication, intelligence, and kindness have been ubiquitous for each and every member of this group that I have known, and I have learned so much from all of them.

Viva Horowitz, my first mentor in the group, provided me an excellent role model during my earliest forays into experimental science. During the research which forms the body of this thesis, I had the wonderful opportunity to work closely with and learn from Andrew Yeats and Joost van Bree, both of whom have taught me not only how to study the optical gating effect on strontium titanate, but also how to be a more thoughtful and analytical scientist in general. Their advice and instruction has been enormously helpful in shaping my approach to research. I would particularly like to thank Joost for providing excellent feedback and discussion during the composition of this thesis which greatly contributed to the final product, as well as several cartoons used throughout this text. I would also like to thank Chris Anderson, Joe Heremans, Paul Jerger, Elena Glen, and Pratiti Deb for helping to proofread this thesis and design my defense presentation. I additionally acknowledge the constant administrative guidance of Mary Pat McCullough throughout my graduate career.

I furthermore thank my collaborators Meng Ye, Kan-Heng Lee, and Hui Gao for providing their insight, talent, and time to the projects described in this work. I additionally thank the members of my committee: Andrew N. Cleland, Giulia Galli, and Jiwoong Park - it has been an honor to have my work evaluated by such esteemed scientists.

Finally, I would like to acknowledge and thank my advisor, David Awschalom. He has provided me with great inspiration and guidance throughout my entire higher educational career, and has been endlessly supportive of me throughout periods of success and adversity alike. His mentorship has been critical to developing my research and my broader career. I could not have asked for a better advisor, and I am forever grateful for the direction, encouragement, and opportunities with which he has provided me over the last ten years.

Abstract

With the rise of two-dimensional materials, there has been a need to find techniques which fully harness these materials' unique properties. One important way to control these materials is via manipulation of their Fermi levels. A novel effect enables all-optical persistent bidirectional control of thin film materials' Fermi levels when they are placed on a strontium titanate substrate and stimulated with light with energy either above (ultraviolet) or below (red) strontium titanate's band gap. I present work using this optical gating technique to bidirectionally control the Fermi level of graphene and molybdenum disulfide, and show that this method corresponds to electrical backgating. Furthermore, I present research utilizing Kelvin probe force microscopy to investigate the work function response of bare strontium titanate to ultraviolet illumination, and to show how iron doping and different annealing conditions impact this response. These results demonstrate the applicability of this technique to diverse two-dimensional material systems, and provide new insight into a non-invasive method of Fermi level control which could prove useful for emerging applications.

Chapter 1

Introduction

One of the most amazing things about working in experimental science is the accidental discovery of entirely new phenomena, which had not previously been anticipated by theory and thus demand novel explanations after the fact. These discoveries give us new unexpected insights into the workings of different material systems, and frequently provide the venue for exciting new technologies.

A perfect example of such an accidental discovery is that of the so-called "optical gating" phenomenon in strontium titanate [1]. It was experimentally discovered that when a thin film of material is placed on strontium titanate, shining different colors of light onto the structure can persistently change the conductivity of the thin film. This discovery was not only theoretically unexpected, but opened the doors to an entirely new way of manipulating thin films.

The optical gating effect, where the strontium titanate substrate is made into an effective backgate in response to optical stimulation, will be explained in far greater depth throughout the body of this thesis. However, to initially motivate this work, I will provide a brief and simplistic summary: when a two-dimensional or thin film material is placed onto a strontium titanate substrate, its electronic properties (specifically, the Fermi level) may be controllably changed by the application of different colors of light above versus below the

strontium titanate band gap energy (in this work, ultraviolet versus red). These changes are persistent in the absence of illumination, instead of transiently depending on active illumination. Although its identity is unknown, some defect in strontium titanate is presumed to be responsible for this effect.

This technique has been utilized on a handful of materials by a handful of authors (as will be discussed in Section 5.1.3). In order to shed more light on this effect, this thesis investigates how two other materials (graphene and MoS_2) may be controlled by using this technique. Optical gating is shown to be equivalent and additive to electronic gating of these material, and to provide a persistent relative change in Fermi level after illumination has ceased which can survive large changes in temperature. This work has demonstrated the effectiveness of optical gating in manipulating the electronic properties of these materials. By analyzing the results of these experiments in comparison with the literature, this thesis provides a more detailed description of how the optical gating technique affects several classes of materials.

Additionally, since this effect is fundamentally due to the substrate, this work encompasses a separate set of experiments investigating how light affects bare strontium titanate to create this effect. Kelvin Probe Force Microscopy is used to observe the difference in strontium titanate's work function (and by extension, Fermi level) produced by ultraviolet light. The effect was demonstrated on standard samples and shown to occur regardless of crystal orientation. Further measurements upon differently-prepared samples annealed at different temperatures in oxygen-rich and oxygen-poor environments, as well as samples with additional iron doping, demonstrated how those preparations affected the response. These measurements also directly assessed the effect's impact on a two-dimensional material (graphene) on top of the substrate, as well as the substrate beneath it, during and after illumination, thus providing greater insight into both components in the combined effect.

Thus, given a unique and novel effect, I have endeavored to better characterize its potential applications in different material systems, and furthermore investigated the un-

derlying cause of this intriguing phenomenon. I hope this thesis will help inform scientists looking for practical non-invasive ways to control two-dimensional systems; give a more complete picture of the phenomenon as a whole to those who are generally interested in the many unusual properties of strontium titanate; and inspire continued research into this topic. Additionally, I hope it proves interesting and enlightening for you, the reader, regardless of what previous scientific background you have.

Chapter 2

Fundamental Scientific Concepts

2.1 Introduction

This chapter has been written in the interest of making this dissertation as accessible as possible to the greatest number of readers, regardless of scientific background (or lack thereof). Scientific communication to lay audiences is something I very passionately feel is critical to creating a more well-educated and technologically thoughtful public, so it is my desire to reflect this in my thesis by utilizing a "ground-up" approach in its conceptual building. Thus, this chapter will lay out the most fundamental and broad science upon which I believe further understanding should be based, and is intended to enable understanding of this work as a whole by readers unfamiliar with science. The following chapter will focus in on the basics of semiconductor physics, giving greater focus to explaining more technical aspects of the science directly related to this work.

The bulk of the material that will be discussed in these two chapters is fairly fundamental, and has been taught to me many times by many different teachers and through many different books, articles, talks, and so forth. Thus, the vast majority of this is written from my own accumulated understanding. This chapter was composed with reference to Callister and Rethwisch's **Materials Science and Engineering: An Introduction** (10^{th} Edition)

[2].

2.2 Atoms and Electrons

Before we begin to delve into the more complex physics which forms the backbone of this dissertation, it is useful to start at the most fundamental level: the humble atom. Atoms are the building blocks of matter. They are composed of two parts: a nucleus and an electron cloud. Within the nucleus, two species exist: protons and neutrons. The number of protons within a nucleus determine which chemical species, be it carbon or gold or anything else on the periodic table, the atom is. Each proton also imparts a positive charge of +1 to the nucleus; since neutrons have no charge, the nucleus is therefore positively charged. Nuclei are incredibly small.

Surrounding the tiny nucleus is a vast cloud of electrons; they take up the overwhelming majority of the cited "volume" of an atom, and the average radius of this cloud determines the radius of an atom as typically described. Each electron has a charge of -1; however, instead of being tightly confined to one location as the protons are, the electrons are free to move throughout space, even as they are generally electrostatically attracted to the positively-charged nucleus. However, electrons are also critically governed by a property called spin. Spin is a purely quantum parameter which governs the way in which the electron behaves in the presence of a magnetic field. We take an electron's spin as an intrinsic property.

What do I mean when I say that spin is purely quantum? The word "quantum" itself derives from the term "quantized": that is, having discrete values. For classical values, we are familiar with things taking on continuous values: a ball of material could have a mass of 1 kg, or 1.1 kg, or 1.01 kg, with finer delineations possible the more sensitive you allow your measurement to be. This is not the case for quantized properties in quantum mechanics: they are limited in which values they can take, and which values they are allowed to take on depends entirely on the parameter itself, as well as which particle we are looking at.

For an electron, spin may take the value of $+\frac{1}{2}$ or $-\frac{1}{2}$ ("spin up" or "spin down"). Because this quantity takes a half-integer value, electrons are called "fermions"; quantum mechanical rules for fermions insist that two electrons may not occupy an identical "state".

It is important to define what we mean by a state. Speaking very loosely here, we may describe a state as an accumulation of all of the relevant parameters for the electron that allow us to exactly describe it. Its charge is not such a parameter - electrons all have the same charge. Instead, in addition to spin m_s, there are three different parameters which every electron in an atom possesses. By specifying all four of these parameters, we are able to uniquely define a single electron, since only one electron in an atom may have that particular combination of the four parameters.

First, there are several different "shells" of electrons in orbit, which one can think of analogistically as equivalent to concentric spherical shells around the nucleus. What shell an electron belongs to is defined by the quantum number n. The maximum value this number can take for a given atom is identical to the number of the row on the periodic table to which the element belongs (with the top row, composed of hydrogen and helium, having n=1). These different shells represent how close the electrons are, on average, to the nucleus, with increasing values of n representing greater average distance (note that as the distance from this average radius increases, the probability of finding an electron trails off towards zero – it is incredibly improbable to find a single atom's electron very far from the nucleus). Thus, n represents the radial component of an electron's wave function (where a wave function is, to simplify for this specific context, a mathematical expression revealing where an electron may be found in space with respect to the nucleus; the radial component specifies how far away it is).

Interestingly, when one mathematically derives the radial expression for these wave-functions, it turns out that there are radii that an electron is forbidden from occupying (that is, there is no probability they will be found at that distance from the nucleus) – the number of these forbidden radii (which are referred to as nodes) is n-l-1 (we will discuss l in the

next paragraph), noting that there is also by default (for all orbitals) an additional forbidden radius at r=0, the location of the nucleus (since the electron is never inside the nucleus), and that the probability of finding an electron at a given r also goes to zero as r goes to infinity. As the value of n increases, the amount of energy required to keep an electron in orbit around the nucleus also increases correspondingly (the states are "higher energy"), since when the electron is on average further away, it will on average be less strongly electrostatically attracted to the nucleus. Thus, they are more easily pulled out of orbit. The electrons furthest away on average – that is, those with the highest value of n – are therefore largely those that participate in bonding due to this reduced attraction, and are referred to as "valence" electrons.

However, not all orbitals are made equal. The general toy picture of an atom, widely portrayed in popular media, has a (usually quite proportionally large) nucleus surrounded by a number of electrons in circular orbits at a neat constant distance. In fact, this is not accurate: the shape of the space which an electron is allowed to occupy is dependent on the angular momentum it possesses, as represented by the quantum number l. This number (and its associated number m_l, defined in the paragraph to follow) define the angular component of an electron's wave function. l may take any value from 0 to n-1 for the particular value of n which describes that electron – that is to say, the quantum number n determines the shapes of space that the electrons with that number can occupy. What shape exactly the orbital takes is dependent on the value of l: when l=0, for instance, the orbital is completely symmetric and resembles a sphere centered on the nucleus, which is often referred to as an s orbital; when l=1, the so-called p orbitals, the orbital takes a form which may be compared to a dumbbell or perhaps to two balloons tied together. Such an orbital is clearly not totally symmetric, necessarily lying along one axis (the axis of the dumbbell bar); thus, there is an angular momentum intrinsic in its shape. In addition to radial nodes, angular nodes also exist; these forbidden regions generally take the form of planes (or sometimes conical surfaces), and each electron's wave function possesses a total of l such nodes.

Now, we experience space in not one but three dimensions, generally termed x, y, and z in a scientific context. These directions are all perpendicular to each other (giving six independent directions relative to anything, including you: we intuitively think of these as up, down, left, right, forward, behind). Thus, as there are three axes, and none is "special" when it comes to the point of view of the nucleus (which we treat as a single point in space at the intersection of all three axes), we can imagine three p orbital dumbbells all perpendicular to each other lying along each of these axes (a dumbell head pointing in each of the six directions). These are differentiated p_x, p_y, and p_z; which axis is which is arbitrary, although often when it comes to interatomic interactions, p_x and p_y are treated as the orbitals in-plane of a given interaction.

How do we distinguish these three different orbitals, which all have (at least with no other interactions) identical angular momentum? The magnetic quantum number m_l is used, which describes an orbital's orientation in space. m_l may take any integer value ranging from -l to +l, so for the dumbbell p orbitals, we have -1, 0, and 1: three values, for each of the three axes in this case. Notice that when l=0, m_l is necessarily zero: there is only one value available.

Of course, one may think of increasingly high values of n, and thus l, and thus more available values of m_l, existing (this greater availability of m_l values necessitating the more complex geometries of higher l value orbitals, which have distinct shapes for different values of m_l, as the different m_l suborbitals may not identically lie on top of each other). The first example of this is the d orbitals, which have five different configurations. These are technically not all in different spatial directions (since that is impossible in three-dimensional space); instead they have very different shapes. These orbitals begin to be filled on the fourth line of the periodic table, although they belong to the energy level n from the row above, thus lying beneath the valence s and p shells. The subsection of the periodic table where the s-orbital is full and d-orbitals are being filled contains the so-called transition metals.

Note that different values of m_l may not have identical energies (that is to say, an

electron may need to have a higher amount of energy to have that value of m_l), particularly for orbitals where l>1: outside influences such as an electric field may result in some of these orbital geometries having higher energy than the others with their same l value, a phenomenon referred to as crystal field splitting. This effect is frequently observed with d-orbital electrons in the transition metals.

Finally, we consider spin, given the quantum number m_s. As mentioned before, an electron may either have a spin of $+\frac{1}{2}$ or $-\frac{1}{2}$; since these are the only two possible numbers, up to two electrons may occupy any orbital with a given value of n, l, and m_l. By default, each individual electron (if there are equal or fewer available electrons in an l orbital compared to the number of m_l states) will prefer to occupy its own orbital (a principle known as Hund's rule); however, if there is a large energy difference between different m_l states (that is, if there is a large extent of crystal field splitting), electrons with different spin will double up as they are added to the atom before filling those higher energy states. An electron's state is intrinsically defined by the combination of these four quantum numbers. Therefore, no two electrons in a given atom may share identical values for all of these number.

2.3 Photons

Photons are the quantum (or smallest divisible particle) of light. The reader may be familiar with the concept that light is both a particle and a wave; in correspondence to this, photons travel through space with an associated wavelength (or, conceptually equivalently, a frequency: the wavelength measures the length between peaks of a wave, while the frequency measures how frequently those peaks occur). This wavelength is inversely related to the energy of the associated photon, according to

$$E = \frac{hc}{\lambda}$$

where E is the photon's energy (typically in units of eV) and λ is the corresponding

wavelength (in units of nm for the wavelengths that will be discussed in this work). (Note that h is the Planck's constant and c is the speed of light, both constants; in the chosen units, the quantities multiply together to give the value 1240 eV·nm.) It is this wavelength λ which determines the color of visible light, which ranges from 400 nm (often referred to as blue; visually purple; approximately 3.10 eV) to 700 nm (red; approximately 1.77 eV). This range of wavelengths roughly account for the visual spectrum (human eyes can see slightly further in both directions, the extent being individually determined). This range of colors appears exactly as seen in a rainbow, which indeed results from droplets of water refracting the white light of the sun (with "white light" being a combination of photons with all the wavelengths) so that photons with different wavelength exit the droplets at different angles, resulting in these different colors being visually separated.

Observe that due to their inverse relationship, a high wavelength corresponds to relatively low energy, and vice versa. However, a photon's possible wavelength does not start and stop at the visible spectrum, because the true spectrum of light extends far above and below what we can see: with wavelengths lower than 400 nm (energies above 3.10 eV), we move into the ultraviolet region, whereas with wavelengths above 700 nm (energies below 1.77 eV), we move into the infrared regime.

Photons have no mass, hence why they travel at the speed of light. The speed of light is the maximum possible speed for anything to travel at, and is only attainable by massless particles.

Unlike electrons, photons possess integer spin (which may take values of +1, 0, or -1); due to this integer spin, they are referred to as bosons. In contrast to fermions, it is perfectly allowable for bosons to occupy identical quantum states; thus, there is no need for photons traveling together to adopt the sorts of complex configurations which electrons take on. We can imagine a light source as pouring a bunch of photons onto whatever it is shining on in the same way a bucket would pour water onto a surface.

2.4 Bonding

There are generally recognized to be five different ways in which atoms may bind to each other: covalent, ionic, metallic, hydrogen, and van der Waals (with the latter two, much weaker, being termed secondary bonding). I will briefly describe each type of bond to provide clarity, although the types most significant to this work are ionic, covalent, and van der Waals.

Ionic bonding occurs when two elements with substantially different electronegativities interact, and is the first type of bonding many of us learn about in chemistry classes. Electronegativity characterizes the tendency of an atom to either gain (high) or lose (low) electrons in interaction with other elements: an atom with almost a full valence shell will desperately want to gain electrons to stabilize itself, whereas an atom with an almost-empty valence shell would prefer to lose electrons, leaving a complete inner shell (or, in the case of hydrogen acting as an electron donor, leaving the bare nucleus). In general, across the periodic table, elements further to the right (possessing more electrons in their outer valence shell) and further to the top (possessing a smaller outer electron shell, with electrons pulled closer to the nucleus) will have higher electronegativities; elements for which the reverse is true tend to have lower electronegativities.

Initially, when the number of electrons matches the number of protons in an atom, it will have a neutral charge. However, when an atom with a high electronegativity interacts with an atom of significantly lower electronegativity, it is able to pull off one or more electrons from the latter and add them to its own outer shell in an attempt to fill its valence shell. Once this is accomplished, the two atoms each take on an electric charge (becoming "ions") due to the gain or loss of electrons relative to the constant number of protons. Accordingly, they now interact via electrostatic forces that attract positive and negative charges to each other. This attraction creates an ionic bond.

Covalent bonding occurs between two atoms of similar electronegativity. In such a case, one atom is not able to "pull" the electron(s) off the other; instead, they are shared

between the atoms. This essentially allows both atoms to functionally add an additional electron to their outer shell, bringing them closer to the possession of a full valence shell. In this circumstance, neither of the two becomes an ion, but they share electrons between them. This sharing will be equal for atoms of equal electronegativity; the more different the electronegativities of the atoms, the stronger the more electronegative one will relatively pull on the electron.

Metallic bonding occurs only in species composed of one or more metal elements (where metals are delineated as on most periodic tables). In metallic bonding, unlike the previous two forms, the valence electrons of bound atoms are delocalized from their respective atoms and are able to freely travel about through the material. This helps create the high conductivity typically associated with metals.

An important note is that while ionic, covalent, and metallic bonding have been described as seemingly totally distinct, in reality there is a bit more of a spectrum. Two non-metal atoms of identical electronegativity (such as two carbon atoms) will feature bonding that is totally covalent; metal atoms of identical electronegativity will feature totally metallic bonding; whereas two atoms of drastically different electronegativities will feature bonding that is totally ionic. However, for intermediate discrepancies in electronegativity, the bonding type will fall somewhere in between. This is quantified as the percentage of ionic character (%IC), a function of the two species' electronegativities.

Hydrogen bonding, as it is not relevant to this work, will also be described quite briefly. It is the term used to describe the interaction between two polar molecules: that is to say, two molecules where there is a very asymmetric dispersion of electronic charge. A classic example of this is water, chemically H_2O: while hydrogen and oxygen form a covalent bond, and might not naively be expected to form charges, the strongly electronegative oxygen atom will tend to pull the molecule's shared electrons towards itself. This results in a partial negative charge on the oxygen atom, and partial positive charges on the hydrogens. Thus, when two water molecules are adjacent to each other, the positive (hydrogen) ends of one molecule will be

attracted to the negative (oxygen) end of another. This intermolecular bonding is strong enough to cause noticeable macroscopic effects: for instance, water's boiling point is much higher than might be expected considering its very small molecular size, entirely due to these interactions.

van der Waals bonding is the weakest form of intermolecular interaction. It is used to describe the interactions that occur due to dipoles. Simply put, one may think about a dipole as a system where the electric charge is not totally homogeneous (the same everywhere), but is separated into regions of greater negative and positive charge. This may occur due to random fluctuations in the electronic cloud of an atom or molecule creating a temporary ("induced") dipole; when this happens in the presence of another chemical, the partial charge may either attract or repel electrons on its fellow, creating another induced dipole. These partial charges then attract each other electrostatically, resulting in a very weak bond. In other circumstances, due to the particular structure of a molecule, there may naturally be regions of partial positive or negative charge due to the differing electronegativities of component atoms. Such a molecule is said to be a permanent dipole. Permanent dipoles may interact with other molecules to create induced dipoles and then bond with them; alternately, they may also bond in the same way with other permanent dipoles. These are all described as van der Waals bonds; their relative strength varies, with bonds between two permanent dipoles being strongest and bonds between two induced dipoles being weakest.

2.5 Crystal Lattices

There are many types of crystal lattice, and it would not be a very good use of our time together to dwell on going through different varieties; we shall leave our discussions of specific lattices for the individual materials which are relevant throughout this thesis. However, I now offer this brief conceptual explanation to elucidate their importance in material science through a few well-known examples.

2.5.1 Explanation of Lattices

We know now how atoms may bind together to form small molecules, but how do they combine to form macroscopic structures - like, say, a chunk of quartz or a piece of glass? What do these materials look like on the atomic level? Is different composition all we must understand to understand different properties?

As it turns out, this is highly individually dependent upon the material in question, and it is not only a function of the component atoms. Actually, quartz shares its molecular composition with common glass: both types of material are composed of silica, SiO_2. However, what separates these two types of material is the way in which their composite atoms are arranged: that is, the geometrical shapes that are formed by those atoms. Quartz has a highly regular crystalline structure, with its atoms very neatly organized and arranged. Such a trait is in fact definitive of crystals in general. The high regularity of the atoms within contribute to common features of crystals in our day-to-day lives, such as the facets that we traditionally see in gemstones: when naturally occurring, these are in fact shear planes created by the regularity of the atomic structure, being the planes along which it is easiest to break the material. Thus, facets are not so much a construct of the jewelry industry as a fundamental consequence of the gemstones' innate order!

In comparison, glass is what is known as an "amorphous" solid. While it possesses the same atomic components as quartz, its atoms are not neatly arranged into a crystalline lattice but subject to a great deal of disorder. Glass is therefore considered a distinct "phase" of silica from quartz; it is created by highly heating and then rapidly cooling silica so that during the cooling, the component atoms do not have time to organize into a regular structure, but instead solidify into a disorganized construct.

2.5.2 Allotropes

We shall leave the amorphous solids for now, as, while quite interesting, they are not relevant to this dissertation. Let us briefly consider how two (or realistically, multiple)

distinct crystalline structures may exist for the same chemical species. A perfect example is that of graphite versus diamond. Both are different forms (known as allotropes) of pure carbon - but you probably wouldn't want to use a diamond pencil to take notes, or wear a graphite engagement ring. Graphite is a silvery-gray, whereas a relatively defect-free diamond is transparent. What creates the differences between these chemically-identical species? It all boils down to the different crystalline lattices the two possess. Graphite comes in sheets of carbon which are bonded covalently and hexagonally in two dimensions, with only weak van der Waals interactions in the third direction; diamond, however, has a three-dimensional covalently-bonded lattice, creating a strong stiff structure. We shall discuss in slightly more detail the reasons for this in Section 4.2.1, when we discuss graphene; however, what is relevant for now is to observe that different lattices may impart highly distinct mechanical and visual properties upon the same chemical species.

2.5.3 Crystal Orientation

All these properties are not completely homogeneous: some are in fact directional. It is trivial to note that for a given crystal structure (such as, for instance, the perovskite structure of $SrTiO_3$, depicted later in Figure 4.1; this is easiest to see with different atoms), if you start at a given atom and travel in several different directions, these directions are not the same: a particular atom may be encountered in one direction but not the other. You can helpfully think of taking different planar "slices" of the crystal structure. For the perovskite cube depicted in the figure referenced:

- a slice representing the left face of the cube will have four strontium atoms arranged in a square with an oxygen atom in the middle;
- a vertical slice halfway to the right (but parallel to the left face) will show a diamond of oxygen atoms surrounding a centered titanium atom;
- a diagonal slice from the lower-left edge to the upper-right edge will be rectangular,

with two strontiums at the top and bottom edges each, two oxygens halfway between on the long edge, and a titanium atom right in the middle;

- a slice from the far-top-left point to the near-bottom-left and far-bottom-right points will feature a triangle of strontium atoms, with oxygens at the midpoint between each strontium, and a titanium in the middle!

All these planar slices are completely distinct from each other. Accordingly, we consider them to belong to different "crystal planes", and the different organizations and compositions of these planes cause some physical properties along them to be different. These different planes are labeled systematically by what are called Miller indices; how to calculate these will not be described here, but guidelines may be found in Reference [2]. Suffice it to say that the first plane I described is the (100) plane, the second is the (200) plane, the third is the (011) plane, and the fourth is the (111) plane.

These Miller indices represent a host of atomically and structurally identical planes; planes with different Miller indices that are symmetrically equivalent are grouped into "families" (e.g. the (100), (010), and (001) planes - the faces of the cube - are all functionally identical, so they belong to the {100} family). Due to the different atomic arrangements, different planes in a crystal may be more easily cut along (these are the "shear planes" mentioned in Section 2.5.1): materials can also be harder along one plane than along another. Now, let's think about a rectangular slab of some material. What plane corresponds to the top surface? This entirely depends on how you cut it: it could be (100); it could be (111)! This top plane determines the overall crystal orientation of your material.

Now we have an idea of how the high regularity of a crystalline structure may contribute to the physical properties of a specimen, and that these properties may be directional; let us extend this revelation to understand that the electronic properties may also be affected by different lattices. One need look no further than graphite and diamond for an excellent example: both are just carbon, but graphite is a fairly good conductor of electricity, while pure diamond is quite insulating! Furthermore, in some materials, these electrical properties

are dependent on direction. Thus, it is not only relevant what elements go into a material in what proportions: the way in which those atoms are arranged in space also are critical to a substance's properties.

2.5.4 Defects

Up until this point, we have assumed that these crystal lattices are perfect: that they exactly resemble the predicted structure throughout. However, reality is never quite so perfect; thus, materials are generally found with a number of defects which change the lattice from the expected ideal. There are a number of defects of all dimensionalities (0D, 1D, 2D, and 3D) which are possible in material systems. However, this thesis is most interested in a few types of zero-dimensional, or "point" defects. I will therefore limit myself to discussing two common types of point defects which are of interest to this work.

The first such defect is known as the vacancy. A vacancy is essentially exactly what it sounds like: one of the atoms in the lattice is simply missing, leaving an empty space. These vacancies are able to move throughout a material by swapping spots with an adjacent atom: when the other atom moves into the place of the vacancy, it leaves behind an empty lattice space which is the new vacancy. A vacancy is generally specified in terms of the atom which is missing, such that a vacancy where an atom X is missing is usually notated as V_{X}.

Our second important defect type is substitutional. Substitutional defects are the replacement of one atom with an entirely different type of atom, which is not an element of the pure compound. Such atoms are termed impurities. These impurities may have the same electronic configuration as the atom which they are replacing in the lattice, or alternatively have a different number of valence electrons; in the latter case, sufficient numbers of these defects will have an impact on the electronic properties of the material.

Defects of different types may come together to form a defect complex. For instance, in some materials, two vacancies will occur adjacently to each other, known as a divacancy; one such defect complex is the divacancy in silicon carbide, where adjacent silicon and carbon

atoms are missing [3]. In other materials, substitutional atoms may occur adjacent to a vacancy, creating a complex: a famous example is the nitrogen vacancy center in diamond [4]. In this defect, one of the carbon atoms in the diamond lattice is replaced by a nitrogen atom: since nitrogen only has three binding electrons, it binds to three adjacent carbon atoms. The fourth adjacent carbon atom is then replaced by a vacancy, and the conjunction of these two forms a complex.

2.5.5 Diffusion

Diffusion refers to the way that atoms (or vacancies) travel throughout a material. This is generally thought of as "mass transport" at a macroscopic level, in comparison to "heat transport" (how heat moves into a material affecting its temperature) and "momentum transport" (which has to do with how momentum is transferred through, generally, a fluid). At any temperature, a material at the microscopic level is not entirely static: the different component atoms in the material may move, vacancies may swap lattice spots with adjacent atoms, and so forth.

Diffusion is a function of a species's concentration, in that atoms tend to move from areas of high concentration of their species to low concentration. One can think of putting a droplet of food coloring into a glass of water: the dye does not all stay clumped in the same place, but instead we can see the color moving outward as the food coloring diffuses into the water. Here, we can also visually see the concentration difference as how dilute the color is, with the center of the initial droplet slowly becoming more dilute in comparison, even as the rest of the water takes on color corresponding to the dye traveling in it. Diffusion is also fundamentally a function of temperature, in that the rate at which something diffuses in a material is determined by how the energy necessary for a substance to diffuse compares to the ambient heat energy (essentially, the temperature).

2.5.6 Annealing

There are many different ways to treat materials which can change their properties. One powerful such technique is annealing. In this process, the material is brought to a high temperature. Depending on what conditions are used in the annealing process, this can have different, permanent effects on the material even when it is brought back down to room temperature. Of course, a simple analogy is baking: when we bake cookies, we are subjecting the dough to permanent changes in character, which are retained even when they cool - baked cookies are qualitatively very different from raw dough, even when they are both at room temperature!

There are a few important parameters in the process of annealing. One is the temperature chosen at which to anneal. This of course has a significant impact on the final state of the material - one can imagine burning cookies to charcoal by baking them at too high of a temperature. When we heat a material, it may take on different properties relating to different "phases" that it may transition to at higher temperatures - for instance, some materials change to a different crystal structure when heated significantly.

Another important parameter is the cooling rate. This is a little harder to relate to our baking analogy, as usually we allow cookies to cool off to room temperature slowly by letting them sit. If we allow an annealed material that has entered a high-temperature phase to cool down slowly, there is still sufficient energy for some of these changes to be undone - the material may return to its initial phase. However, if we drop the temperature incredibly quickly (a process called "quenching"), there may not be enough time for this to take place, and thus the material may be frozen in its high-temperature phase. Quenching is an important part of tempering steel due to this freezing of properties; it is also, as we alluded to prior, the relevant factor causing glass to solidify amorphously instead of in a crystalline form.

One additional important parameter is the atmosphere in which the annealing is taking place. We can anneal materials under vacuum (an absence of gases); however, just as

frequently we may choose to do so under a particular atmosphere (with "partial pressures" of different reactive gases, as well as inert ones). Such a process may be relevant to defects within the material. For example, if a particular material has a large number of oxygen vacancies, these will be moving around a lot during annealing due to the heat dependence of diffusion. Annealing this material under an oxygen atmosphere, some oxygen atoms in the ambient gas may actually diffuse into the material, filling these vacancies. Conversely, annealing a material which contains oxygen atoms in a vacuum may result in oxygen atoms being pulled from the material to form oxygen gas, leaving oxygen vacancies.

Note generally that annealing, since it is the addition of heat to the material, will encourage diffusion of all sorts to take place throughout the material, since diffusion is a temperature-driven process.

2.6 Kinetic and Potential Energy

Often when we discuss energy in a psuedo-scientific context, we are fairly handwave-y about what it means. However, we may easily think about energy as falling into two primary types: kinetic and potential.

Potential energy is essentially "stored" energy; it characterizes a particular object or state in comparison to others. Generally, an object wishes to minimize its potential energy. This may seem slightly unclear, so I will give an example: imagine a ball sitting still at the top of a hill. If the ball were even lightly tapped such that it begins to move, it will immediately begin to roll down the hill. In this case, the height is directly related to the potential energy of the system: the ball wants to roll down to the lowest potential energy state. However, oftentimes there are energy barriers that prevent an object from achieving its minimal energy state, which require the input of additional energy to the system to surmount. To return to our analogy, imagine that there is a wall in front of our ball at the top of the hill. Even if the ball is tapped, it will not be able to roll down the hill because

there is a wall in front of it blocking it. However, if you add energy to the system by tossing the ball above the barrier, it will then be able to roll down the hill to the minimum energy state.

Kinetic energy is essentially the energy of motion. When the ball begins rolling down the hill, it is experiencing a decrease in potential energy; however, that energy is not lost, but has been converted into motion. Energy can be neither created nor destroyed; it merely changes form, a principle known as conservation of energy. Thus, a ball given a push along a flat surface will initially roll with a given kinetic energy; the reason it eventually slows down is that it is losing energy to the environment, in forms such as heat.

In the SI system of units, energy is frequently measured in Joules (J). However, an alternative unit of energy which is much smaller (and therefore more relevant to microscopic systems) and which will be utilized therefore in this work is the electron volt (eV).

2.7 Current, Voltage, and Resistance

In order to think about electronic systems, as we will later in this work, it is necessary to consider perhaps the three most widely-known quantities relating to electronics: current, resistance, and voltage.

A current is essentially a flow of charge. It is created by charge carriers (often we think of electrons, though as we will discuss later this is not always true) moving directionally from one point to another. In this work, current will be signified by I. In the SI system of units, current is measured in amperes (A).

Resistance describes a material's resistance to a current flowing through it. This is very much a material-dependent property, which is influenced by factors such as the crystalline structure, phase, and component atoms of the material. A material's resistance is also dependent on a number of external factors such as temperature, since these factors alter the material's microscopic properties. A material's resistance, where relevant, will be referred

to as R. In the SI system of units, resistance is measured in Ohms (Ω).

Voltage measures the difference in electrical potential energy between two points. This difference imparts a current between the two points, as the charge in the area will try to flow from a high to low energy state. Note that it is necessary to have two points to define a voltage: a voltage is a comparison, and cannot be thought of independently. Voltage is conventionally referred to as V, or sometimes ΔV to emphasize the differential nature of this quantity. In the SI system of units, voltage is measured in volts (V).

For a simple analogy, let us imagine a hill in an otherwise-flat field, with a waterfall flowing down from the top of the hill. The height of the hill relative to the ground represents the voltage of the system. The flow of water is analogous to the flow of current. Meanwhile, the terrain the water is traveling down characterizes the resistance: it could be extremely smooth (low resistance) or full of jagged rocks that create obstacles (high resistance).

The current, voltage, and resistance in a system are all related mathematically. The simplest model often used to relate these quantities is Ohm's law,

$$V = IR$$

Here, we can see that there is a linear relationship between the voltage and the current: when the current is plotted against the voltage, the slope of the line will be equal to the resistance (assumed in this case to be constant). Materials which obey this relationship, having such a linear relationship between current and resistance, are known as ohmic.

2.7.1 Superconductivity

One phenomenon which has fascinated a multitude of scientists is that of superconductivity. A superconducting material is one that has essentially zero resistance: that is, current is able to flow through the material totally unimpeded, without needing an applied voltage.

Superconductivity has never been observed at room-temperature; materials which su-

perconduct only do so at very low temperatures, such that materials which superconduct above 77 K (the boiling point of liquid nitrogen) are typically referred to as high-temperature superconductors (for comparison, room temperature is 300 K!). The critical temperature is the temperature at which a material experiences the onset of superconductivity; this is known as the material's T_c. Above this temperature, the material will possess a finite resistance.

Chapter 3

Semiconductor Physics

Now that we have a working understanding of the bare fundamentals, it is time to focus more specifically on the physics of semiconducting materials specifically. While still being primarily conceptual, this chapter will provide a more technical background for the work to be discussed in this dissertation. This chapter was composed with reference to Callister and Rethwisch's **Materials Science and Engineering: An Introduction** (10^{th} Edition) [2]; Streetman and Banerjee's **Solid State Electronic Devices** (7^{th} Edition) [5], and Kittel's **Introduction to Solid State Physics** (8^{th} Edition) [6]. Other references were also used for the topics of Dirac cones [7]; Fermi level, work function, electron affinity, and band bending [8]; and two-dimensional electron gas [9].

3.1 Band Structure

It may seem that once a bunch of different atoms are bonded together, via whichever mechanism, that that would be the end of the story: the material is no more than the sum of its parts. However, as is often the case with systems containing a large number of components, emergent properties that characterize the bulk system emerge. One of the most significant such properties is band structure. When a large number of atoms are all bound together to form a solid, the different energy levels available to each electron orbiting a given nucleus

may be thought of as being combined almost in the way a deck of cards is when it is being bridged and shuffled: many different electron states become available to all the electrons in the system. What may previously have been identical energy states on discrete atoms experience splitting when thus combined to form many states at many different energy levels. These may be very densely "packed" - that is, the difference in energy may be miniscule – and accordingly we may think of a region of very densely packed electronic states as forming a "band".

3.1.1 Valence and Conduction Bands

To begin with, let us imagine a single axis representing the energy of electron states. Traveling higher along this axis will take us to states with correspondingly higher energy, and vice versa. We may first think about the energy states of the valence electrons, which are tightly bound to their respective atoms: due to the stability of these configurations, they occupy a relatively low energy state. The dense band of electronic states representing these valence electrons is therefore called the valence band. Conversely, states corresponding to electrons which are free to roam about through the material's lattice are higher energy and make up what is referred to as the conduction band.

3.1.2 Band Gaps

In some cases – specifically and definitionally, metals – the valence band and conduction band are overlapping. Thus, valence electrons are free to transition between bands, and then travel through the material and conduct electrical charge, resulting in the typical high conductivity characterizing metals. However, such an intersection is often not the case: instead, there is often a gap in energy between the lowest point in the conduction band and the highest point in the valence band. This gap is often described as a "forbidden zone" because there are no energy states available for electrons to occupy. Thus, in order for an electron from the valence band to be "promoted" to the conduction band, an amount of

energy greater than or equal to the size of this gap must be conferred upon it – the addition of a smaller amount of energy will simply not be sufficient to promote it to a higher band.

There are many different ways of conferring the necessary energy for this promotion. For very small band gaps, the ambient thermal energy of the environment (calculated by multiplying the absolute temperature by the Boltzmann constant) may be sufficient to excite an electron. For larger band gaps, however, a means of transferring more energy is required. One of the most well-known methods, and the one on which we will focus throughout this work, is via photon: a photon may, upon "impact" with an electron, transfer its energy to the electron, allowing it to be excited to the conduction band.

Critically, this travel between bands does not go only one way: an electron may also lose energy and drop in energy from the conduction band to the valence band, in which case it will emit a photon corresponding to this drop (in order to obey conservation of energy).

The size of this energy gap defines a materials' electronic properties: conductors have either no band gap or a very small one; insulators have extremely large band gaps; and semiconductors feature band gaps of an intermediate size.

3.1.3 Direct vs. Indirect Band Gaps

So far, we have considered the band system as essentially falling on a vertical line: we have assumed that the lowest point in the conduction band lies directly above the highest point on the valence band, and thus only a photon is necessary to traverse that gap. However, to get a more accurate idea of the physics that is often at play, we must consider another axis (conventionally horizontal, perpendicular to the energy): that of the electron momentum k.

As a result of introducing this additional axis, it becomes possible for a conduction band minimum to exist at a different value of k than a valence band maximum. In order to travel between these energy states, therefore, a photon with energy corresponding to the difference between the maximum of the valence band and the minimum of the conduction band is not enough, since photons can only transfer energy (traveling up and down along

the energy axis). To travel horizontally along the k-axis, it will therefore be necessary to gain or lose momentum. This is accomplished via phonons, the quanta of vibrational energy. In an analogous way to how photons transfer an amount of energy corresponding to their wavelength, phonons similarly transfer an amount of momentum corresponding to their own respective wavelengths. Thus, moving between these specific points requires either absorption or emission of both photons and phonons. This is termed an"indirect band gap", as opposed to the direct band gap which does not have a transition involving phonons.

3.1.4 Dirac Cones

One possible band structure, which differs from that of metals as well as conventional gapped materials, is important to note. In the so-called "Dirac cone" band structure, the conduction band minima are the same as the valence band maxima at certain points in the band structure. Thus, the band gap is closed only for very specific values of momentum k. When plotted, the bands looks almost like an hourglass at these meeting points, with both valence and conduction bands linearly tapering to the same point - therefore creating the appearance of a "cone". This band structure arises due to and enables rich and interesting physics; however, a rudimentary and simplified understanding is sufficient for our purposes.

3.2 Fermi Level/Chemical Potential

One important parameter is the Fermi level E_{F}, also referred to as the chemical potential μ (these terms will be used interchangeably in this text). This is a material-dependent parameter which denotes the highest energy state which would be occupied by an electron were the material at equilibrium at absolute zero temperature. Above zero temperature, where statistics determine what energy an electron actually has, the Fermi level is taken as the energy level which statistically would have a 50% chance of being occupied by an electron. This energy level acts as something of a point of symmetry for the electron energy

distribution, inasmuch as the probability that an electron is in the energy level E_F+X is the same as the probability that an electron is *not* in the energy level E_F-X. As a whole, this parameter may be construed to characterize the electronic energy of a system.

Notably, for semiconductors and insulators, this value generally lies within the band gap; accordingly, electrons are not actually occupying a state at this energy because this state does not exist. Thus, it acts more as a measure of how likely it is that a charge carrier (electrons and holes, as will be discussed later) will enter the band where it can conduct (for electrons, the conduction band). In semiconductors, the Fermi level is influenced by the presence of additional charge carriers, i.e. doping: when the number of carriers are equal, this energy will be halfway between the valence and conduction bands; the presence of additional electrons will result in it being raised, while fewer electrons will result in it being lowered. Applying an electric field via gating will also shift the Fermi level. Therefore, the Fermi level is not a constant but a parameter which may be controllably changed.

3.2.1 Work Function

A material's work function is a measure of the energy that is necessary to move an electron within the material at the material's Fermi level to the vacuum outside the surface. Thus, mathematically the work function is the difference between the vacuum energy and the Fermi level. The work function is a material-dependent property.

One often-referenced example where the work function is relevant is the famous photoelectric effect, a fundamentally quantum effect which violates the expectations of classical physics and which Einstein won the Nobel prize for explaining. In this effect, light shone upon a metal surface will dislodge an electron from the surface of the material into the vacuum; however, the maximum kinetic energy of this electron is not dependent on the intensity of the light as may classically be expected, but its wavelength (since that determines the energy of the photon whose impact liberates the electron). In this case, we find that the difference between the energy of the light ($\frac{hc}{\lambda}$) and the maximum kinetic energy of the lib-

erated electron (E_{k}) is in fact equal to the charge of the electron q times the work function ϕ:

$$q\phi = \frac{hc}{\lambda} - E_k$$

This makes some intuitive sense when we think of the work function as a sort of energy "toll booth" in front of the interface with the vacuum (i.e. the material's surface): when the photon strikes the electron and is absorbed as energy, some of the energy gained must be lost to pay the cost of breaking free from the material. Since energy is neither created nor destroyed, the rest becomes the electron's kinetic energy.

3.2.2 Electron Affinity

The electron affinity is similar to the work function; however, whereas the work function is the difference between the vacuum energy and the Fermi level, the electron affinity is the difference between the vacuum energy and the conduction band minimum. Thus, it represents the energy needed to move an electron at the bottom of a material's conduction band to the vacuum outside the surface. If the electron affinity is subtracted from the work function, the result is the energy difference between the Fermi level and the conduction band edge.

3.2.3 Band Bending

We have so far assumed that a semiconductor's band structure is totally identical throughout the material - that is, that the Fermi level maintains the same relative position between the conduction and valence bands everywhere in the material. This is not necessarily the case: the surface of a material, as an interface, is sensitive to what is nearby.

If two materials in electrical contact have different work functions, the material with the lower work function (i.e. the material which is more easily able to give up electrons)

will lose electrons to the material with the higher work function. This transfer of charge will correspondingly change the Fermi levels of both materials until they are the same. Simultaneously, it will induce an electric field.

As a result of this electric field, near the surface of the material, the bands in the material may "bend" upwards or downwards relative to their position in the bulk - resulting in the conduction band becoming farther from or closer to the Fermi level, respectively. This may be linked, correspondingly, to a depletion of or accumulation of electrons at the surface relative to the bulk of the material. This results in a range of surface effects, the details of which depend on what the materials' electrical properties are.

3.2.4 Two-Dimensional Electron Gas

One possible result of band bending near the surface of a material is the creation of a two-dimensional electron gas (2DEG). In such a situation, the bands are bent downwards near the surface of the material to such an extent that the conduction band actually crosses the Fermi level of the material (but only close to the surface); accordingly, there is an accumulation of free electrons which are confined to a thin region near the surface of the material but able to move about in the plane of that surface. Thus, they are considered to form a two-dimensional system.

3.3 Charge Carriers

3.3.1 Electrons and Holes

We have up until this point been assuming that the charge carriers under consideration are solely and definitionally electrons. However, it is important to ask how conduction *really* takes place – that is, how is charge carried through a material? Traditionally, we think of electrons moving in the conduction band to act as charge carriers. However, it is equally possible to consider the absence of an electron (a "hole") as its own charge carrier traveling

through the valence band.

This may seem a little strange at first, so let us consider it fully. Imagine that we have a situation where a substance's valence band is entirely full of electrons and its conduction band entirely empty. Instead of just viewing the conduction band as "empty", we could alternately imagine it to be full of the *absence* of electrons - holes. These holes, comprising the entirety of the conduction band, are not moving and thus not transferring charge. However, let us imagine that we use a photon to excite a single electron up into the conduction band. It is essentially taking the position of a hole in the conduction band, while simultaneously leaving a new hole in the valence band. Just as the electron in the conduction band is free to travel through the lattice, so the hole in the valence band may also travel - one primary difference being that it moves not through its own motion, but by electrons essentially swapping places with the hole. Think of it like this: when an electron fills the gap previously acting as a hole, it leaves behind a gap of its own, so holes will travel in the opposite direction of electrons. Just as the electron acts as a negatively charged particle, the hole acts as a positively charged particle. However, it is technically *not* a particle, simply a phenomenon that takes on particle-like characteristics, so it is often referred to instead as a quasiparticle.

3.3.2 Mobility and Carrier Concentration

Mobility quantifies the average speed at which charge carriers move in a material due to an applied electric field. This quantity is typically reported in units of $\frac{cm^2}{V \cdot s}$. Electrons and holes have separate mobilities in a material. Mobility is adversely affected by carrier scattering, which interrupts the charge transport; in the low temperature regime, this scattering is primarily caused by ionized impurities, whereas at high temperatures, thermal lattice vibrations are usually the main cause unless there is a significantly high concentration of impurities to scatter off of.

The amount of charge carriers present per unit volume of material is the carrier concentration. The amount of carriers of a given type is directly related to the Fermi energy's

relative proximity to the band in which the particular carrier conducts; thus, when the Fermi energy is closer to the valence band, there will be a higher concentration of holes, and when it is closer to the conduction band, there will be a higher concentration of electrons. When a material's Fermi level is in the center of the band gap, the hole concentration will be equal to the electron concentration, a value known as the intrinsic concentration; for any Fermi level, the product of the hole and electron concentrations will be equal to the square of the intrinsic concentration. The carrier concentration is generally given in units of cm^{-3} (for bulk materials) or units of cm^{-2} (for two-dimensional materials).

3.3.3 Defect States

All the cases we have previously discussed assume that the materials used are completely pure – that is, that the material is composed exactly of the chemical species expected, and that its band gap as reported in the literature describes exactly the amount of energy which must be imparted to excite an electron from valence to conduction band, or lost when the electron drops from the conduction to the valence band. This is, however, not necessarily the case: the addition of particular defects to a pure crystal may result in the creation of energy states within the forbidden band gap. Thus, an electron could be excited from the valence band to such an intermediate state by a lesser amount of energy, and then excited from that intermediate state to the conduction band by another lesser amount of energy – essentially breaking the band gap down into steps. With many defects, you can essentially consider the intermediate states to form a band of their own in the band gap region.

This phenomenon explains why diamond, despite having an extremely high band gap, is not always an insulator: the presence of significant numbers of defects enable its transformation into a semiconducting material. These defects are notable for altering the visual appearance of the diamond due to their absorbing light of the appropriate wavelengths to excite the defect states: for example, large numbers of nitrogen impurities result in a yellow appearance, since violet light is being absorbed.

3.3.4 *p*-, *i*-, and *n*-type materials

Semiconductor materials may be treated to have an excess of either carrier type beyond their normal concentration. Those treated to have excess electrons are termed n-type, whereas those treated to have excess holes are termed p-type. In an n-type material, electrons are the dominant charge carriers, as we conventionally expect; however, in a p-type material, holes are the dominant charge carriers. The majority charge carrier will be the one to carry current; thus, in a p-type material, current is created by the flow of holes, instead of the electrons we typically associate currents with.

To make a material p- or n-type, doping is typically used. Doping is the addition of impurity atoms with either fewer or more valence electrons than the atoms which they are substituting. Incorporating atoms with fewer valence electrons essentially results in the addition of holes, while atoms with more valence electrons logically add electrons. Since the addition of holes entails the removal of electrons, the former dopants are conventionally refered to as "acceptors", whereas the latter are known as "donors". The presence of large numbers of these types of defects result in an excess of whichever charge carrier is being provided by the dopants. Doping will furthermore result in a shift of the Fermi level. n-type doping increases the Fermi level, while p-type doping decreases the Fermi level.

In contrast to p- and n-type materials, we have intrinsic materials, often referred to as i-type. These are undoped materials which have the natural carrier concentration of the pure material. Due to the lack of doping, these are generally significantly less conductive. In i-type materials, the Fermi level lies exactly in between the conduction and valence bands.

3.3.5 *p*-*n* junctions

A p-n junction is created when a p-type region of material is placed in contact with an n-type region. Since the p-type region is rich in holes and relatively low in electrons, and opposite is true of the n-type region, diffusion of the majority carriers from each region into the other will take place. This diffusion forms a region at the interface (the "space-charge region")

where the separate currents of the two carrier types flowing in neutralize each other, leaving a region with low conductivity. However, each side of the region is oppositely charged due to this loss of carriers.

These oppositely-charged sides creates a built-in potential difference in the material across the space-charge region. This may be further manipulated by the application of an additional voltage, or bias. The directionality of this bias is important: forward bias results in the flow of current across the junction, whereas reverse bias prevents current from flowing until the break down of the junction. Such a junction may be used to create simple circuit devices such as diodes (alone) or more advanced ones such as transistors (using multiple junctions).

3.4 Field-Effect Transistors

When working with semiconductors, it is necessary to construct devices to control and manipulate currents for technological purposes. One of the most basic devices that may be created is a field-effect transistor. Such a device includes three terminals. The source and drain terminals are the points between which the current I_{DS} in the device flows; there is a voltage difference V_{DS} between the two.

The other terminal is known as the gate, lying between the source and drain. The gate is a source of an independent voltage V_G, which produces an electric field in the sample. It is thereby is able to change the resistance of the conduction channel between the source and drain - thus changing the relationship between I_{DS} and V_{DS}, as well as fundamentally altering the Fermi level in a given region. Increasing or decreasing the voltage of the gate can thus result in change of the current at a given V_{DS}. Gates may be constructed on top of ("top gates") or underneath ("back gates") a material being gated.

Chapter 4

Materials

This chapter serves to compile relevant information about the materials used throughout the work summarized in this dissertation for the convenience of the reader.

4.1 Strontium Titanate

4.1.1 Basics of STO

Strontium titanate is chemically known as $SrTiO_3$ and is referred to from hereon throughout this text as STO. It is a semiconductor possessing both direct and indirect band gaps of 3.75 and 3.25 eV respectively at 4 K (with only a slight decrease at room temperature) [10] [11], corresponding to wavelengths of approximately 330 and 381 nm. It has a complex index of refraction, with a real part in the visible spectrum varying between 2.20 to 2.66 depending on composition and strain [10]. Its dielectric constant is very high, with a value of around 370 at room temperature and increasing to nearly 2 x 10^4 at low temperatures [12] [13] [14]. STO can be controllably changed from an insulating state, via a semiconducting state to a metallic, and even superconducting, state, via the addition of dopants either during crystal growth or via annealing [15]. The conductance of STO can be controllably changed between non-metallic and metallic via the application of an electric field, a phenomenon known as

resistance switching [16]. Vacuum-reduced strontium titanate has also demonstrated to superconduct at low temperatures [17], with a T_c of order 100 mK [18] [19].

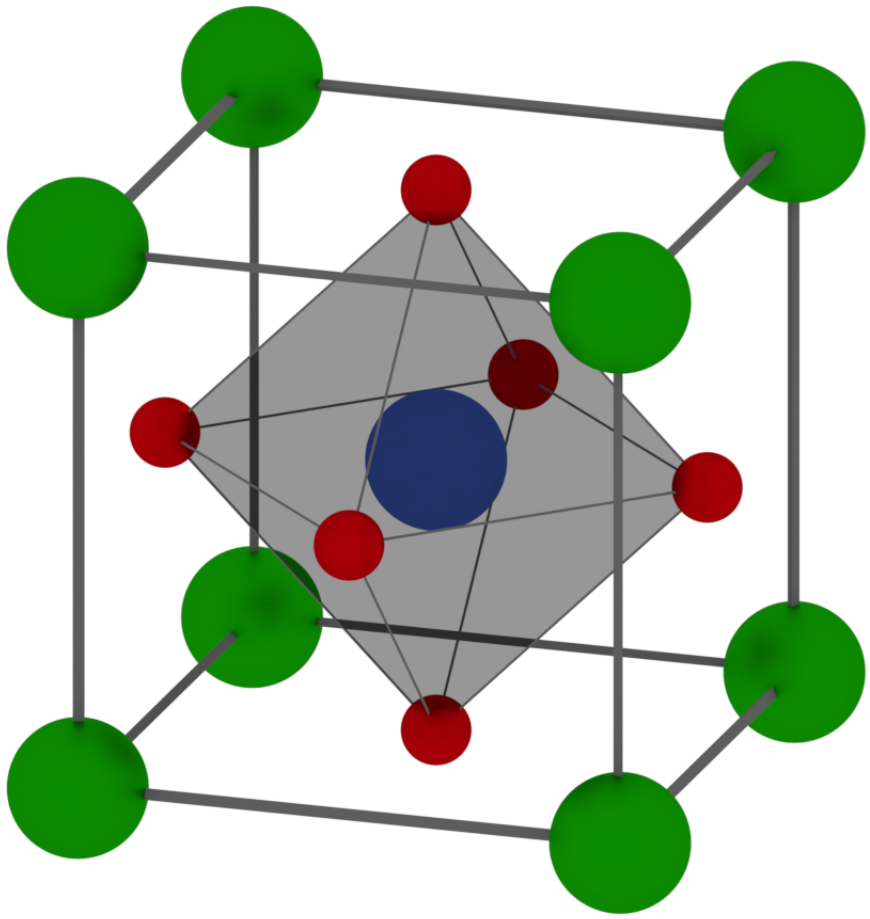

Figure 4.1: Depiction of the crystal structure of STO, showing its room temperature cubic perovskite phase. Here, we may see a titanium ion in the middle, surrounded by an octahedron of oxygens, while eight strontium atoms make up the corners of the cube. *Figure courtesy of Joost van Bree.*

The characteristic lattice structure of STO is perovskite. This structure may itself take on different phases: cubic (down to a second order transition temperature of roughly 105-110 K) and tetragonal (below this transition) [20] [21]. This transition involves a rotation of the TiO_6 octahedra which results in a reduction of overall symmetry of the system, as well as a change in the crystal's lattice parameters [21]. Other structural transitions possibly occur at lower temperatures [15]. An image depicting the cubic structure may be found in Figure

4.1. In the unit cell, which may be considered as ionic [15], a titanium ion (with a charge of 4+) is surrounded by six oxygen ions (with a 2- charge); furthermore, four strontium ions (with a 2+ charge) sit at each corner of the cubic lattice, themselves each surrounded by twelve of the oxygen atoms [15] [22].

Another phase transition, from a classical to a quantum paraelectric state, is known to take place at around 35-37 K and is attributed to quantum tunneling [15] [23] [24]. In this regime, the dielectric constant becomes independent of temperature, and randomly-oriented dipoles exist in the material; the application of an electric field enables alignment of these dipoles [15].

STO has a mean work function of approximately 4.26 eV at room temperature, but has also been shown to have slightly different work functions correspondent to different crystal faces, with the (100), (110), and (111) faces corresponding to measured work functions of 4.13, 4.32, and 4.34 eV respectively [25]. Physisorption and surface oxidation have also been shown to change the work function [26]. It also possesses an electron affinity of approximately 4.1 eV [27] [28].

STO as a material is a platform which displays a vast number of interesting material properties. Due to the desire to constrain this thesis to topics relevant to the work to be presented later, there is unfortunately not space to discuss all the fascinating physics which has arisen in the study of this material. For now, we will focus most strongly on topics related to this thesis.

4.1.2 Defects in STO

STO is host to a vast array of different types of defects. One of the most common defects is the oxygen vacancy [15], wherein one of the oxygen atoms in the lattice is absent. These have been seen in STO to form clustered complexes, such as divacancies, often around dislocation defects in the bulk material [29]. Such vacancies may be easily formed using vacuum annealing [29]: under a low partial pressure of oxygen, oxygen from the lattice is

bonded to form free O_2, leaving a vacancy and two electrons per oxygen [13]. Acting as double donors, oxygen vacancies include one electron which has a very small binding energy and is therefore almost always ionized, as well as a second electron which is more tightly bound and results in the production of blue luminescence [30].

Although low-temperature reduction can result in inhomogeneous distribution of these vacancies, particularly around dislocation defects, higher temperatures of reduction have been argued to make the distribution of defects more homogeneous, as well as increasing the carrier concentration [13]. Oxygen vacancies provide high-mobility free electrons, and increasing oxygen vacancies (only up to 0.03%!) can cause the material to transform from a dielectric insulator all the way into a superconductor [31], with a T_c of approximately 0.3 K [17].

Spatially-localized niobium doping can also create a two-dimensional superconducting state [32]. Increasing niobium doping is associated with a decrease in the resistivity of STO at or below room temperature [13].

Substitutional Ti defects are common in STO, with replacements often being transition metals such as iron (3+ charge), manganese (2+ charge), and chromium (3+ charge) [22]. Iron doping has been observed to result in a brownish coloration to the sample [33]. This doping enables the reaching of the metal-insulator transition via electroreduction at 250°C, which also produces a distinctive electrocoloration effect, with darker color associated with higher oxidation states and a more yellow hue to more reduced states of iron [33]. These experiments on electrocoloration relied on heating the sample to 250°C at low pressure to induce the movement of oxygen vacancies throughout the crystal [33].

In general, these transition metal substitutional defects may be compounded by the absence of an adjacent oxygen, forming a substitutional-vacancy complex [22]. Such complexes are generally referred to in the format e.g. Fe^{3+}-V_O. These Fe^{3+}-V_O defects are affected by different types of annealing: Zvanut *et al.* found that the concentration of Fe^{3+}-V_O complexes decreases significantly during annealing under oxygen-rich atmosphere at temper-

atures above 500°C, whereas subsequent vacuum anneals at temperatures between 300°C and 400°C were sufficient to increase the concentration again; vacuum annealing above 500°C, however, also decreased the concentration of this complex [22]. The energy needed to excite an electron to the $Fe^{3+/4+}$-V_O defect level - where an electron is liberated from Fe^{3+}-V_O leaving a more oxidized iron - has been found to be around 1.2 eV above the valence band edge [34].

Titanium vacancies may also be induced in STO via vacuum annealing at 1200°C with SrO powder [35]. These vacancies may form V_{Ti}-V_O complexes with oxygen vacancies which have been linked to persistent photoconductivity [35] [36].

Hydrogen defects may also be present in STO. Hydrogens bound to strontium vacancies (V_{Sr}-H) and hydrogen substitutionally replacing oxygen are two defects which are alternatively hypothesized to be the cause of persistent photoconductivity [37].

4.1.3 Photo-Induced Effects in STO

When stimulated with above-band gap illumination, the dielectric constant of STO has been observed to significantly change [38]. Furthermore, a transient photocurrent due to such illumination was found to involve the transport of both electrons and holes, which reduces upon application of an electric field: the subsequent localization of charge during gating has been cited as a possible cause for the corresponding increase in dielectric constant [38]. It is believed that electron-hole pairs are created during this optical stimulation, but the conductivity is specifically associated with electron motion [39].

Strong photoconductivity in response to ultraviolet light has also specifically been observed. One experiment saw hugely-increased responsivity below the structural transition temperature of 105 K; a notable decrease in conductivity was seen at around 37 K in this experiment, presumably corresponding to the transition to the quantum paraelectric phase [40]. Another experiment used ultraviolet light to control the carrier density, with more two-dimensional transport seen at short wavelengths (310/330 nm), while longer wavelengths (370

nm) showed higher electron mobility despite reduced electron densities; they associatedly observed a wavelength-dependent magnetoresistance [39].

A more persistent photoconductivity was observed to take place in the bulk of strontium titanate (which had previously been vacuum annealed at a maximum temperature of 426 K to create vacancies) upon exposure to sub-band gap light (2.9 eV and above) [35] [36]. This photoconductivity featured an increase in free-electron concentration of greater than two orders of magnitude, existed at room temperature, and demonstrated a persistence of order days [35] [36]. At the time, the authors concluded based on positron lifetime in the material that this persistent effect was likely due to the dual vacancy $V_{Ti\text{-}O}$ [36]. However, this persistent photoconductivity was later linked to annealing under water vapor, with the mechanism now believed to be linked to substitutional hydrogen defects in the place of oxygen being photoexcited to bond with V_{Sr}-H complexes, producing an oxygen vacancy and freeing two electrons to produce the resultant conduction [37] [41].

Significantly, a two-dimensional electron gas (2DEG) has been observed to be created on the (001) surface of 0.1% La-doped STO with an electron density that is directly related to ultraviolet irradiation (though this radiation had extremely high energy) [42]. This is believed to be caused by donor defects in the STO, such as possibly oxygen vacancies, creating an accumulation of electrons at the surface due to the deep downward bending of the conduction bands [42].

Of interest to this work is the effect of light upon specific defects. Zvanut *et al.* found that there was a significant increase in EPR intensity related to the Fe^{3+}-V_O complex in post-oxygen annealed samples upon illumination with ultraviolet light; however, samples vacuum-annealed above 500°C showed no effect due to ultraviolet illumination, as Fe^{3+} and Cr^{3+} also did not in any cases [22]. Thus, it was concluded that the effect of oxygen annealing was to oxidize Fe^{3+}-V_o centers to the Fe^{4+} state, while ultraviolet light served to ionize them back to the 3+ charge state [22]. It is also worth noting that Cr^{3+} was observed to be sensitive to ambient light at visible wavelengths [22].

Rice *et al.* also observed a sub-band gap absorption band (centered at 430 nm) in reduced STO which was slightly correlated with oxygen vacancy concentration (but not totally, indicating the relevant defect might be a complex); when this band was present, a polarization-dependent zero-field magnetization could be optically induced by 400-500 nm light at temperatures below 18 K [43]. This phenomenon was found to be dependent on the polarization of light used, with opposite handedness of circular polarization corresponding to an inversion of the effect and linear polarization causing it to vanish; furthermore, the induced effect was persistent for several hours even after illumination was ceased [43].

4.1.4 Impacts of Annealing on STO

As mentioned in previous sections, and as might be reasonably expected, annealing can have a significant effect on the defect populations in STO. This makes annealing a powerful tool in manipulating many of the properties associated with STO.

Annealing temperature during a reduction (i.e. low oxygen) anneal was found to have a significant effect on the resistivity of STO, with resistivity between 5-300 K decreasing as a function of annealing temperature [13]. It has further been linked to an increase in carrier concentration, with a reduction temperature of 600^{o}C corresponding to a carrier density of order 10^{15} cm^{-3}, whereas a higher reduction temperature of 1100^{o}C corresponded to a carrier density of order 10^{18} cm^{-3} [13].

Furthermore, the persistent photoconductivity observed by Tarun *et al.* was noted to only occur in the aftermath of vacuum annealing, albeit only to the relatively low temperature of 426 K [36]. Such annealing was believed to be necessary to create the vacancy defects believed to be responsible for creating this effect [36]. Vacuum annealing was also necessary to create the optically-induced magnetization measured by Rice *et al.* [43]

Annealing has a significant impact on the formation of Fe-V_O complexes in iron-doped STO, which is visually distinguishable: anneals with higher oxygen pressure result in a brown color characteristic of substitutional Fe, whereas reducing the partial pressure of

oxygen during annealing causes a transition to a more transparent color characteristic of Fe-V_O defect complexes [44]. Although oxygen annealing can quench the EPR spectrum associated with the Fe^{3+}-V_O defect, ultraviolet illumination results in a partial recovery of signal, indicating ultraviolet-induced ionization of the defect to this state [34].

It is also relevant to note that the persistent photoconductivity tentatively associated with either $V_{Ti\text{-}O}$ or hydrogen defects was produced in samples which had also been subjected to annealing; in the latter case, annealing under water vapor was specifically used to induce photoconductivity [36] [37]. Thus, annealing may be a necessary creator of defects associated with persistent photoeffects.

4.2 Two-Dimensional Materials

Atomically-thin sheets of material, often known as "two-dimensional materials", have come under a significant amount of scrutiny in recent years for their many novel properties. These materials are covalently bonded together in-plane to form sheets one- to several-atoms thick, which interact with other sheets in the third dimension via the much-weaker van der Waals bonding; as a result, such materials are also sometimes known as van der Waals materials [45]. Exciting physics that has been observed in such materials include superconductivity [46], piezoelectricity and ferroelectricity [47], thickness-tunable band gaps [48], and directionally-anisotropic transport properties [49] [50] [51] [52].

What makes this class of materials even more exciting is the fact that, due to the inter-layer bonding of stacked sheets being van der Waals and not covalent, sheets with very different crystal structures may be stacked, in direct contrast to normal bulk materials where lattice matching is a much more serious concern [53] [45]. This has created a common analogy of Legos in referring to these materials due to their robustness in stacking, and opened the door to the creation of so-called van der Waals heterostructures composed of multiple layers of two-dimensional materials [53]. Furthermore, these differences in lattice are not only

non-problematic; they also open the door to exciting new physics based on relative angles of different layers, as epitomized by the discovery of unconventional superconductivity at particular "magic" twist angles of bilayer graphene [54].

In this work, we will specifically focus on two of these materials: graphene and molybdenum disulfide, a member of the material class known as transition metal dichalcogenides.

4.2.1 Graphene

Since a single layer was first exfoliated in 2004 [55], graphene has captivated many scientists, and opened the door to the study of two-dimensional materials. Graphene is the two-dimensional form of the carbon lattice, wherein each carbon atom is sp^2-bonded to three other carbons to form a hexagonal two-dimensional pattern. This sp^2 bonding is a result of the hybridization of the s and in-plane p_x and p_y electron orbitals [56], while the out-of-plane p_z orbitals contribute a free electron which enhances conductivity [57]. Such bonding differs from the three-dimensional sp^3 bonding in diamond, wherein each carbon atom is bonded to four nearest neighbors arranged in three-dimensional space with the symmetry of two interpenetrating face-centered cubic lattices (a system conventionally known due to this fact as a diamond lattice) [2]. Graphene, however, does not feature covalent bonds in the third dimension; instead, its sheets are stacked via van der Waals bonding into a bulk form familiar to us all as graphite [56].

Famously, graphene was initially mechanically exfoliated from bulk graphite using sticky tape [55], resulting in a technique colloquially referred to as the "scotch tape method". This method remains highly relevant as a means of providing high-quality graphene [56]. Other means of manufacturing graphene have been explored, such as the reduction of graphite oxide to graphene [58]; unzipping carbon nanotubes [59]; and both catalytic [60] [61] and catalyst-free [62] [63] [64] chemical vapor deposition growth on a variety of substrates, including $SrTiO_3$ [65].

The electronic properties that this unique material possesses have created much of the

exciting science surrounding it. There are a relatively small number of defects present in high-quality graphene, meaning that current may travel across the lattice with relatively little impediment [56]. Furthermore, due to graphene's structure, its charge carriers have a linear dispersion relation and act as relativistic massless particles traveling at the material's Fermi velocity, resulting in the observation of behavior approximating Klein quantum tunneling [66]. Accordingly, high-quality graphene has been found to have an incredibly high carrier mobility, with one experiment demonstrating a value in excess of 200,000 $cm^2/V{\cdot}s$ for a suspended single layer [67]. Additionally, its band structure at the Fermi level takes the form of a Dirac cone, leading it to be described as a "zero-gap semiconductor" due to the lack of band gap between the valence and conduction bands [66] [68]. Via gating, the dominant carriers in graphene can thus be switched between electrons and holes [55].

4.2.2 Transition Metal Dichalcogenides: MoS_2

MoS_2 is one example of a material class known as transition metal dichalcogenides (TMDs). TMDs constitute materials with the formula AB_2, where A is a transition metal and B is a chalcogen (that is, an element belonging to the column of the periodic table below oxygen) [50]. Members of this family have displayed a wide range of interesting properties, such as superconductivity (seen in $NbSe_2$ [46]) and band gaps that move from indirect in the bulk to direct in the monolayer [50].

One application to which TMDs are often linked is the novel field of valleytronics. Valleytronics rely on the valley degree of freedom which electrons possess within the band structure; due to the inversion asymmetry of their lattices, many TMDs possess two inequivalent valleys in their band structure which can be moved between [69]; this essentially acts as a binary for hypothetical information storage [70].

Additionally, due to the fact that TMDs have broken inversion symmetry, different polarizations (right- or left-circularly) will preferrentially populate one valley over another, creating a discrepancy in population between the two [69] [70]. This enables observation

of the valley Hall effect, where under circularly polarized light which results in the greater population of one valley, a directional current and a resulting net Hall voltage are produced [69]. Furthermore, due to the fact that TMDs have strong spin-orbit coupling, the electron spins also have opposite signs at these valleys, resulting in spin-valley coupling which can lead to improvement in both spin and valley lifetimes as well as other interesting applications [70].

Molybdenum disulfide is particularly well-known among the TMD class due to the fact that its components are relatively harmless and easy to acquire [71]. MoS_2 may be produced by a variety of means, including exfoliation as well as direct growth by a number of methods, such as chemical vapor deposition and atomic layer deposition [71].

Structurally, the molybdenum atom is "sandwiched" between two layers of sulfur atoms; each sulfur is bonded to two molybdenums, whereas each molybdenum is bonded to four sulfurs, producing a hexagonal type pattern [71] [72]. When stacked in layers, the separate layer sulfur atoms position themselves to form a "zig-zag" pattern [73]. The material is extraordinarily flexible, able to retain its properties to a radius of curvature of 0.75 mm, making it a popular potential candidate for flexible electronics [73] [74].

MoS_2 possesses a band gap which varies from indirect in the bulk to direct in the single layer, enabling the tuning of its electronic properties via control of the number of layers [50]. In the single layer, its band gap has a magnitude of 1.9 eV [72], while its bulk band gap is 1.2 eV [73]. MoS_2 has been used to create transistors with an ON/OFF ratio up to 10^8 at room temperature [63]. It can possess a carrier mobility of above 200 $cm^2/V{\cdot}s$ [71] [72] [73].

While in the bulk, MoS_2 does not display photoluminescence, it does in the monolayer (and to a lesser extent in a few layers) [75], with peaks reported at 1.9 eV as well as 2.05 eV (corresponding to 653 nm and 605 nm, respectively) [73]; this photoluminescence can be enhanced by gating, as well as being substrate-dependent [73]. Optically, MoS_2 monolayers display a high absorption coefficient between 400 and 500 nm, dropping off to become essentially transparent above 500 nm [71] [76].

4.2.3 Other Materials

$(Bi,Sb)_2Te_3$ is related to the class of materials known as binary sesquichalcogenides, which include such members as Bi_2Te_3 [77]. These materials are three-dimensional topological insulators; $(Bi_xSb_{1-x})Te_3$ represents the class of ternary sesquichalcogenides which may be created by modifying the ratio of antimony to bismuth in the material, which enables a tuning of the carrier density [77]. As one might expect, $(Bi,Sb)_2Te_3$ is a formulation where bismuth and selenide exist in equal concentrations. Being a topological insulator, this material possesses a Dirac cone band structure in its surface states, along with a bulk band gap [78]. Thin films of this material have been observed to display a directional photocurrent whose direction depends on in which direction the light is circularly polarized [78].

Two-dimensional black phosphorus (known as phosphorene in the single layer) is a two-dimensional form of phosphorus which possesses a "wrinkled" structure [79]. This material is a *p*-type semiconductor, with a very high hole mobility that can exceed 1000 $cm^2/V{\cdot}s$ (though it is theoretically predicted to be able to exceed 10,000 $cm^2/V{\cdot}s$) and a recorded ON/OFF ratio of up to 10^5 [79] [49]. This material possesses a thickness-dependent direct band gap of 0.3 eV in the bulk, increasing to above 1 eV in the monolayer [48]. Its optical properties, as well as the extent of its mobility, are directionally anisotropic [49] [51].

4.3 Heterostructures

We have now dedicated a section to STO and a section to two-dimensional materials; however, STO has been used as a substrate for two-dimensional materials in a variety of heterostructures across many published works. In this section we will briefly touch on a few of these materials. Note that the papers most closely related to the work of this dissertation will be reserved for the literature review in the following chapter, in Section 5.1.3.

One of the most famous STO-related heterostructures is $LaAlO_3$/STO, where the $LaAlO_3$ layer is measured in unit cells - ergo essentially a two-dimensional material [80] [81].

At the interface between the two materials, a two-dimensional electron gas is formed, which has been attributed alternatively to causes such as the so-called "polar catastrophe" - an intrinsic electric field resulting from the coupling of a polar to non-polar material; to the oxygen vacancies within the two layers; or to intermixing between the different cations at the interface layers [81]. This two-dimensional electron gas shows great persistent photoconductivity in response to ultraviolet illumination at ambient conditions, particularly when enhanced with palladium nanoparticles [82]. This interface may be changed between conducting and insulating via a gating-mediated change in electron tunneling regimes [80]. The relative conductivity of the interface has furthermore been shown to be responsive to light (above 520 nm), and protonation or deprotonation of the $LaAlO_3$ surface has been associated with a change in conductivity exceeding four orders of magnitude [83]. Strikingly, the interface of this heterostructure has been demonstrated to be magnetic (despite the component materials' lack of magnetism) [81]. This magnetism is dependent on carrier concentration, resulting in behavior similar to the Kondo effect, where the resistance decreases with temperature until reaching a minimum at some temperature whereupon it again increases: the temperature key to this effect has been observed to be directly related to carrier concentration, and the increase in resistance at lower temperatures may be stifled using light of wavelength as high as 650 nm [81]. Superconductivity dependent on gate voltage has also been seen in this system, albeit with a T_c of order 100 mK [84].

Another important heterostructure is FeSe/STO. Despite the fact that in the bulk, FeSe is a superconductor with a T_c of 9 K, a monolayer grown on STO can have a T_c as high as 109 K [85]. Although at present the mechanism behind this enhancement is not certain, it is believed to be due to the transfer of electrons from the substrate, particularly when the STO has been previously subjected to vacuum annealing (which may be expected to induce oxygen vacancies) [86]. The high T_c has made it an exciting new material for high-temperature superconductivity. Furthermore, as has been demonstrated in thin flakes of FeSe on SiO_2/Si, liquid gating has been capable of changing the onset T_c from 10 K to 48

K [87] - thus it may be expected that FeSe/STO should similarly display gating-dependent T_c.

Other recent work has further elaborated on how 2D material/STO heterostructures may react to optical stimulation. In their 2020 paper "Optically Controllable 2D Material/Complex Oxide Heterointerface" [88], Tao Liu *et al.* placed a bilayer of $MoTe_2$ on a 15 nm thin film of STO (itself on a Si/SiO_2 substrate) in order to fashion a functional photodetector. This photodetector was exposed to a variety of light wavelengths within the visual range (notably all above the STO band gap wavelength). An according photocurrent was produced which was notably higher than the corresponding photocurrent found for the bilayer $MoTe_2$ placed on SiO_2, and to exhibit a more significant hysteresis when the gate voltage was swept, indicative of interfacial states existing where TMD meets STO. Further experimentation indicated that this work was translatable to heterostructures encorporating fellow TMDs MoS_2, WS_2, WSe_2, and $MoSe_2$ [88]. The photocurrents observed for all these TMD devices were found to be negative, and to quickly regain their initial negligible value upon cessation of illumination [88].

Chapter 5

Techniques

This chapter contains a description of the techniques utilized in this work. The first section, describing "optical gating" as a whole, is of key importance to all work done, being that this dissertation is centered around investigating the mechanism behind this phenomenon. The second section presents Kelvin probe force microscopy, which will be utilized in the work featured in Chapter 7 to better investigate details of the optical gating mechanism.

5.1 Optical Gating

5.1.1 Introduction

Control over a material's electronic properties necessitates the control of carrier types and concentrations within the material, as we have previously discussed. These properties are directly dependent upon the material's chemical potential. When the chemical potential of a sample is accordingly harnessed, it may be referred to as "gating" the sample. Such gating, when applied in different regions of a material, enables the creation of different devices: a classic example is that of the p-n junction, which may be produced by oppositely gating two adjacent regions of materials. Such a junction is critical to electronic systems, as explained in Section 3.3.5.

Of course, such control over electronic properties is extremely desirable for two-dimensional systems, many of which are interesting for device design specifically because of unique properties which may be harnessed through controllable gating. Accordingly, many techniques exist to achieve this end for such materials, such as chemical doping (via such techniques as the incorporation of dopants during the material's growth, the controlled diffusion of dopants throughout the material, or ion implantation) [89], the physisorption of gases (including O_2, NO_2, and H_2O) to the surface of the material [89], isoelectronic doping (wherein the dopant is chosen specifically for the close resemblance of its electronic properties to the doped material) [90], and electrolytic gating (where an electrolytic fluid is employed) [90].

Unfortunately, one commonality for many forms of gating is the necessity to modify the sample itself in order to achieved the desired effect. This may be acceptable for robust and large-scale samples, but can pose a problem for very small and chemically delicate ones. Two-dimensional materials are an excellent example of this latter case. It is extremely difficult to selectively control the doping of two-dimensional materials [50]. The physical properties and structure of such thin materials can be undesirably altered by the addition of chemical dopants [89], or damaged by the fabrication of electronic devices upon them [50]. Chemical doping of two-dimensional materials has observed to produce results that are unstable in ambient air, along with creating additional possible scattering points that negatively impact mobility [91]. Methods such as physisorption, electrolytic gating, and isoelectronic doping create issues of resolution control, both of the extent of gating as well as the spatial precision possible. Ideally, a gating technique for such materials would be spatially localizable, reversible, and completely non-invasive.

In 2015 [1], a new method of gating was described in the literature which bypasses many of the typical problems associated with such techniques. When a two-dimensional material is placed on a substrate of STO, the chemical potential of the material may be controlled entirely optically, via the application of light either above ("ultraviolet") or below ("red") STO's indirect band gap of 3.25 eV [10], corresponding to 381 nm.

Since the only thing interacting with the material itself is light, this approach is incredibly non-invasive in comparison to other techniques. This effect has been shown to be bidirectional and therefore completely reversible [1] [92], with ultraviolet and red illumination serving to oppositely raise and lower the chemical potential of the exposed material, with a corresponding effect on the materials' conductive current/resistance (which wavelength corresponds with which behavior changes for different materials, presumably due to the different dominant charge carriers associated [92]). Additionally, it is incredibly persistent [1] [92] [93]: once the chemical potential has been raised or lowered to a particular level, in the absence of further illumination, it may be observed (by the lack of change in corresponding material current/resistance) to remain more or less the same until further illumination is provided; since relatively little change was found to occur over a period of 16 hours [1], the decay rate seems to be incredibly long. Altogether, due to the non-invasive, spatially-resolvable and persistent bidirectional control over the chemical potential which this method provides, optical gating offers an incredibly exciting method for harnessing the electronic properties of a vast array of two-dimensional materials.

5.1.2 Proposed Mechanism

The cause of this interesting effect is believed to be certain defect states existing within the STO lattice, with the proposed mechanism described as follows [1] [92]. These defects are presumably relatively shallow, as they are able to be excited by the relatively long-wavelength red light used in these experiments. Although some candidates, such as iron (due to its involvement with other photoeffects in STO), have been proposed, currently the identity of the defect state responsible is unknown; thus, we consider it in this discussion simply as a generic defect.

When light is shone onto this heterostructure of two-dimensional material and STO, some of the light may interact with the two-dimensional material, contributing to different photoeffects or interacting with defects in that material. However, due to the incredible

thinness of that material, the majority of the light will be able to pass through it, and interact with the STO below.

The critical thing to realize here is that STO's indirect band gap at 381 nm means that photons of that wavelength and lower will be absorbed by the substrate when it is shone onto the material. Accordingly, this high-energy light is able to excite many of the defect states near the surface of the STO, but not those deeper in the bulk. This illumination results in charge carriers being excited and moving around throughout the lattice. During a sustained exposure to ultraviolet light, as long as the charge carriers remain close to the surface, they are able to be continually re-excited and travel about; however, since there is not an exclusive direction of travel, some will eventually drift deep enough into the substrate that the light is absorbed before it can interact with them again. As a result, during the continual re-excitation, there will be a net drift of carriers away from the surface of the STO and into the bulk. This depletes the region near the surface, creating an inhomogeneous charge distribution which changes the surface properties of the material as it interacts with whatever two-dimensional material is laid on top (essentially, tuning the charge of an incipient "back gate"). The region which ultraviolet light penetrates into STO has been calculated to have a depth of 7.1 um for 370 nm excitation [39] [94].

Observation of the effect in several material systems [1] [92] indicates that the carriers which are primarily being diffused are electrons, leaving the surface of the STO comparatively positively charged by their depletion. This dearth of negative charges creates an electric field which electronically affects any material which is placed on the surface of the STO.

To reverse this effect, accordingly, light with wavelength longer than the band gap's (traditionally, red) is shone onto the heterostructure. This longer-wavelength light is able to penetrate the material entirely, exciting the defect states throughout. Accordingly, as the re-excited carriers move about the whole of the lattice, the initial charge distribution inhomogeneity is relaxed and eventually extinguished, essentially erasing the temporary "back gate".

It is worth noting that Yeats *et al.* [1] and Liu *et al.* [92] observed that light of intermediate energy between ultraviolet and red was not as potent as red light. It seems plausible that there are other defect states in STO with higher energies which are absorbing some of the incident light and preventing it from acting to maximum effect on the responsible defect states.

This effect has been observed to be strongest at low temperatures, but still present even at room temperature; one possible reason for this increase is the nature of STO's high dielectric constant [1], which becomes even more massive at low temperatures as discussed previously in Section 4.1.1.

While the specific defect responsible has not yet been identified, Fe^{3+}-V_O has been considered as a candidate, due in part to its notable response to ultraviolet illumination as discussed in Section 4.1.2.

5.1.3 Optical Gating: A Literature Review

Although the utilization of STO as a substrate for thin films is well-established, relatively few publications have observed the optical gating phenomenon. In this section, I will provide a literature review for previously-published applications of this particular technique.

The first publication directly relevant to the topic of optical gating was the 2015 work by Andrew Yeats *et al.*, "Persistent optical gating of a topological insulator" [1]. In this seminal work, the "stepping" of the material's resistance in response to repeated periods of illumination followed by darkness was demonstrated, showing the sequential raise the chemical potential across the Dirac point of the topological insulator $(Bi,Sb)_2Te_3$'s Dirac cone band structure via ultraviolet light exposure, and then to subsequently lower it via red light exposure. This effect was shown to be equivalent to electrostatic gating of the sample, and they noted that the two methods seemed to be additive.

Additionally, a *p*-*n* junction in the material was created entirely using optical stimulation. Scanning photocurrent microscopy was used to confirm the spatially-resolved pat-

terning of p- and n-type regions on the topological insulator, showing the effect to have a resolution below 20 um. The effect was shown to have a persistence of over 16 hours, followed by near-immediate termination by the application of red light. The temperature dependence of ultraviolet light's effect on the material's resistance was also observed, showing it to be strongest at low temperatures but still non-negligible at room temperature.

Finally, a similarly persistent and bidirectional effect was demonstrated on a thin film of ZnO on STO, proving that the effect was not unique to topological insulators and thus opening the doors to application of this effect to other materials. Since ZnO is n-type, ultraviolet light was observed to decrease, and red light increase, the measured resistance of the material (though during red illumination, the resistance greatly decreased, likely due to photoconductive effects).

In explaining the effect, Yeats *et al.* proposed the defect-moderated mechanism which has been described in the previous section. They observed that the ultraviolet light seemed to be leading to the eventual loss of electrons near the substrate surface, causing a net positive charge at the surface of the STO. This inhomogeneity induces an electric field which influences the two-dimensional material on top; this field is then relaxed by the free charge diffusion throughout the material induced by red light.

These authors further expanded on this work in a 2017 paper, "Local Optical Control of Ferromagnetism and Chemical Potential in a Topological Insulator" [95]. This work used Cr-$(Bi,Sb)_2Te_3$. Here, optical gating was used to create p-n junctions in the material and demonstrate local control of the Fermi level, as well as to tune the coercive field H_c of the sample equivalently to backgating. This technique was used in conjunction with magneto-optical recording to demonstrate persistent optical control of both magnetization and chemical potential.

In 2016, Fucai Liu *et al.* reported in their paper "2D Black Phosphorus/$SrTiO_3$-Based Programmable Photoconductive Switch" [92] the creation of a 2D black phosphorus/STO heterostructure which demonstrated the familiar optical gating response to ultraviolet and

red illuminations, with the upward "stepping" of current in response to red light, and its retention of the value after illumination is ended, presented alongside the quick quenching of the current via ultraviolet light, and the repeatability of this effect for alternating illuminations of the two wavelengths. Bidirectional tunability via ultraviolet light was not demonstrated, presumably due to a high power density of light used, as the ultraviolet exposure turned the current off within seconds. This heterostructure was found to have an ON/OFF ratio of over 10^5 at 50 K.

Liu *et al.* found time constants for the processes of rising current induced by the red light, and the decays in the aftermath of both illumination types. The rise in current was found to be inversely related to temperature by an exponential function, being that it is mainly determined by the excitation energy of the defect. The decay in the aftermath of red was related to $T^{3/2}$, reflective of the fact that scattering determines this effect. Finally, the decay after ultraviolet illumination was fitted with a combined exponential and power law in temperature, indicating that this decay arises due to scattering as well as the excitation of the defect.

Intriguingly, in this paper, the heterostructure's performance was also compared with very preliminary results on MoS_2: whereas in the former case, red light increased the current associated with illumination and ultraviolet light quenched it, in the latter case the response to the two wavelengths was reversed, a reversal which the paper ascribes to the p-type character of the black phosphorus in contrast to the n-type character of MoS_2. Liu *et al.* attribute the effect as a whole to the creation of electron-hole pairs near the surface by ultraviolet light. Since the ultraviolet light may only penetrate a short distance into the material, this results in a net drift of the generated electrons to deeper within the material where they are unable to be further excited. Such an effect induces an electric field across the material interface. This electric field causes electrons in the black phosphorus to accumulate, quenching the hole-driven conductivity of the material. Conversely, red light is able to liberate the electrons deeper in the STO to neutralize the hole accumulation near

the surface.

A 2019 paper published by Ming Yang *et al.*, titled "Light induced non-volatile switching of superconductivity in single layer FeSe on $SrTiO_3$ substrate" [93], presents an excellent example of one of the exciting ways in which optical gating may be harnessed, though it did not address one-half of the effect, presumably due to a lack of familiarity by the authors with the other works described above. In this work, the FeSe/STO heterostructure, well-known for possessing a high superconducting T_c whose value depends upon the gating of the thin film, is exposed to ultraviolet light. As one might anticipate, exposure to ultraviolet light raises the T_c of the sample from 24 K to 30 K. However, to undo the effect, red light is not employed; instead, the application of -100 V pulses via the back gate is utilized to swiftly reverse the effect (within 5 s).

Yang *et al.* explain their results by suggesting that electron-hole pairs are generated under ultraviolet light, and that the electrons remain at the surface of STO while the holes are transferred into the FeSe [93]. However, this seems unlikely given the results of Liu *et al.*, since a transfer of holes into an overlying black phosphorus layer, and the accumulation of negative charge at the surface of STO, would be expected to aid in its hole-based conductivity instead of quenching it. Yang *et al.* acknowledge that superconductivity in FeSe/STO has been associated with electron transfer from the substrate, rather than hole conductivity, indicating that electron transfer is more likely to result in enhancement of the superconductivity [86].

Additionally, Yang *et al.* employed thermal cycling of ultraviolet-primed samples in a superconducting state at 16 K to higher temperatures, with the dwell time at higher temperatures exhibiting no seeming impact upon the reversibility of the effect. The maximum temperature employed, however, had a significant effect on the resistance of the sample when it was subsequently cooled to 16 K and measured, increasing noticeably at around 40 K and around 150 K, which they attribute to structural phase transitions in STO. These phase transitions may be expected to have an impact on the degree of charge separation in the

substrate, likely explaining why the effect of the ultraviolet light is correspondingly and increasingly mitigated with higher achieved temperatures during the cycle [93]. Interestingly, they note that there is no effect from the exposure of lower-energy (below the STO band gap) light upon the onset T_c; however, this is likely due to the lack of prior illumination by ultraviolet light. One expects that had the ultraviolet-illuminated material been subsequently exposed to longer-wavelength light, the corresponding T_c would have decreased accordingly. A proposal for a more comprehensive employment of optical gating with the FeSe/STO heterostructure will be detailed in the chapter on future work (Section 9.1).

5.2 Kelvin Probe Force Microscopy

Kelvin probe force microscopy (KPFM) [96] [97], also known as Scanning Kelvin probe microscopy (SKPM), is a scanning probe microscopy technique for measuring the electrical potential of a sample's surface. While it uses a similar set-up to atomic force microscopy (AFM), conventional AFM techniques rely upon the probe's mechanical contact with the sample in order to generate a signal that conveys topography at a nanoscale resolution [98]. In contrast, in KPFM there is an electrostatic force between the probe and the sample as a result of a difference in their work functions [97] [99]. Thus, this technique allows a spatial and temporal mapping of the work function across the surface.

5.2.1 Mechanism

The operating mechanism involved is perhaps best explained in comparison to AFM [96] [98] [100]. In the latter, the probe takes the form of a flexible cantilever with an incredibly sharp tip (typically 10 nm in radius) that is lowered towards the surface of a sample. In response to the van der Waals and electrostatic forces between the tip and the surface of the sample, the cantilever deflects. Laser light is reflected off the back of the cantilever, allowing this deflection to be monitored with a position-sensitive detector. AFMs may be operated

in different modes: the tip can either be maintained in direct contact with the surface of the sample, or the cantilever can be externally oscillated at its mechanical resonance frequency so that the tip makes intermittent contact with the sample. This latter "tapping" mode is advantageous in that both tip and sample are less likely to be damaged during measurement, and also because the resulting oscillation deflection can be more sensitively detected using lock-in techniques. In both modes, the deflection is measured and then fed into a feedback system, enabling the deflection to be maintained at a preset level by moving the tip vertically with respect to the sample; this relative motion is monitored as the tip moves laterally in the x- and y- directions, creating a topographic image of the sample surface [101].

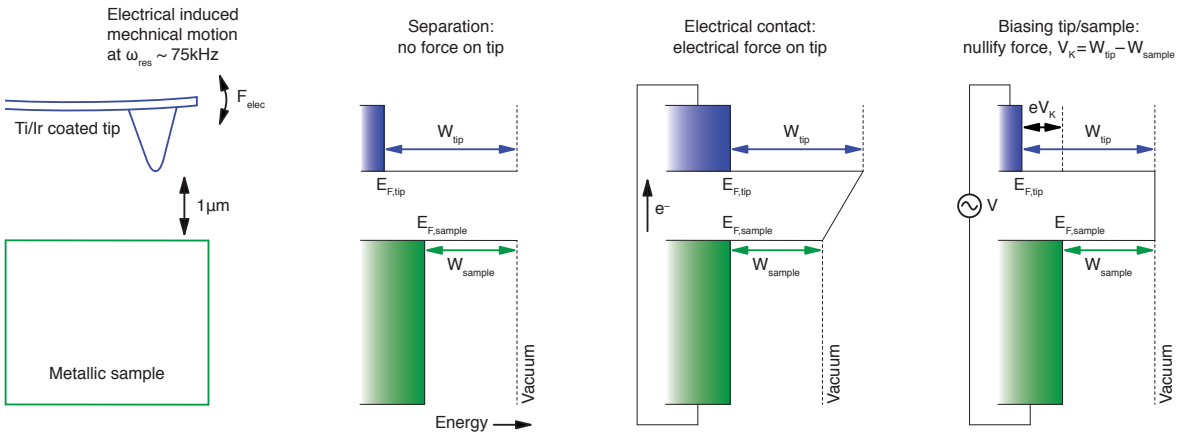

Figure 5.1: Figure depicting the mechanism of the KPFM technique. The leftmost image depicts a conductive AFM tip positioned above a sample, vibrating due to electrically-induced force at a resonant frequency ω_{res}. The center-left image depicts the work functions of the tip (W_{tip}) and the sample (W_{sample}) as well as their Fermi levels E_{F} when they are disconnected. In the center-right figure, the tip and sample have been electrically connected and an electrical force is being exerted. In the rightmost figure, a voltage is being used to nullify the electrical force and compensate for the difference in work function between sample and tip. *Figure courtesy of Joost van Bree.*

Figure 5.1 depicts the basic working mechanism of the KPFM technique [97]. KPFM utilizes similar probes to standard AFM, with the distinction that they are made of electrically conductive material (usually Si, coated with Ti/Ir). The tip is positioned above the sample (as in the leftmost image), which has a different work function (W_{tip}) and Fermi level ($E_{\text{F,tip}}$) from that of the sample (which has a work function W_{sample} and Fermi level $E_{\text{F,sample}}$). When the tip and sample are electrically connected (as in the center-right im-

age), the difference in chemical potential leads to electron transfer between tip and sample until their Fermi levels align ($E_{\mathrm{F,tip}}$=$E_{\mathrm{F,sample}}$). Any difference in work function between tip and sample will result in a potential difference - and therefore, an electric field - between the two. This field results creates an electrostatic force which deflects the cantilever.

The tip-sample system may be modeled as a plate capacitor with height-dependent capacitance $C(z)$ and potential difference $V = W_{sample}$ - W_{tip}, yielding an electrostatic force [102]

$$F_{el}(z) = \frac{C(z)^2 V^2}{2\epsilon_0}$$

where z is the distance between the tip and sample. The potential difference V may be canceled out by adding a DC bias to the tip equal to the difference in work functions between tip and sample ($V_{CPD} = W_{tip}$ - W_{sample}, as shown in the rightmost image in Figure 5.1). As a result, the force on the tip is nullified. Following this logic, the feedback system dynamically adjusts the DC bias to the tip to prevent deflection as the tip moves across the sample. This enables the spatial mapping of the difference in work functions based on the recorded bias at given locations.

It is possible to use lock-in techniques to get a more accurate measurement of the electrical force. This may be accomplished by modulating the force between tip and sample, and accordingly the deflection of the tip, similarly to the "tapping" mode used in regular AFM. Therefore, in addition to the DC bias, an AC bias (typically with an amplitude of about 1 V) is also applied to the tip. The mechanical resonance of the tip-cantilever system (typically 75 kHz) maximizes the sensitivity of this deflection. In the plate capacitor model, the electrostatic force now becomes [102]

$$\begin{aligned} F_{el}(z) \approx & \frac{C(z)^2}{2\epsilon_0}\{(V_{CPD} + W_{sample} - W_{tip})^2 + 2(V_{CPD} + W_{sample} - W_{tip})V_{AC}sin(\omega t) \\ & - \frac{(V_{AC})^2}{2}cos(2\omega t)\} \end{aligned}$$

A lock-in amplifier may then be used to detect the first harmonic of the force. This term will also be canceled out when the DC bias is equal to the difference in work function.

Although this model is simple, even when more complex interactions of the tip and cantilever are considered, these ultimately only serve to change the effective capacitance; thus, setting the DC bias equal to the difference in work functions will still eliminate the first harmonic term [103]. However, this model is based on a metallic sample; STO, being a semiconductor, will experience band bending. Nonetheless, calculations [102] and experiments [104] indicate that the DC bias still represents the difference in work functions (modified for band bending). However, according to the calculations, the force will have a different dependence on height compared to metallic samples; furthermore, nonlinearities in the dependence on both AC and DC voltages are expected [102]. Section 7.12.3 contains more detailed discussion of this factor in our measurements.

Chapter 6

Optical Gating Measurements

The measurements described in this section were performed by the author and Andrew L. Yeats, in the lab of David D. Awschalom, as featured in a manuscript currently being written. Peter J. Mintun helped with acquisition of the graphene sample and experimental design. Growth and preparation of the MoS_2 sample used in these experiments were performed by Kan-Heng Lee and Hui Gao, working in the lab of Jiwoong Park.

6.1 Introduction

In order to broaden the understanding of the optical gating effect's applicability, it is important to demonstrate how it affects a range of two-dimensional materials. To this end, we have performed measurements upon graphene and the transition metal dichalcogenide MoS_2 placed on STO. Basic characterization measurements on graphene were performed to demonstrate the effects optical gating would have on this famous material with a Dirac cone band structure, which was expected to behave similarly to the topological insulator $(Bi,Se)_2Te_3$ as measured by Yeats *et al.* [1] Additionally, a host of experiments were performed on MoS_2 to elucidate its performance as an n-type material beyond the initial measurement performed by Liu *et al.* [92] These measurements, beyond characterization, included an evaluation of ultraviolet power dependence upon transient and persistent measurements, a demonstration

of "stepping" the resultant current using ultraviolet and red illumination, and the effects of a temperature sweep upon a sample that was alternately previously primed with ultraviolet and red light.

6.2 Measurements

All measurements described in the following chapter were conducted in a Quantum Design Physical Property Measurement System (PPMS), which is capable of lowering the temperature of a sample to below 2 K at high vacuum. A customized cap for this PPMS containing red (650 nm) and ultraviolet (375 nm) LEDs enables light to be shone onto the sample, as controlled by two Yokogawa 7651s; in the absence of either LED being on, the sample chamber is completely dark. The samples' source-drain and gate voltages are applied by a Keithley 2600, which also measures the resulting current across the sample.

Samples were created using 5 x 5 x 0.5 mm^3 (111)-oriented STO obtained from MTI as a substrate. The two-dimensional materials differed in source and how they were placed on the sample and electrically connected. The graphene was commercially obtained from and transferred by Graphenea, with electrical connection provided in the form of indium dots adhered at the corners of the sheet. The MoS_2 was grown via metal organic chemical vapor deposition and vacuum transferred to the STO [105] [106]. Gold electrodes were created via electron-beam evaporation. Patterning of the MoS_2 was accomplished using fluorine ICP with SF_6/Ar. Final sample strips had the dimensions 10 μm x 30 μm. Samples were then adhered to a gold surface on PCB which was wired to serve as a back gate for the experiment, and wired to gold contacts which enabled connection to the Keithley 2600. Photographs of samples may be seen in Figure 6.1.

Measurements taken encompass plots of the drain-source current I_{DS} for given values of the drain-source voltage V_{DS} and the back-gate voltage V_G; in the case of graphene, the resistance was calculated (to enable better comparison to the literature). The system was

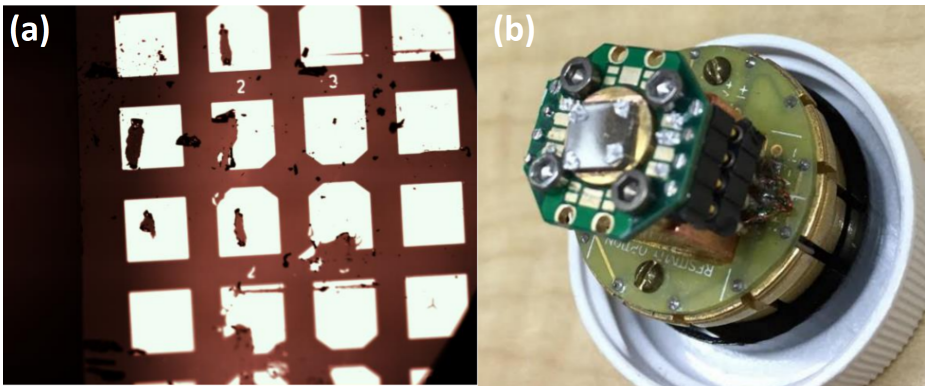

Figure 6.1: (a) Photograph of the MoS_2 sample; note that the gold contacts are visible and the strips of MoS_2 lie between them. (b) Photo of graphene sample as wired for the PPMS setup.

maintained at vacuum (approximately 10^{-6} Torr) for all measurements. All measurements, unless otherwise noted, were conducted at 10 K.

6.3 Graphene

6.3.1 Characterization

A measurement was carried out to observe the effect of continuous illumination upon the sample without utilization of a back gate. In this experiment, the sample was left in complete darkness for several hours before and as the measurement was initiated, to establish a baseline. Next, the sample was exposed to ultraviolet light at 0.64 mW/m^2, as the resistance increased and then decreased, until the resistance was observed to have a value roughly equivalent to that observed initially. After this exposure, illumination was halted, and the sample allowed to remain in darkness for approximately twenty minutes to observe its response. Next, red light illumination (15 W/m^2) was employed to return the current through the resistance peak and decrease to near its initial value. After this final illumination, all light was ceased and the sample was further observed in darkness for a final period of approximately fifteen minutes. In total, this experiment took roughly eighty minutes.

The data from this measurement may be found in Figure 6.2. There are several critical points which may be observed from this data, which is extremely comparable to the data

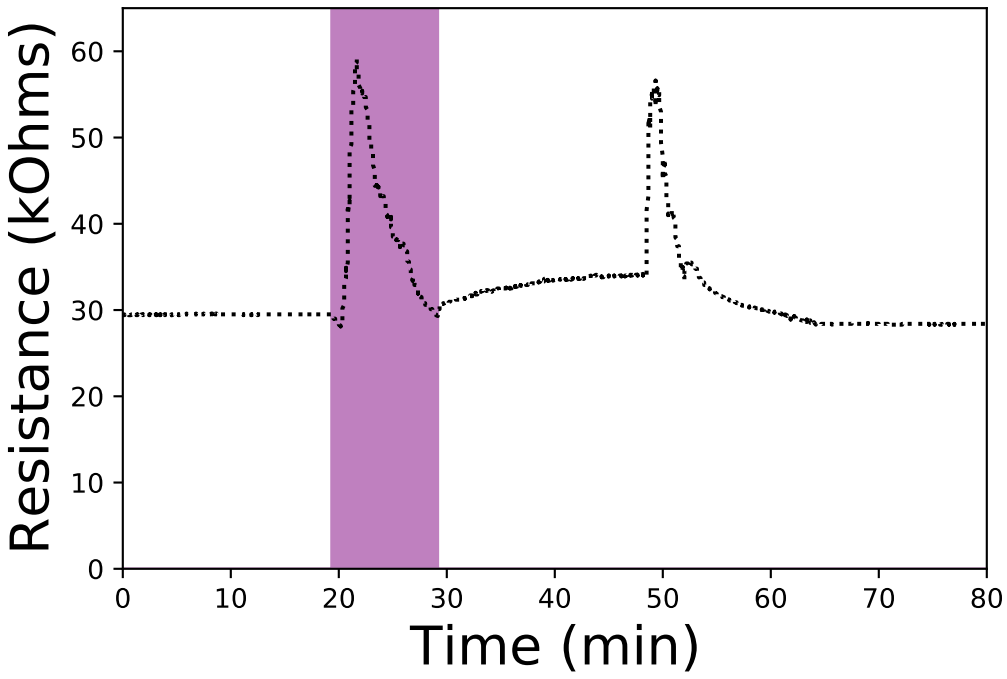

Figure 6.2: Graphene's response to optical gating, as measured via resistance. The highlighted portions of the graph correspond to periods of ultraviolet (purple) and red (red) illumination. This measurement was conducted at a temperature of 10 K.

presented by Yeats et al for the topological insulator $(Bi,Sb)_2Te_3$ [1], as might be expected for two species which both possess a Dirac cone band structure (*this comparison will more explicitly be discussed in Section 6.5*). First, during illumination with both colors of light, the current initially decreases from its previous value in darkness, then steadily increases again as long as illumination continues. This behavior is consistent with the chemical potential being swept through the Dirac point. However, the direction of this sweep depends entirely on the color of light used: in the case of ultraviolet illumination, the chemical potential begins initially below the Dirac point in the valence band (high current), up through the Dirac point (resulting in a maximal resistance), and then finally up into the conduction band (with the increase in available states corresponding to an decrease in measured resistance). Conversely, illumination with red light rapidly increases the current (quickly dropping back to the Dirac point), with the resistance slowly but steadily falling after this as the chemical

potential is lowered through the conduction band. The roughly triangular shape of both peaks is what would be expected for a Dirac cone band structure, confirming the presence and quality of the graphene.

Evidence that the directionality of this effect is as described – namely, that the chemical potential is indeed being increased by the ultraviolet light, and decreased by the red light – may be seen in the periods of darkness interspersing the illuminations. The initial and final dark measurements show almost no change in value across many minutes; however, the period of darkness after ultraviolet illumination shows a slow but quite perceptible relaxation. This relaxation would more logically be expected to correspond with a relaxation in chemical potential downwards towards a lower energy state, instead of a steady creep upwards to a higher energy state. Interestingly, the two peaks may be observed to have slightly different value at their maxima, with the ultraviolet illumination producing a higher peak (59.1 kΩ) than the red illumination (56.6 kΩ). This may be due to the different power densities used resulting in different effective "sweep rates".

Although the "stepping" of graphene utilizing subsequent pulses of red and ultraviolet light in the PPMS set-up at 10 K is not presented in this work, analogous data at room temperature was obtained utilizing a four-point probe station and may be seen in the following chapter, as shown in Figure 7.11.

6.3.2 Electrical Gating

Further support of this data corresponding to an increase and decrease in chemical potential is provided by a subsequent measurement. In this case, the chemical potential in darkness was altered directly via electrical gating by means of the sample's back gate, which was swept from a minimum of -15 V up through to a maximum of 50 V, and then back down again to -15 V. The data for this experiment may be found in Figure 6.3, which depicts both the increasing and decreasing voltage sweeps separately.

One fact which is immediately apparent is that the upwards and downwards sweeps do

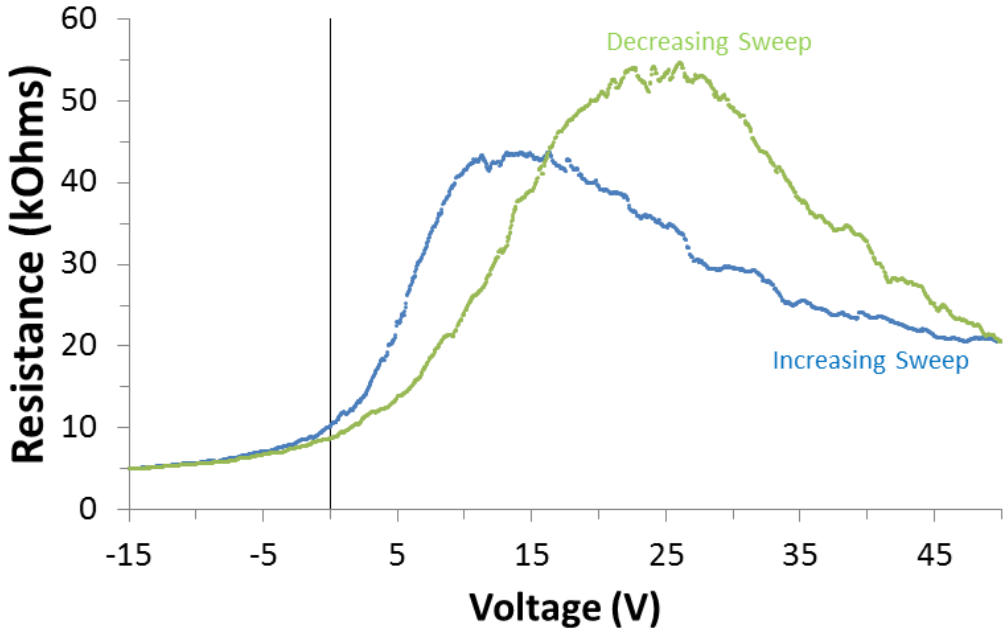

Figure 6.3: Graphene's response to electrical gating, as measured via resistance data for a sweep of V_g on graphene in darkness. Both the upsweep ("increasing") and downsweep ("decreasing") are depicted. There is a vertical line corresponding to a gate voltage of 0 V. This measurement was conducted at 10 K.

not neatly overlap, but display hysteresis, and possess two key differences: namely, while both sweeps demonstrate the roughly triangular shape that would be expected from the chemical potential traveling across the Dirac point, the location and amplitude of the minima are different. The upsweep reaches a maximum approximately 10 V lower than the downsweep does, and the resistance is slightly more than 10 kΩ lower for the upsweep. This is a much more significant discrepancy than was seen for the resistance maxima in the case of optical gating, which differed by only a couple of kilo-ohms. Hysteresis in graphene has been commonly observed, and is often linked to adsorbates [107]. Downsweeps have been observed to result in a relatively-higher V_G corresponding to conductance minimum (resistance maximum) in graphene versus upsweeping [107], as we observe here. The fact that this maximum occurs at above-zero V_G indicates p-typing of the material. This has multiple potential causes, one being doping of the sample via water adsorption, as was seen by Novoselov *et al.* in their seminal work on graphene [55].

It is also interesting to note that the peaks themselves also possess slightly different

values from those obtained via optical gating: the maximum resistance obtained is higher in the case of optical gating. Nonetheless, these values may be observed to be relatively close (59.1 kΩ versus 55 kΩ for the optical and electrical gating, respectively). The difference may be due to the sweep rate of the gating voltage.

6.4 MoS_2

6.4.1 Characterization

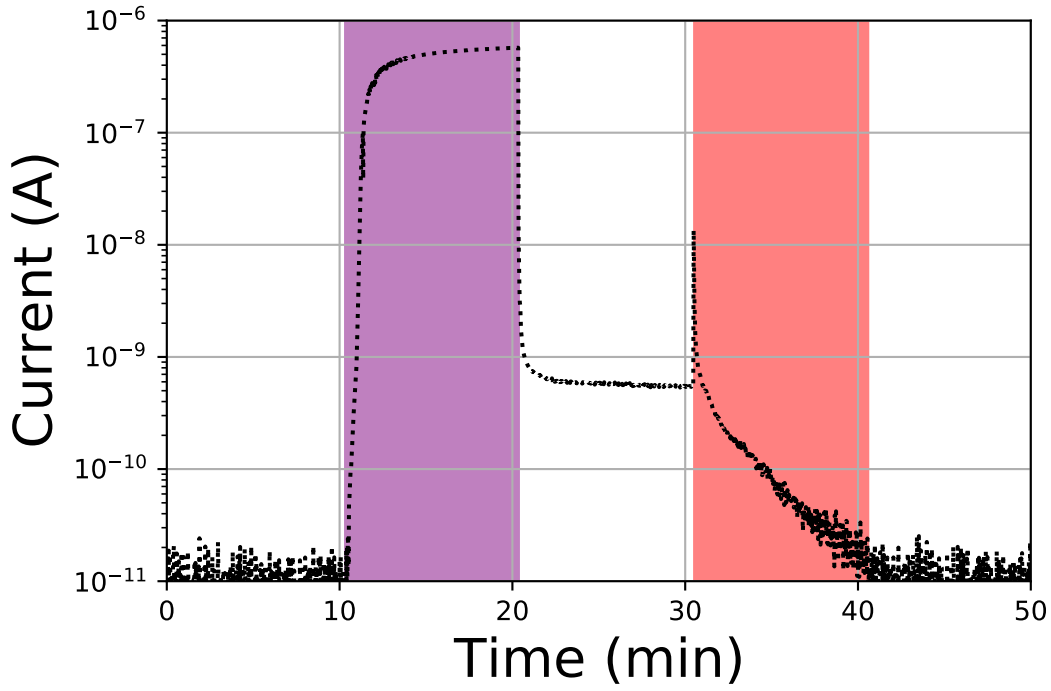

Figure 6.4: MoS_2's response to optical gating using 10-minute intervals of: darkness; illumination by ultraviolet light; darkness; illumination with red light; darkness. Highlighted regions show illumination with either ultraviolet (purple) or red (red) light. A power density of 0.002 W/m^2 was used for the ultraviolet illumination; a power density of 15 W/m^2 was used for the red illumination. Measurement was conducted at 10 K using a 0.5 V source-drain voltage. Note that the current is plotted on a logarithmic axis.

An initial experiment was carried out to observe the effect of both illumination sources upon the MoS_2 with V_{DS}=0.5 V and V_G=0 V. In this experiment, ten minute intervals were used: first a period of darkness, then ultraviolet illumination (at a power density of 2

mW/m^2), followed by another dark period, subsequent red illumination (at a power density of 15 W/m^2), and then a final period of darkness. This data may be seen in Figure 6.4. Note that the data here is presented on a logarithmic scale to allow for better comprehensibility.

What we may immediately observe from this data is that both initially and at the end of the experiment, the measured current I_{DS} is incredibly small – essentially zero (we will approximate it as 10 pA, treating this as the value of the "OFF" state). Since there is no conduction taking place, we may infer that we are beginning and ending our measurement in MoS_2's band gap. Turning on the ultraviolet illumination almost immediately raises us out of the band gap into the conduction band, as is apparent by the huge increase in current to approximately 570 nA. However, this immediate increase is not strictly exponential, as may be seen in Figure 6.5 (a): instead of appearing linear, there is an inflection point where there is a noticeable change in rate around 11 minutes. After this rapid increase, a new regime of extremely slow upwards drift is entered, as is visible in Figure 6.5 (b). Ultimately, this ON state gives us an ON-OFF ratio of approximately 5.7 x 10^4.

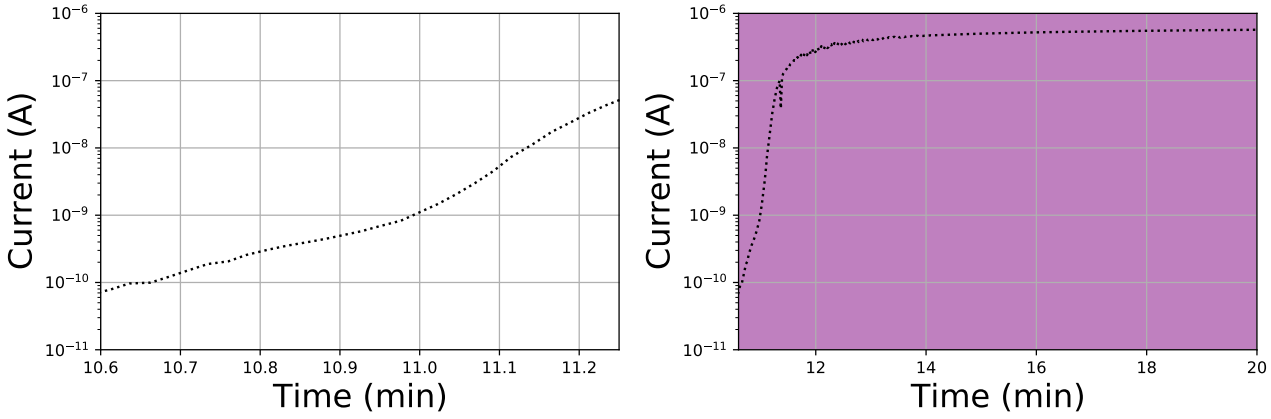

(a) (b)

Figure 6.5: Onset of the MoS_2 photocurrent during ultraviolet illumination. (a) shows part of the initial rapid ascent, while (b) depicts a longer period, also displaying the subsequent very slow increase. The current in both plots is depicted on a logarithmic axis.

It is very important to note that upon cessation of ultraviolet illumination, the current immediately drops back down again to an intermediate value of approximately 0.5 nA. This

indicates that in addition to the higher conduction afforded by the overall increased chemical potential, there is furthermore a photocurrent response in the MoS_2 itself which is not related to the persistent optical gating effect. This is clearly a significant effect, imparting a difference of nearly three orders of magnitude. Nonetheless, after this immediate decrease, the current maintains a roughly constant value, which we may treat as a secondary ON state that yields an ON-OFF ratio of 50.

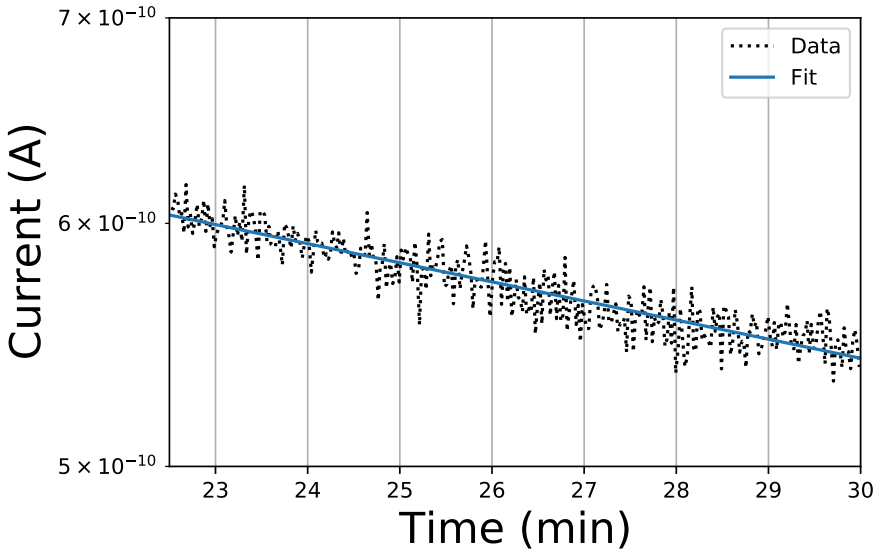

Figure 6.6: MoS_2's current decay after cessation of ultraviolet illumination. Plot displays data taken after the quenching associated with the ultraviolet light being turned off. The data is plotted with an exponential fitting functions of the form Ae^{Bt}, with parameters A=8.34 x 10^{-10} A and B=-0.0143 min^{-1}. The current is depicted on a logarithmic axis.

Taking a closer look at the data during this interim period, as plotted in Figure 6.6, reveal a plot that - on a logarithmic axis - is seemingly very nearly linear. However, if we look at the entire period of darkness (after the immediate drop in current due to the ultraviolet light being turned off), fitting an exponential function of the form Ae^{Bt} yields parameters of A=(8.34...$\pm$0.01) x 10^{-10} A and B=(-1.43...$\pm$0.04) x 10^{-2} min^{-1}. Inverting B gives us a decay time constant of approximately 70 minutes. This is seemingly a brief timescale for this effect, especially considering the extremely long persistence of the effect as seen in subsequent measurements.

This indicates that despite the seeming linearity of the data, a simple exponential fit

is probably not sufficient to capture the dynamics of this effect during this brief temporal regime. Likely, the complex transient decay from the ultraviolet-induced photocurrent's cessation is still playing a major role during this ten-minute period and obfuscating the more long-term effect, so this time constant may be expected to roughly characterize the after-effects of ultraviolet exposure. A more accurate time constant to describe the dynamics of the persistent regime will be determined based on the persistence measurements in Section 6.4.2.

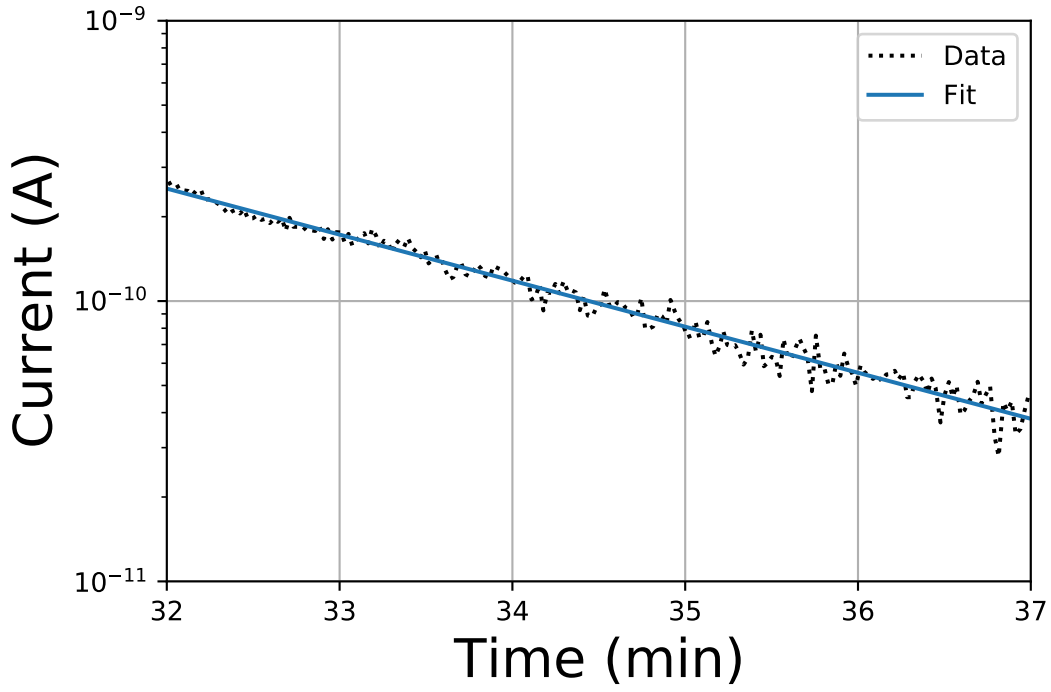

Figure 6.7: MoS_2 current decay during red illumination (after the initial spike at onset of red illumination). The decay in current between 32 and 37 minutes is plotted with an exponential fitting function of the form Ae^{Bt}, with parameters A=4.534 x 10^{-5} A and B=-0.378 min^{-1}. The current is depicted on a logarithmic axis.

Now applying a dose of red light, we see an immediate spike in current followed by a steady decrease which ultimately ends in the OFF state. This initial spike is possibly due to a photocurrent, but also possibly in part due to thermal effects – note that the power density of red light was significantly higher than that of the ultraviolet light (these values being chosen to impart the desired effects on similar time scales). Nonetheless, after this brief

spike, the decrease in current is steady, yielding a roughly linear slope on our logarithmic plot.

Since a linear slope on a logarithmic plot implies exponential decay, a subset of data during red illumination (after the initial spike but before the minimum value is close to being reached) was fitted to an exponential curve. This data is shown in Figure 6.7; aside from a few fluctuations in value, it may be seen to provide a fairly good fit, confirming that the red illumination process may be modeled with a simple exponential decay. For an exponential fitting function of the form Ae^{Bt}, the obtained parameters were A=(4.534±0.551) x 10^{-5} A and B=(-0.378±0.004) min^{-1}. Inverting B, we find that we have a decay time constant of approximately 2.6 minutes during the application of red light, characterizing the rapidity of the system's response to such illumination. Such a time constant may be expected to change as a function of the power density used.

6.4.2 Persistence

After this initial measurement, we then set about further characterizing the effects of optical gating on MoS_2. One of the most interesting characteristics of optical gating that had been observed in the literature is the long persistence of the effect; thus, to demonstrate that this persistence was also observable in MoS_2, we performed a several-hour experiment, also with V_{DS}=0.5 V. First, with the system set in the OFF state, we measured the ambient current for an hour. This was followed by illumination with ultraviolet light (0.6 mW/m^2) for an hour. After this, the system was allowed to sit for sixteen hours in darkness. Finally, the MoS_2 was again subjected to red illumination (15 W/m^2) for an hour, and finally measured again for an hour in total darkness.

The results obtained for this experiment may be seen in Figure 6.8. It is first relevant to observe that, despite the longer timescales utilized, the rough shape of the plot is much the same as the data obtained from the characterization experiment: after the initial negligible value, illumination with ultraviolet light causes a significant increase in the current; turning

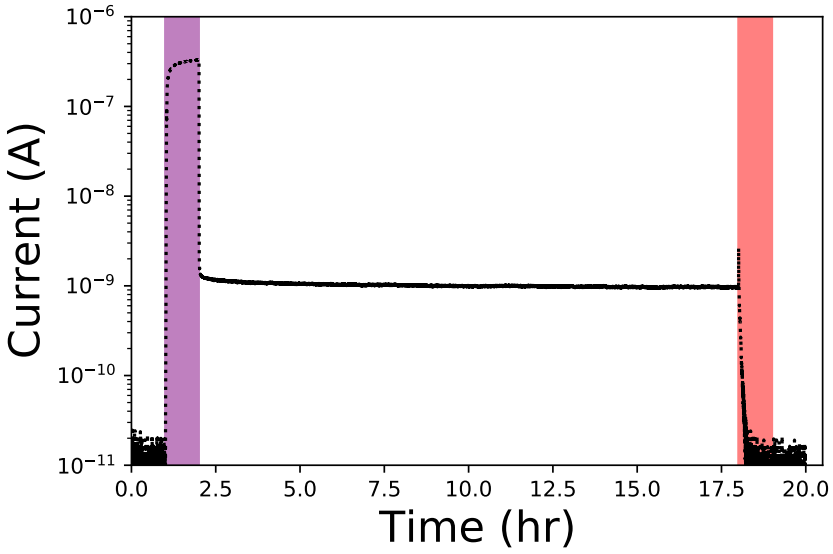

Figure 6.8: Plot demonstrating the persistence of MoS_2's heightened current following ultraviolet illumination over 16 hours. Current is shown as a function of time. Highlighted regions show an hour-long period of illumination with either ultraviolet (purple) or red (red) light. A power density of 6 x 10^{-4} W/m^2 was used for the ultraviolet illumination; a power density of 15 W/m^2 was used for the red illumination. Measurement was conducted at 10 K using a 0.5 V source-drain voltage. The current is depicted on a logarithmic axis.

this off leads to a drop in current to a relatively constant value, which is finally quenched back to the OFF state by the application of red light. While under ultraviolet illumination, the current is drastically increased as is typical for MoS_2, reaching a value of order 100 nA. Taking this as the "ON" state, and the initial current value, of order 10 pA, as the "OFF" state, yields an ON/OFF ratio of order 10^4.

In the intermediate period after the cessation of ultraviolet light, the current value substantially decreases from this initial "ON" state almost immediately. Treating the initial current value as the "OFF" state, and the persistent period, with a current of order 1 nanoAmp, as a different "ON" state, we see an ON/OFF ratio of 10^2 for the persistent dark current.

Since the intermediate period of darkness after ultraviolet light was significantly longer than that observed in the initial characterization measurement, it seems likely that this data will give a better value for the time constant associated with the decay, considering that any transient effects from the ultraviolet light's cessation should have ended. Accordingly, data

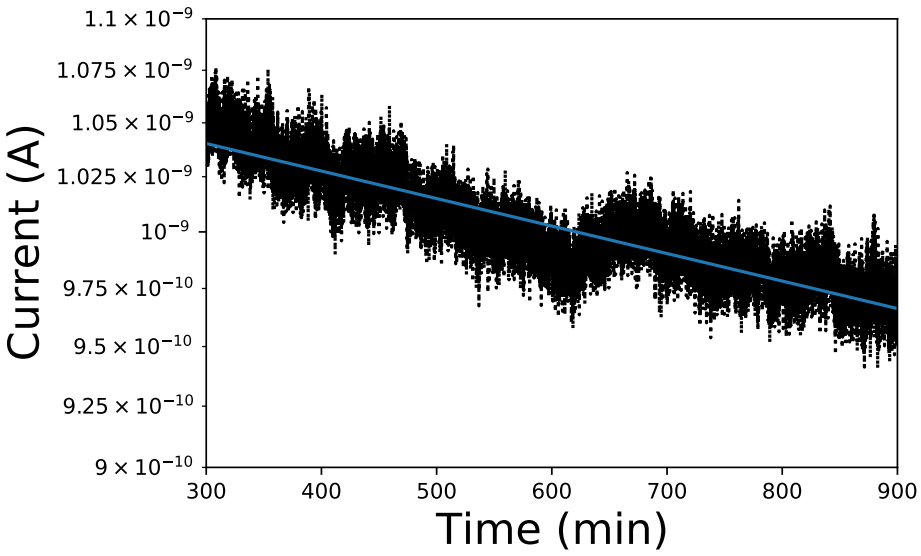

Figure 6.9: Exponential fit to MoS_2's persistent current decay. Plot displays a close-up of a subset of data taken in between illuminations (several hours after the quenching associated with the ultraviolet light being turned off). The decay in current between 5 and 15 hours is plotted with an exponential fitting function of the form Ae^{Bt}, with parameters A=1.08 x 10^{-9} A and B=-0.00738 hr^{-1}. The current is plotted on a logarithmic axis.

between 5 and 15 hours after onset of the experiment (i.e. starting three hours after the ultraviolet light was turned off, nearly three time-constants worth for the decay associated with cessation of ultraviolet light) was evaluated. This may be seen in Figure 6.9. Fitting an exponential function of the form Ae^{Bt} to the data results in parameters of A=(1.08...) x 10^{-9} A and B=(-7.38...±0.02) x 10^{-3} hr^{-1}. (*Note that the error in A was of order* 10^{-13}*, substantially smaller than the obtained value*). Inverting our value for B gives us a new time constant which is substantially larger than the one found in the characterization measurement: 136 hours, or more than 5.5 days. Such a lengthy time scale matches the long persistence of the effect as seen in this measurement.

6.4.3 Ultraviolet Power Dependence

Experiment were carried out to evaluate the effect of changing the power density of the applied ultraviolet light on both the "photocurrent" and "dark" ON states. For the former, the increase in photocurrent with power density for the first four minutes of illumination is

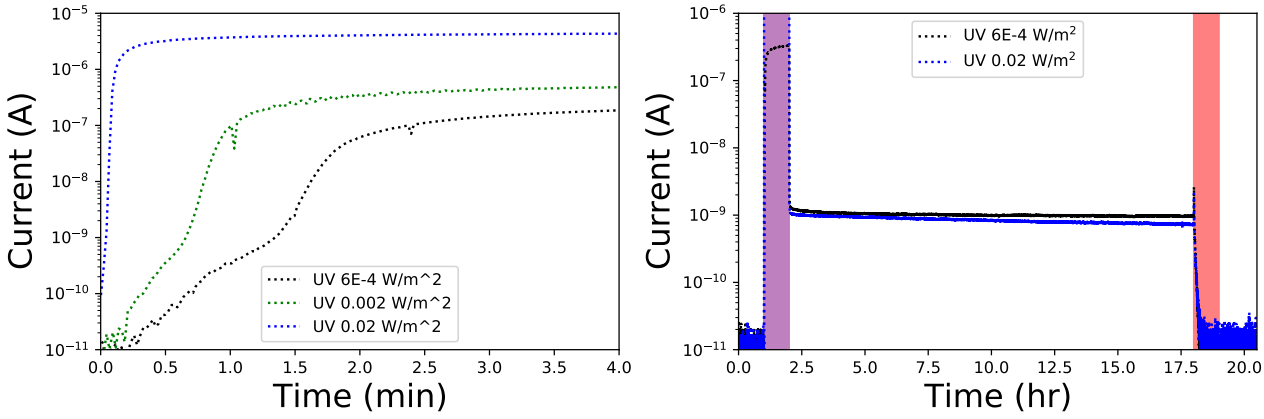

(a) Plot comparing the first four minutes of ultraviolet illumination at a variety of power densities.

(b) Plot demonstrating the persistence of heightened current following ultraviolet illumination at two different power densities over 16 hours, with current shown as a function of time. Highlighted regions show an hour-long period of illumination with either ultraviolet (purple) or red (red) light. A power density of 15 W/m^2 was used for the red illumination.

Figure 6.10: Ultraviolet power density dependence for MoS_2 current. Measurements were conducted at 10 K using a 0.5 V source drain voltage. Note that the current in both plots is given on a logarithmic axis.

depicted in Figure 6.10 (a). Taking the ratio of the photocurrents resulting from 0.02 W/m^2 and 0.002 W/m^2 evaluated after ten minutes' illumination gives a value of 8.08, close to the power density ratio of 10. Likewise, taking the ratio of the photocurrents after ten minutes of illumination for 0.002 W/m^2 and 6 x 10^{-4} W/m^2 gives a value of 2.18, fairly close to the power density ratio of 3.33. Thus, the photocurrent and power density within this regime tentatively seem to be directly related.

Since we speculated there might be some difference in decay rate based on power density of ultraviolet light used, we utilized the same sample bias (V_{DS}=0.5) and illumination pattern which was employed for the persistence measurement, comparing our initial data with data taken with a drastically increased ultraviolet power density (0.02 W/m^2). This comparative data is presented in Figure 6.10 (b).

It is immediately clear that the difference in ultraviolet power density has a significant effect on the photocurrent ON state after an hour: the greater power density has a far greater resulting current, achieving a value of 4.86 uA (approximately 5 x 10^5 times the approximated 10 pA OFF state). Thus, the photocurrent is clearly dependent on illumination power

density, as expected. At the same time, the rate of increase after the initial rapid increase period has ended is far slower, with the lower power density data showing a significantly greater rate of increase after the first few minutes of illumination. This may indicate that there is a saturated photocurrent obtainable for this MoS_2 system under illumination.

Interestingly, after the illumination is ceased, the current in both experiments dropped to the same rough value. This indicates that there is a maximum saturation value that can be attained for the persistent current regardless of the intensity of the photocurrent during illumination. However, the time constant of decay is actually faster for the higher power density, being reduced to 2 days. While this is still a multi-day persistence, this overall indicates that higher power densities may be undesirable for longer-term gating. The decay in response to red (with the same illumination power density used) is essentially the same between the two cases.

6.4.4 Ultraviolet and Red Stepping

Experiments were performed to determine the effects of multiple brief exposures to ultraviolet (and subsequently, red) illumination followed by darkness. The first experiment, whose data is depicted in Figure 6.11 (a), was carried out at V_{DS}=0.1 V. A power density of 6x10^{-4} W/m^2 was used for the ultraviolet illumination. A power density of 1.4 W/m^2 was used for the red, much less than in other experiments, to enable slow stepping of the current. Illuminations were not of a consistent duration or interval.

During each ultraviolet illumination, the current increases drastically before falling to a steady-state value once the illumination is ceased. The current during illumination increases with each successive pulse, following a basic shape similar to the current for uninterrupted ultraviolet illumination. A closeup of the current's behavior during the ultraviolet pulses may be seen in Figure 6.11 (b). Interestingly, after the fifth pulse of ultraviolet light, the current at steady state seems to saturate at the approximate value of 0.4 nA. This would seem to be the saturation value at V_{DS}=0.1 V, corresponding to the approximately 1 nA

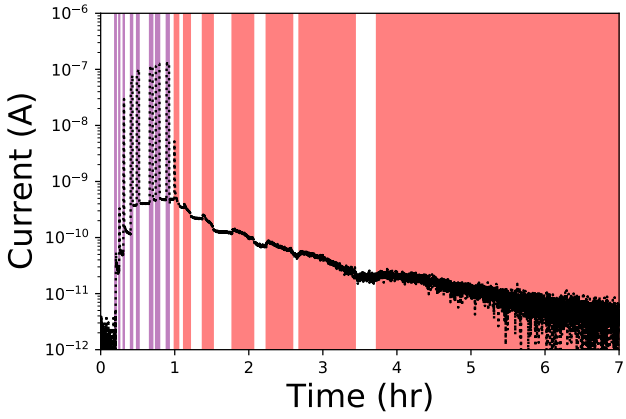

(a) V_{DS}=0.1 V; 6x10^{-4} W/m^2 ultraviolet power density; 1.4 W/m^2 red power density

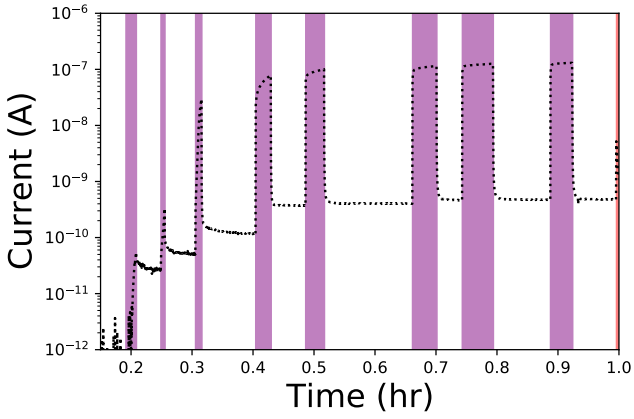

(b) A closeup on the ultraviolet pulse sequence of the previous plot.

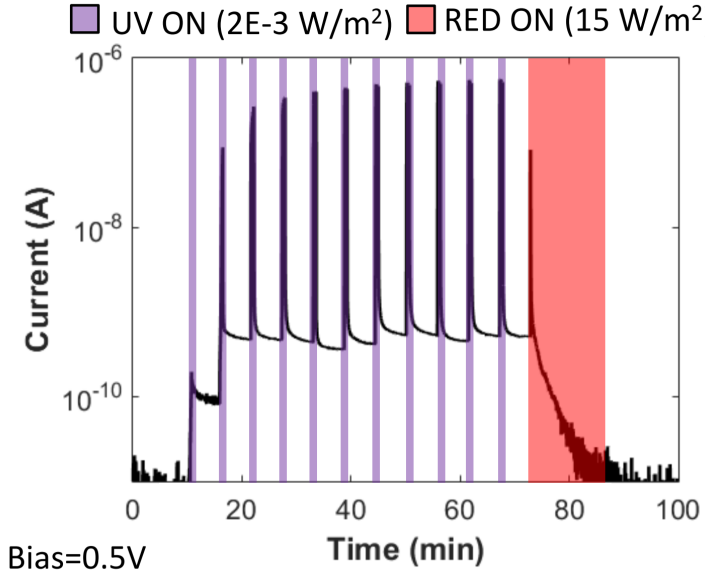

(c) V_{DS}=0.5 V; 0.02 W/m^2 ultraviolet power density; 15 W/m^2 red power density

Figure 6.11: MoS^2 current "stepping" behavior in response to repeated ultraviolet and red illumination pulses. Highlighted regions show illumination with either ultraviolet (purple) or red (red) light. Subfigure captions provide the details of the source-drain voltage and illumination power densities utilized. Measurements were conducted at 10 K. Note that the current is given on a logarithmic axis.

saturation for V_{DS}=0.5 V (as determined in the previous two sections).

While ultraviolet illumination has a rapid impact on the current, both during and after illumination, the effect of red illumination is more gradual. Instead of seeing a noticeable photocurrent peak for the duration of illumination, there is in some cases an initial small spike in value upon onset of the red, followed by a steady decline in value at a very shallow

slope. The relatively weak red power chosen enables a better view of the dynamics, showing that there is a gradual, nearly linear decay (on a logarithmic axis). Between red pulses, the current holds approximately constant in the dark for most intervals, with a slight decline visible following the red pulse ending just after the second hour of the experiment.

Using higher power densities of light (0.002 W/m^2 for ultraviolet, and 15 W/m^2 for red), and increasing the source-drain voltage to 0.5 V, yielded the data visible in Figure 6.11 (c). Here, only two pulses of ultraviolet light are necessary to attain the steady-state current value of 1 nA seen in the persistence measurements carried out at the same source-drain voltage. This supports the assertion that a higher power density enables a faster achievement of the persistent saturation current, and further indicates that the persistent saturation current is very quickly achievable with moderate power densities of light, allowing it to function as a switch.

However, while the switch may be "switched on" very rapidly, "switching off" is a much more drawn out process. Even at nearly 10^4 times the power density of the ultraviolet, the red light is still far less effective, taking more than ten minutes to reduce the current back to the initial "OFF" state. While greater power densities may be more effective, the possibility of heating effects eventually imposes a limitation on the viable rate at which the "OFF" state may be returned to.

It is also notable that although the rough value of the persistent current after ultraviolet illumination remains at the same order of magnitude, the actual value does not monotonically increase, but indeed decreases at certain points, while still maintaining the same rough value. The exact cause of this fluctuation is not known.

6.4.5 Electrical Gating

The effect of electrical gating via the back gate upon the sample was also ascertained to establish how it functioned compared to optical gating. For this experiment, the sample was first exposed to ultraviolet light to "prime" it. Then, the light was turned off, and the

measurement began by sweeping the back gate voltage down to -15 V. Subsequently, it was swept back up to 25 V, and then finally swept down to 0 V. The data for this experiment may be seen in Figure 6.12. Part (a) of the figure shows only the upsweep from -15 V to 25 V, whereas (b) shows the full data from the experiment. These measurements were conducted with a source-drain voltage of 0.5 V.

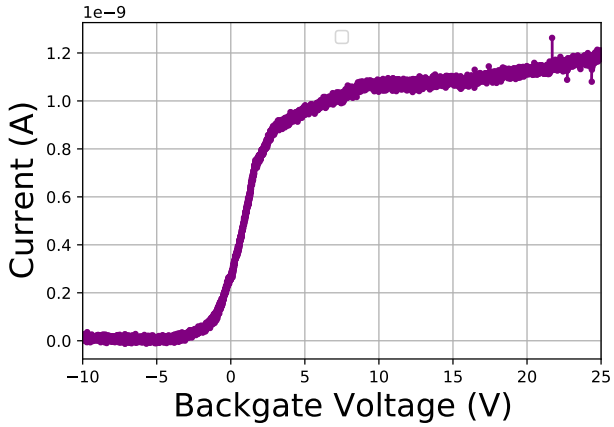

(a) Data depicting an back gate upsweep from -15 V to 25 V.

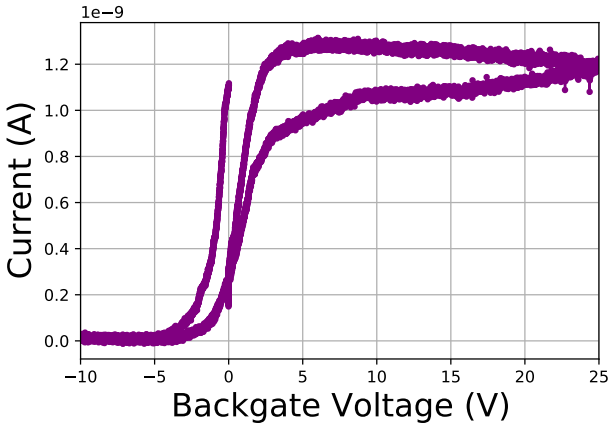

(b) Data showing the full sample history during the back gate sweep: starting at 0 V after having been primed with ultraviolet light, sweeping down to -15 V, then up to 25 V, and finally back to 0 V.

Figure 6.12: Plots depicting the response of MoS_2 to electrical gating via a backgate voltage sweep.

The data shown in (a) confirms the hypothesis that back gating functions similarly to the optical gating in terms of resultant current. Initially, the current is in the pico-Amp regime, being barely perceptible; however, increasing the back gate voltage results in a fairly rapid increase in current between approximately -2.5 V and 2.5 V. This increase then tapers off as the back gate voltage continues to increase towards a "steady-state" around 1.2 nA, similar to the saturation current of the optical gating for this V_{DS}. The high slope during the initial ascent in current is reminiscent of how quickly the saturation current was attained with ultraviolet pulses in Figure 6.11 (c); overall, as expected, the graph is very similar to the step-function graph a switch would have, with an onset voltage around -2.5 V.

The full data set also shows the impact of the ultraviolet priming. The current starts, at a back gate of 0 V, with a value of 1.1 nA due to the ultraviolet exposure. This decreases

during the down sweep, but the decrease is offset from the upsweep curve by over a volt. While this may seem like a small difference, considering the rapid change in current that occurs in this range, it is still significant for the sample.

When the minimum current is reached, this seems to quench the effect of the ultraviolet priming for the upsweep. While hysteresis is visible when the back gate has a positive voltage value, it ultimately returns on the final downsweep to approximately the same value at 0 V back gate that it had on the upsweep. This indicates that the effect of the ultraviolet light has indeed been erased.

6.4.6 Mobility and Carrier Concentration Calculations

We are able to estimate the mobility μ of the MoS_2 in the persistent ON state via the equation [108]

$$\mu = \frac{\delta I_{DS}}{\delta V_g} \frac{L}{W C_i V_{DS}}$$

where L is the channel length, W is the channel width, C_i is the capacitance of STO per unit area, and we may estimate $\frac{\delta I_{DS}}{\delta V_g}$ based on the slope of the electrical gating curve. The channel's length is 30 μm and width is 10 μm. The value of V_{DS} used is 0.5 V. A linear fit was used on the steepest descent of the first downsweep of the electrical gating measurement to estimate the derivative of the ultraviolet-primed state, and was found to have a slope of 1.27 x 10^{-9} A/V. We may use the relation

$$C_i = \frac{\epsilon_0 \epsilon_{STO}}{d}$$

where the thickness $d = 0.05$ cm, and the vacuum permittivity ϵ_0 is 8.85 x 10^{-14} F/cm. ϵ_{STO} is approximately 10^4 at 10 K. We may thereby calculate a value for μ of approximately 0.431 $cm^2/V{\cdot}s$. This number is rather low for MoS_2 at low temperatures, where values of order 100 $cm^2/V{\cdot}s$ have been reported on silicon substrate [109]. However, its order of

magnitude is comparable to some measurements of monolayer MoS_2 on Si/SiO_2 substrate taken at low temperature and low source-drain voltages, where the relatively insulating state was attributed to charges trapped at the device-substrate interface, and low carrier density [110]. Thus, we may expect that our sample falls into a similar regime to those results.

We are further able to calculate the electron carrier concentration n via the equation [111]

$$n = \frac{I_{DS}L}{qW\mu V_{DS}}$$

where q is the charge of the electron, being 1.602 x 10^{-19} C, and using the value of 1.1 nA for I_{DS}. Thus, we find a carrier concentration of 9.56 x 10^{10} cm^{-2}.

6.4.7 Temperature Sweep

The response of the current to a temperature sweep from 10 K up to 300 K and then back down was also measured at a sample bias of V_{DS}=0.5 V. Although the sweep was performed in darkness, the experiment was performed twice to compare the effects of initializing the sample with ultraviolet and red light. This data may be seen in Figure 6.13.

The most immediate takeaway from this figure is that clearly, the initialization state of the sample has a significant impact on how the induced current behaves as a function of temperature. In all cases (up until the downsweep reaches approximately 50 K), the case where ultraviolet priming had been applied produced a higher current. This difference is most immediately obvious at low temperatures at the beginning of the upsweep, where the current in the aftermath of ultraviolet light exceeds the red-primed case by two orders of magnitude. However, the difference is still perceptible at room temperature. While it is known that the optical gating effect may be induced at room temperature, this offers further confirmation that the effect, when initiated at low temperature, still persists through drastic increases in temperature.

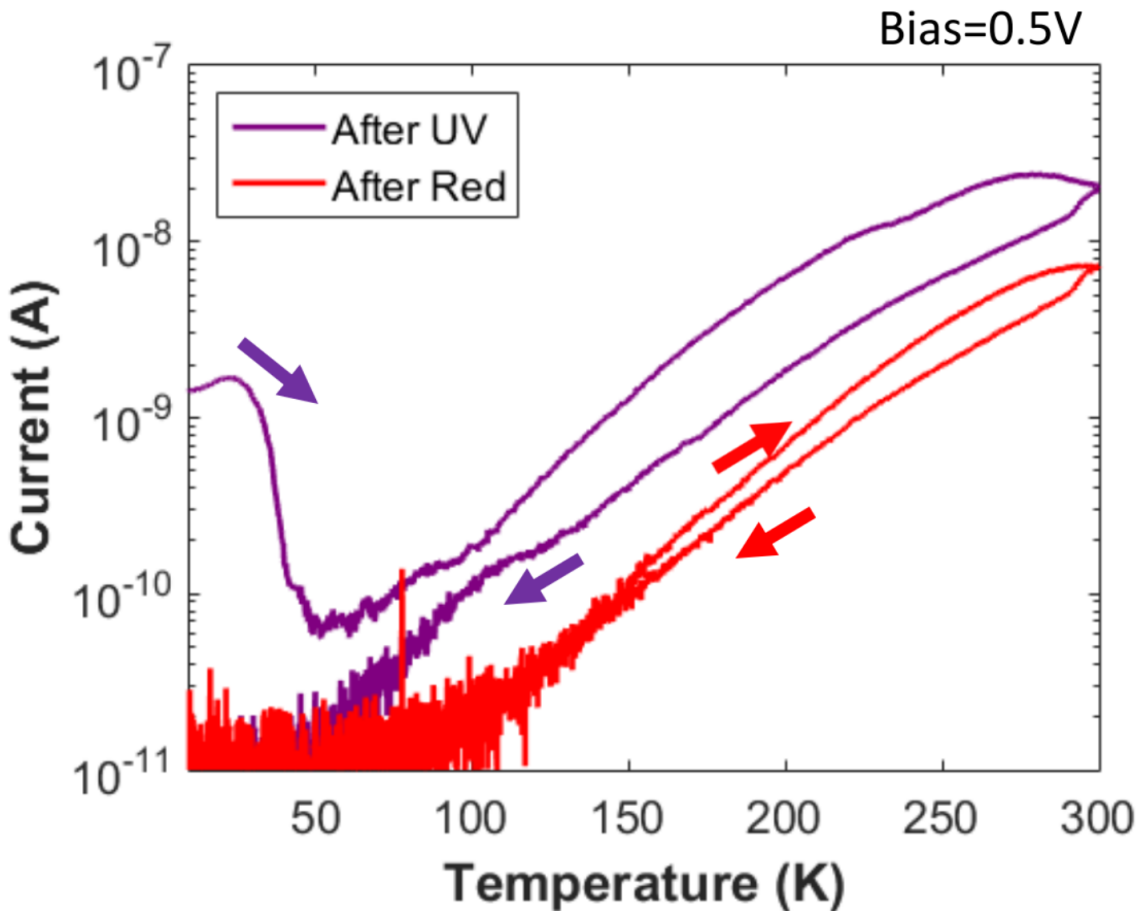

Figure 6.13: Response of MoS_2's ON and OFF states to temperature sweeping. Plot showing a temperature sweep up from 10 K to 300 K and back in darkness, in the aftermath of both ultraviolet and red illumination. The arrows indicate the direction of the sweep for adjacent data. The current is plotted on a logarithmic axis.

One curious trait of this graph is the fact that the sample primed with ultraviolet light starts out with its current increasing in response to increasing temperature, as one might expect due to thermal effects. However, this reaches a maximum at approximately 25 K, after which we see a precipitous drop in current until approximately 50 K. At this point, the decrease is reversed, and the current begins steadily rising again; still, it does not recover a value equal to this initial peak again until the temperature reaches over 150 K - quite a significant increase. This behavior is presumably linked to the phase change STO experiences in this temperature range.

Focusing on the end of the downsweep, it is apparent that by around 50 K, regardless of the priming of the sample, the current output is identical, indicating a complete erasure

of the aftereffects of optical gating. That this temperature corresponds with the minimum value of the upsweep for the ultraviolet-primed case seems unlikely to be coincidental: this temperature is clearly fundamentally linked to a change in how the effect operates. This will be further discussed in Section 6.5.

6.5 Analysis

The data in this section is best analyzed in comparison with past work in optical gating, since the conjunction of all these experiments in several different material systems offers a richer insight into how two-dimensional materials in general behave when subject to this phenomenon. Therefore, this section will heavily focus on comparison with the pre-existing literature discussed in Section 5.1.3.

Due to the band structure of graphene, it should be analyzed in comparison with the work on $(Bi,Sb)_2Te_3$ by Yeats *et al.* [1], since this topological insulator also possesses a Dirac cone band structure. Our data for graphene very strongly resembles the data shown in that paper: we may clearly see how the resistance steadily increases under exposure to ultraviolet light as the material's Fermi level is increased, reaching a maximum resistance at the Dirac point and then steadily decreasing again as the conduction band is scaled. The persistence of this adjustment in resistance, with some relaxation, is visible in the dark period between doses. Then, again, red light is able to increase the resistance up to the Dirac point whereupon the resistance decreases once more, corresponding to a drop in Fermi level down into the valence band. While the analogous data showing the "stepping" of this effect due to subsequent pulses of light is not presented at 10 K in this chapter, it is demonstrated on graphene at room temperature in an analogous set-up in the following chapter, as may be seen in Section 7.10.3. Thus, we may conclude that, as expected, these two systems display similar responsivity to the optical gating technique.

In analyzing our results with MoS_2, we first note that the source of the photocurrent

during illumination is probably linked to the MoS_2 alone. Monolayer MoS_2 is known to show photoconductivity through the visible spectrum, increasing as wavelength decreases, and the rate of increase during illumination that we observe, as well as the drop-off upon cessation of illumination, is consistent with previously-observed data [112]. Few-layer MoS_2 on SiO_2 shows a photocurrent in response to 254 nm ultraviolet light; however, the resulting decay after cessation of illumination has a time constant of approximately a minute, and no mention was made of a persistent state [113]. Comparing these results to photocurrent measurements of an MoS_2 trilayer on Si taken upon exposure to 254 nm light, we see some similarity in the increase of current during illumination, and in the long persistence of that effect after illumination; however, our photocurrent plummets significantly almost immediately upon cessation of illumination, in contrast to the data observed under vacuum in that experiment, where the induced current maintains roughly the same value [114].

Nonetheless, we may dismiss the possibility that the effect we observe as a whole is uniquely created by the MoS_2, since red light at our wavelength would be expected to also induce a photocurrent, not eliminate the persistent current [112]. Since the persistent state after illumination had an identical value to the maximum current achieved via electrical gating, we conclude that this state is indeed equivalent to the electrically-generated ON state, and that optical gating therefore functions analogously to electrical gating. Intriguingly, higher power densities of ultraviolet light, while imparting a larger photocurrent, may result in a faster decay of the persistent state.

The majority of the work in MoS_2 presented in this chapter receives its closest comparison in the work of Liu *et al.* using two-dimensional black phosphorus [92]. Their preliminary measurement of MoS_2, as shown in their Supplemental Information, is similar to the initial data set shown in Figure 6.4, confirming that our measurement set-up and sample provide consistent results with theirs, and guaranteeing the comparability of our data.

A significant note to be made is that for black phosphorus, below-band gap light induces the increase in current while above-band gap light quenches it, in direct contrast to MoS_2,

where the effects of the light are reversed. Liu *et al.* assert that this is due to the fact that ultraviolet light, via driving migration of electrons, creates a positive charge on the surface: since black phosphorus is *p*-type, its native carriers are holes, which are quenched by the influx of electrons stimulated by this positive charge, resulting in a diminished current [92]. The opposite happens for the *n*-type MoS_2, whose native carriers are electrons; thus, the positive surface charge under ultraviolet illumination greatly increases the current seen in the material. While they only had a preliminary result for MoS_2 to demonstrate this, our greater data set fully supports this interpretation: we are able to demonstrate the upward "stepping" effect of the MoS_2 current in response to ultraviolet light exactly analogously to the stepping they show occurring in the black phosphorus current in response to red light.

The comparison of the time scales of the different illumination types we see in MoS_2 also strongly supports the hypothesized mechanism of the effect, put forth in their work as well as in the seminal work by Yeats *et al.* [1], and described in detail in Section 5.1.2. Regardless of whether ultraviolet light has an amplifying or quenching effect on the current induced in the two-dimensional material, its effect is extremely fast - almost instantaneous - due to the rapid excitation of many defects near the substrate surface, generating an electric field in the STO, and the possible transfer of electrons to the layer above. Conversely, the red light takes effect at a much slower rate, since the relaxation of the substrate's electric field is generated via scattering induced by a weaker-energy stimulus. This slower time scale enables a downwards stepping in the current of MoS_2, using subsequent red exposures, as we have shown. Such a feat was not demonstrated in black phosphorus, presumably since it was observed that only two seconds of ultraviolet illumination were sufficient to totally quench the optical gating effect for that material - extremely significant since a much longer dose was necessary to achieve the saturation current in MoS_2. Due to the fact that Liu *et al.* do not specify the power density of ultraviolet light being used, it is ambiguous whether this setting may have been too high to enable more gradual stepping. Since the ultraviolet-induced effect is much stronger and more immediate than the red-induced effect, further

experiments with lower power density light would be necessary to show tunable bidirectional control for p-type materials, as we have demonstrated here for the first time in an n-type material.

Liu *et al.* further observed an ON/OFF ratio exceeding 10^5 in black phosphorus. We may compare this with the two ON states observed in MoS_2. Unlike in black phosphorus, MoS_2 displays a significant photocurrent as a result of the ultraviolet illumination, which couples with the optical gating effect to produce an ON/OFF ratio exceeding 10^5. In the absence of illumination, however, the MoS_2 ON/OFF ratio was seen to be only on the order of 10^2, a much lower value. Both of these values are much lower than the maximum value of 10^8 which has been observed before in MoS_2 [63]. This ON/OFF ratio can reasonably be concluded to be dependent on the sample itself, since a similar ON/OFF ratio to the persistent one in MoS_2 was achieved via electrical gating.

The time scale of the dynamics of MoS_2 in the aftermath of ultraviolet illumination was further examined. It was observed that the transient effects of illumination were still significant in the minutes following cessation, with the impacts not seeming to be well-characterized by a single exponential function, but roughly characterized by a time constant of about an hour. Meanwhile, the persistent effects after a substantial period of darkness showed a time constant for the persistent effect of order days, comparable to the long time scales observed in the literature [1] [92] [93]. Finally, the effect of red illumination was neatly characterizable by an exponential fit.

Our experiment looking at the electrical gating of MoS_2 after priming it with ultraviolet light confirms that the effects of the two types of gating are initially additive, since the initial ultraviolet priming offsets the gate voltage sweep curve. However, this additivity may be quenched by lowering the gate far enough into the negative, as the subsequent sweep reveals. Thus, we conclude that optical and electrical gating are transiently additive so long as the Fermi level is not reduced significantly via electrical gating.

Sweeping the temperature after initially priming with alternatively ultraviolet and red

light also demonstrates some persistence of the effect through increasing temperature, as the current observed in the material is substantially different depending on which light it had been exposed to prior to the temperature sweep. However, this distinction is quenched on the downsweep at around 40-50 K. Interestingly, this is very close to the temperature regime at which the ultraviolet-primed upsweep also experienced a local minimum in current, and is very near the quantum paralectric phase transition of STO [15]. This data is comparable to the thermal cycling to different temperatures performed by Yang *et al.* with FeSe on STO [93]. In that work, the FeSe was placed in a superconducting state via ultraviolet light, and then cycled up from 16 K and back in darkness. They observed a significant increase in measured resistance in the temperature region around 40 K, as well as another significant increase close to 150 K [93]. Coincidentally, this latter value also appears in our work, being roughly where the ultraviolet-primed sample has a current equal in value to its value at 10 K; however, this seems unlikely to have deeper significance.

Thus, this work has provided another example of a Dirac cone band-structured material responding to optical gating, as well as presented a more thorough exploration of the responsivity of an n-type material with an ultraviolet-induced photocurrent to this effect. Sensitive bidirectional tunability of the material current using pulses of both light colors has been demonstrated for the first time in a band gapped material. Additionally, temperature sweeping emphasized the significance of the quantum paraelectric phase change in altering the persistence of the effect across temperature changes. By adding graphene to the list of materials which have been gated using this effect, and providing a more thorough investigation of MoS_2's responsivity, the broad applicability of this technique to a variety of two-dimensional material systems has been further shown.

Chapter 7

Kelvin Probe Force Microscopy Measurements

The measurements described in this section were performed by the author and Joost van Bree, in the lab of David D. Awschalom, as featured in a manuscript currently being written. Help was also provided by Andrew L. Yeats in experimental design. Assistance in sample preparation, such as graphene transfer and annealing, were further provided by Grant T. Smith and Samuel J. Whiteley. Additional theoretical analysis was also provided via collaboration with Meng Ye, working in the group of Giulia Galli.

7.1 Introduction

To date, the papers in the literature relating to the optical gating effect (*see Section 5.1.3*) have focused upon, essentially, its applications: how the effect impacts two-dimensional materials placed upon STO. However, to discover more about how the effect itself works, it is important to investigate how bare STO itself responds to light. Furthermore, using techniques to alter defect populations should help shed light upon the identity of the defect responsible for this effect. Such knowledge is needed to further engineer and optimize the optical gating effect in STO and/or other materials. Accordingly, we used the KPFM tech-

nique (detailed in Section 5.2) to look at how illumination affects the surface potential of bare STO. We furthermore performed an annealing study on several different samples to ascertain the effects that the resultant change in defect populations would have on the optical gating response. Additionally, to provide good comparison with the work in the previous chapter as well as to get a closer look at the workings of the effect on a two-dimensional material, we performed KPFM measurements upon a sample of graphene placed on STO.

7.2 Samples

Samples consisted of both (111) and (100) oriented Verneuil-grown STO, received from the companies MTI, Crystal, and PSC. One samples was doped with Fe (0.005%); others had not been subjected to deliberate doping (though background defect concentrations are known to be relatively high in Verneuil-grown STO). One sample had a single layer of graphene (from Graphenea) "easy-transferred" (using water and low-temperature hot-plate annealing) [115] onto its surface. Other samples were measured as-received, and later subjected to a range of annealing conditions prior to subsequent measurements.

7.3 Set-Up

To create a set-up to measure the effects of ultraviolet illumination upon the surface of our samples, we modified a room-temperature MFP3D-Bio AFM produced by Asylum Research to incorporate optical illumination sources. An electrically conductive Ti/Ir coated tip was used to perform the measurements. Focused 375 nm light was used to provide the above-band gap stimulation used to incur the optical gating effect on the bare substrate. Meanwhile, defocused 660 nm light was utilized as the below-band gap stimulation. The light sources were regulated via the programmable DAC outputs of the AFM system. These program capabilities allowed the measurement of contact potential over long time periods, with fully-programmable measurement sequences in which the illumination was automatically switched

on and off. These sequences incorporate automatic periodic (every 100 s) retraction and approach of the tip, to compensate for tip-sample distance variation over long measurement times (resulting in visible small jumps in some time-traced measurements of potential). Measurements were conducted with the AFM enclosure shut to prevent the interference of external light sources. All measurements were conducted at room temperature. The temperature and relative humidity inside and outside the AFM enclosure were controlled and monitored to minimize thermal drift and to ensure humidity changes were not impacting measurements.

Some additional four-point probe measurements were performed utilizing a probe station. This station also had an enclosure, preventing ambient light from affecting it during measurement, and was modified to allow optical access at the top to enable stimulation via 375 nm and 660 nm light.

7.4 Spatial Measurement of Contact Potential

A confirmation of the general principle behind the experiment, as well as the spatial dependence of the optical gating phenomenon, may be seen in Figure 7.1 which depicts the effect of ultraviolet illumination on the contact potential difference V_{CPD} of a STO sample ((111) orientation, undoped, previously subjected to 30 minutes annealing at 1050^{o}C under oxygen and subsequently cooled at approximately 75^{o}C/s). In (a), the sample has previously been subjected to 660 nm light in order to ensure that prior illumination has not altered the spatial potential of the sample. Indeed, it is greatly homogeneous in contact potential value, with the only significant deviations being small points on the right hand side of the image. These spots correlate with the topographical AFM image of the sample in (b), showing them to be small specks of dirt on the surface distinct from the wafer itself and thus unrelated to the measurement. After the application of ultraviolet light (with the spot size and shape shown in the optical image in (d)), the contact potential shows a significant change, decreas-

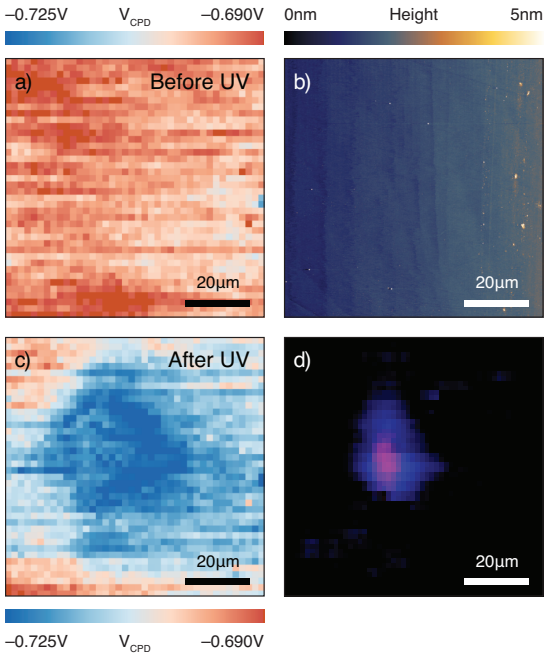

Figure 7.1: KPFM spatial measurements of STO surface potential in response to ultraviolet illumination. (a) KPFM measurement of the surface of STO before ultraviolet exposure. (b) Topographical AFM image of the surface. (c) KPFM measurement of the surface of STO after ultraviolet exposure. (d) Optical image of the ultraviolet spot.

ing by approximately 0.035 V. This substantial change is a clear confirmation of the fact that ultraviolet illumination has a quite noticeable impact on the surface potential of STO. Moreover, it demonstrates that the effect is indeed local: the strongest change is seen in the region subjected to direct illumination under the spot, as the region with the greatest decrease in contact potential resembles the shape of the ultraviolet spot. Outside of this region, there is much less change in the surface contact potential, indicative of the fact that the effect is largely, but not entirely, confined to the illuminated area.

7.5 Ultraviolet Dose Dependence

The response of bare STO (MTI, (111) orientation) to ultraviolet illumination was quantified using single-point measurements. Here, the contact potential was monitored at a single point on the bare STO before, during, and after ultraviolet illumination. A typical curve depicting the contact potential's response to ultraviolet illumination may be seen in Figure 7.2 (a).

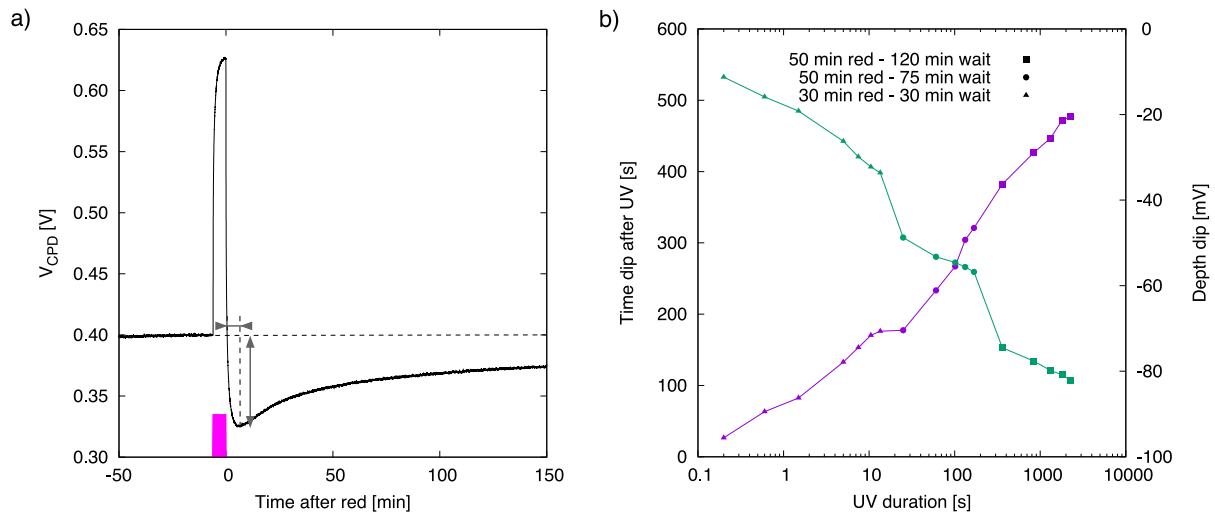

Figure 7.2: Comparison of ultraviolet dose dependence's impact on the subsequent time (after cessation of illumination) and depth of the dip in contact potential. (a) displays a typical measurement, with notation showing where this minimum would be found on a data set. (b) depicts the accumulated data characterizing these dips, with purple data corresponding to the time of the minimum (left axis) and green data to the depth of the minimum (right axis); time is displayed on a logarithmic axis. Different data point types display the different pre-ultraviolet treatment of the sample.

Interestingly, there is a significant spike in the contact potential of the bare STO only during ultraviolet illumination, indicating an increase in the negative charge of the surface taking place. This massive accumulation of negative charge could possibly be indicative of the creation of a 2D electron gas (2DEG) at the surface of the STO due to the continual stimulation of negatively charged defects close to the wafer's surface resulting in a downward-bending of the conduction band, similar to the ultraviolet-reactive 2DEG observed by Meevasana *et al.* in a La-doped sample of STO [42]. Upon cessation of illumination, this accumulation of negative charge dissipates. However, the contact potential falls to below the initially-held value, indicating a drop in Fermi level as the surface has become more positive due to the electrons from the excited defects drifting further into the bulk, leaving a net positive charge in comparison to before ultraviolet stimulation.

Of particular interest is the fact that after illumination, the contact potential reaches a minimum value, whereupon it begins relaxing upward again. To characterize the immediate response to ultraviolet light, we therefore chose to focus on this minimum, looking at both the time taken to reach the minimum value after ultraviolet light had been turned off, as well

as the ultimate depth that was reached. This was measured as a function of the ultraviolet dose applied. This data is plotted in Figure 7.2 (b). Note that while the samples had previously been subjected to different prior lengths of red exposure and subsequent relaxation in darkness, they were believed to be roughly equilibrated due to the long duration of each used.

Looking at the response, there is a clear direct relationship between the duration of ultraviolet exposure (as shown logarithmically) and the time necessary to achieve the subsequent minimum contact potential. This makes sense since the initial plummet would be expected to be due to the negative charge accumulation dissipating upon cessation of stimulation and relaxation of any conduction band bending. With more excited charges present, the time necessary for these to lose energy and diffuse back into the bulk would be expected to increase correspondantly.

Furthermore, the depth of the minimum attained is also directly correspondent to the duration of illumination. This logically makes sense when we consider that the longer the illumination takes place, the more the STO close to the surface is being depleted of defect-linked carriers, which are being excited and then drifting deeper into the bulk. Once the accumulation of charge caused by ultraviolet illumination has dissipated, the effect of this depletion becomes clearly apparent, as the relative absence of these negatively-charged carriers results in a far more positive potential at the surface of the STO.

7.6 Comparison of Different Annealing Conditions

A single sample with (111) orientation (obtained from MTI) was subjected to a broad variety of annealing treatments, and the effects compared at a single point within the illumination zone, to elucidate the effects of these preparations. Chronologically, the treatments took place as follows: after an initial measurement of the sample as-received, the sample was subsequently subjected to annealing in a tube furnace under an atmosphere rich in O_2 at

500°C, 700°C, 900°C, and finally 1050°C; then, the sample was subjected to annealing under an oxygen-poor atmosphere of H_2 and Ar ("forming gas") at 500°C, and finally 1050°C. For all these cases, the sample was annealed for a total of 30 minutes, then cooled at a rate of 75°C/s. It was expected that oxygen anneals would annihilate oxygen-based vacancies within the substrate; that forming gas anneals would help to reinstate them; and that sufficiently high temperatures would extinguish the responsible defect state.

Figure 7.3 (a) shows how the sample responded to repeated pulses of ultraviolet illumination (1.5 second duration). Notably, all showed a decrease in overall contact potential across the duration of the experiment. In all but one case (that of the STO annealed at 1050°C under H_2), the effect of a pulse was a rapid change in the contact potential, which then proceeded to decay over the dark time to an overall value lower than prior to the pulse. Thus, an effective downward stepping of the contact potential is visible in each of these cases.

However, a clear distinction is visible between the STO which had not been subjected to any heat treatment and the sample post-oxygen annealing: namely, a positive peak is visible on the untreated STO and the STO annealed under forming gas at 500°C during the ultraviolet illumination, followed by a decrease in contact potential; however, the oxygen-annealed cases do not show any such peak.

After the sample was annealed at 1050°C, it does not display any notable response whatsoever to the ultraviolet illumination; instead, its contact potential is relatively flat, with a slight downwards slope. The general decreasing trend is clearly much smaller in magnitude than the contact potential decrease incurred in all other samples by the pulse sequence, so the cause of this slope may be dismissed as the predominant effect causing the general downward trend seen in responsive samples. Instead, this was interpreted as solely due to drift, which is within the typical range of stability of the potential measurement over this time period. This lack of responsivity may indicate that the defect is no longer present in the sample to be activated, or is in a state where it can no longer be activated. The sample after its annealing at 500°C under H_2 differs in that very small positively-signed peaks are

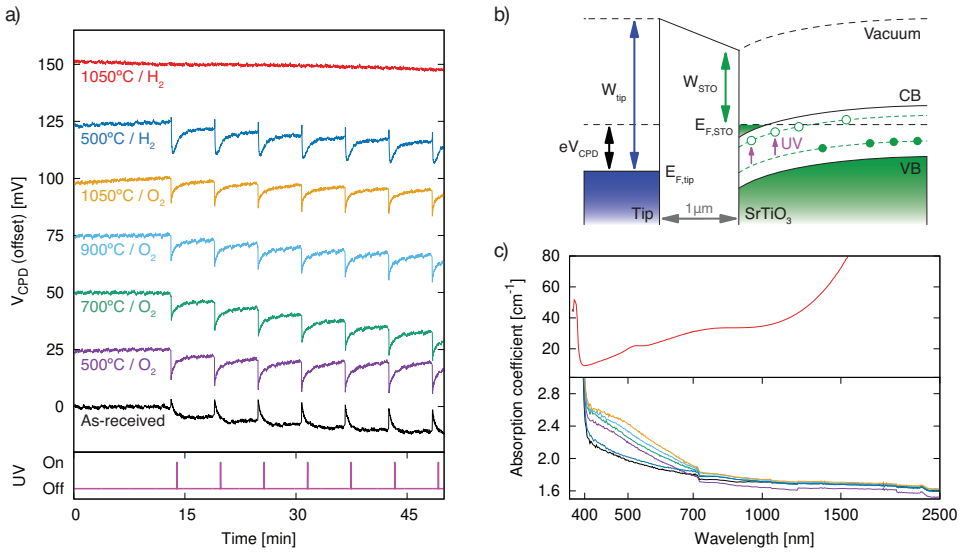

Figure 7.3: Plot of KPFM response to ultraviolet pulse and absorption spectra for different annealing conditions. (a) KPFM data for a series of 375 nm ultraviolet pulses performed on the same sample as-received (black) and at different annealing conditions (other colors; conditions noted at left) after a red reset (not shown). Data is offset for clarity, with the chronological history of the sample going from bottom to top. The lower inset figure depicts the timing of the ultraviolet pulses. (b) Cartoon depicting the bands of the AFM tip and the surface of the STO during ultraviolet exposure, demonstrating the hypothesized downward band bending and formation of a 2DEG. (c) Absorption data for the sample after different anneals; the color of the line corresponds to the colors in (a). Note that this sample is Sample 2, as referred to in Table 7.1. *Cartoon courtesy of Joost van Bree.*

instantaneously visible during ultraviolet illumination; however, this is still followed by an overall significant decrease in contact potential, which relaxes back to a steady-state value.

Figure 7.3 (c) displays the absorption coefficients of the sample after different annealing conditions. Immediately, it is apparent that the sample subjected to annealing at 1050°C under H_2 possesses a much higher absorption across the visible spectrum, requiring a scale with values around an order of magnitude greater in the visible spectrum, and drastically increasing as the wavelengths extend into the infrared. The shape of the absorption coefficient function also displays no significant similarity to any other cases measured beyond an initial decrease in absorption occurring at around 400 nm, which is the absorption edge; while all other preparations display a subsequent decrease in their absorption coefficient as wavelength increases, the absorption coefficient for this treatment substantially increases starting in the low wavelengths of the visible spectrum and proceeding on through the infrared. This is expected to correspond to the creation of many free carriers which are able to absorb

any given wavelength, drastically impacting the absorption spectrum. Therefore, this final treatment may be seen to have had a huge effect not only on the STO's responsiveness to stimulation in optical gating, but also on the optical properties of the sample as a whole.

Of the other annealing conditions measured, the absorption spectra are less dissimilar, but roughly fall into two groupings. All cases in which the sample were been exposed to O_2 during annealing feature a notable "bump" in their spectra across the visible spectrum, as compared to the untreated sample. These appear similar to the absorption band which has been attributed to iron defects in the absence of vacancies, specifically to the oxidative Fe^{4+} defect state [116]. This indicates that the charge state of iron defects, and their conjugation to oxygen vacancies, in the sample are being changed as a result of the anneals. In comparison, the sample when re-annealed at 500°C under H_2 displays a very similar absorption coefficient spectrum to the untreated sample, with only a slight and essentially constant increase in value. Thus, this 500°C H_2 anneal step seems to have effectively reversed the effect of the O_2 anneals on the iron defects in the sample.

7.7 Comparison of Different Samples Under Annealing

A variety of distinct samples were then compared in order to ascertain the difference made by distinctive annealing conditions, dopants, and manufacturers. These samples are labeled numerically to differentiate them; a concise description of their properties may be found in Table 7.1.

TABLE 7.1: Samples and Annealing Conditions Used for Multi-Sample Annealing Study

Sample Number	Supplier	Doping (%-weight)	Anneal Time [min.]	Approx. Cooling Rate [°C/s]
1	MTI Boule 1	-	30	75
2	MTI Boule 1	-	30	75
3	MTI Boule 2	-	60	10
4	MTI	0.005% Fe	60	10
5	PSC	-	60	10

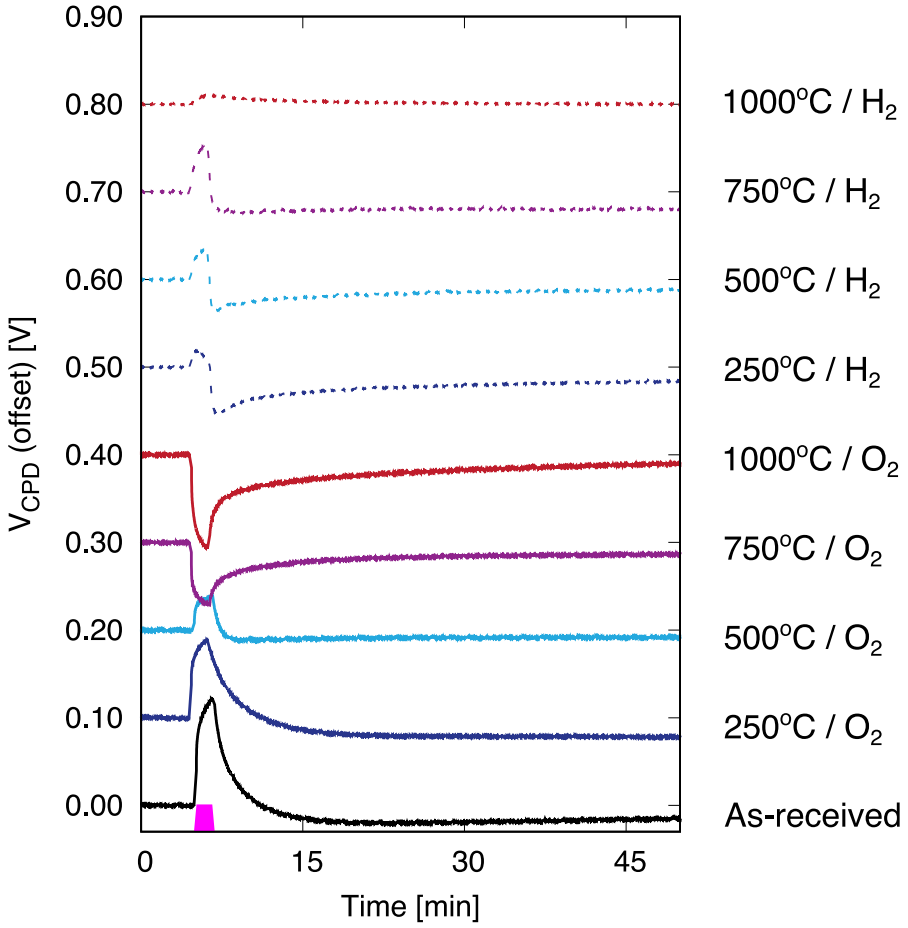

Figure 7.4: Depiction of the pulse sequence used in measurements for Samples 3, 4, and 5, with data displayed for different annealing steps coming from Sample 5.

Sample 1 was notably only subjected to annealing under O_2 (at 500°C, 700°C, 900°C, and 1050°C), while Sample 2 (annealed under O_2 at those temperatures) was also annealed under H_2 but only at 500°C and 1050°C. For both Samples 1 and 2, an annealing time of 30 minutes was chosen, with a cooling rate after of 75°C/s. Samples 3, 4, and 5 were annealed at four different temperatures (250°C, 500°C, 750°C, and 1000°C) under both O_2 and H_2, using anneal durations of 60 minutes followed by a cooling rate of 10°C/s. These anneals occurred subsequently, first going from low to high temperatures under O_2, and then from low to high temperatures under H_2.

Notably, Samples 3, 4, and 5 were subjected to a different pulse duration than Samples

1 and 2 (who were subjected to pulses as may be seen in Figure 7.3). We do not expect that this should have qualitatively change the behavior of the samples in response to different annealing steps, since the ultraviolet duration dependence in Section 7.5 showed that the behavior is essentially the same. Moreover, the majority of our analysis derives from intra-sample comparisons. For the sake of completeness, a figure depicting analogous data to Figure 7.3 (a) for Sample 5 and displaying the utilized pulse sequence is shown in Figure 7.4.

Figure 7.5 accumulates the data associated with these measurements. Figure 7.5 (a) shows a sample measurement of V_{CPD} before, during, and after a pulse of ultraviolet light. It also serves to delineate the meaning of each of the subsequent parts of the plot: (b) displays the average V_{CPD} measured prior to illumination; (c) displays the change in V_{CPD} incurred during the illumination; and (d) displays the change in V_{CPD} overall before and after the illumination took place. Due to degradation during use, different AFM tips were used throughout this set of measurements; for clarity, these are distinguished with different data point symbols.

7.7.1 Change in Absolute Contact Potential

First examining Figure 7.5 (b), it is clear that all samples regardless of provenance, and regardless of whether or not they were doped with iron, displayed essentially the same initial V_{CPD} prior to illumination in the absence of treatment. This V_{CPD} is approximately 0.3 V. Our calibration (*see Section 7.12.1*) indicates that the work function is approximately 4.5 eV. Taking the electron affinity of STO to have a value of approximately 4.1 eV [27] [28], the Fermi level is therefore approximately 0.4 eV below the conduction band.

How the sample was treated resulted in some difference. Samples 1 and 2, which were annealed in each treatment for half the time of their fellows (note also that these two samples did not receive an annealing treatment at 500^{o}C under O_2), showed clear distinction in their overall trends after O_2 anneals as compared to Samples 3, 4, and 5, which reacted largely the same under oxygen anneals. One possible source of some of this discrepancy is indeed

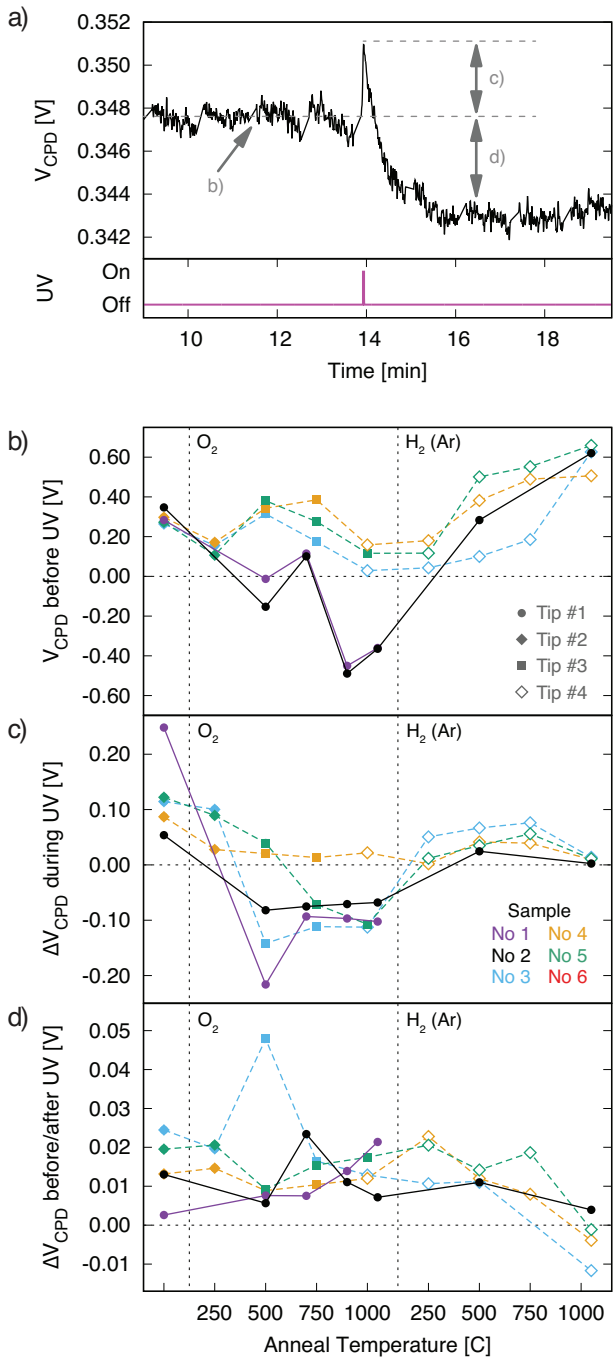

Figure 7.5: Measured response of contact potential to ultraviolet pulse for different samples and different annealing conditions. (a) General example of contact potential reaction to an ultraviolet pulse. The different labeled parts correspond to further subplots in this figure. (b) Typical pre-ultraviolet contact potental value for different samples and different annealing conditions. (c) Typical height of contact potential peak during ultraviolet exposure with pre-ultraviolet value subtracted. (d) Typical decrease in value of contact potential following ultraviolet exposure relative to initial value. The separate sets consisting of Samples (1, 2) and Samples (3, 4, 5) were subjected to different illumination conditions. Chronologically, each data set is ordered from left to right, with different symbols representing the different AFM tips used.

the reduced anneal time, and number of anneals, to which the samples had been subjected. Samples 3, 4, and 5 all display an initial dip upon their first anneal, followed by a peak which decreases upon subsequent anneals (this peak being only marginally greater than the untreated contact potential).

Another possible source of discrepancy is the fact that multiple tips were utilized for Samples 3, 4, and 5. Examination of data taken after the same (250^{o}C O_2) anneal, when Tips 2 and 3 were both used, shows a contact potential discrepancy of around 0.3 V. However, the subsequent tip change (at the 1000^{o}C oxygen anneal, where a new tip was used for two samples) seems to show consistent values across the different tips. Since approximately the same final value is obtained after the 1000^{o}C forming gas anneal of these three samples as for the 1050^{o}C anneal of Sample 2, and since this value corresponds to cessation of the effect for all samples measured, we may infer that this value is accurate, and that therefore only Tip 2 (the first tip used for Samples 3, 4, and 5) was likely to have been problematic, giving us a value 0.3 V too low - thus, for Samples 3, 4, and 5, the contact potential during the oxygen anneals probably does not actually dip then then peak then decrease again, but in fact is consistently decreasing, as we see in Samples 1 and 2. Nonetheless, despite this possible source of error, we may still observe trends in behavior for data subsets using the same tip.

Ignoring the different temperatures of the anneals and the actual contact potential values measured, Samples 1 and 2 do actually follow the same general trend as Samples 3, 4, and 5. It is possible that the first anneal decreases the contact potential regardless of temperature, with further annealing briefly increasing the contact potential before it drops significantly again. It is also interesting that Samples 1 and 2 have much lower contact potential values overall across the O_2 anneals, corresponding to lower Fermi levels, despite the fact that the data from the last two tips used for Samples 3, 4, and 5 is believed to be accurate in relation to the data from Samples 1 and 2: possibly Samples 3, 4, and 5 have less distinctly negative values because of relaxation and defect re-equilibration during the much longer cooldown period mitigating the severity of the effect, whereas the relative

quench used on Samples 1 and 2 does not allow this to take place. Thus, rapid cooling may enable a greater tuning of the initial contact potential V_{CPD} than slower cooling rates do. Since there is a notable difference arising from these cooling rates, we may infer that the equilibration time is on the order of minutes, indicating that the duration of annealing (30 versus 60 minutes) was unlikely to be as influential in this data as the cooling rate.

Samples 1 and 2 reach a minimum contact potential during oxygen annealing of approximately -0.4 V after a 900^{o}C O_2 anneal, corresponding to a total work function + Fermi level (with respect to the conduction band) of approximately 5.7 eV. This indicates that the Fermi level is approximately 1.6 eV below the conduction band. Samples 3, 4, and 5 ultimately reach a contact potential between 0-0.2 V, corresponding to a sum of work function and Fermi level of approximately 4.7-4.9 eV, or Fermi levels approximately 0.6-0.8 eV below the conduction band.

During the subsequent forming gas anneals, however, Sample 2 behaves very similarly to Samples 4 and 5 despite the shorter duration of each anneal step and despite the fact that it was only subjected to half the number of anneal steps (note that Sample 1 was not subjected to these later anneals). Thus, these H_2 anneals seem to take effect extremely quickly, and the effects are not relaxed by a longer cooling period. Intriguingly, Sample 3 demonstrates slightly different behavior during the anneals at 500^{o}C and 750^{o}C, which does not seem to be reflected in the illumination reactions of the sample during these anneals, as shown in Figures 7.5 (c) and (d) (where Sample 3 displays quite typical data compared to the others). Thus, this distinct pattern in initial contact potential does not seem to make a difference overall on the optical gating performance of Sample 3, and therefore, while it remains a mystery, is not believed to be significant. In general, the subsequent anneals consistently correspond to the raising of the Fermi level towards the conduction band, as seen by a steady increase in contact potential.

Ultimately, the 1000^{o}C/1050^{o}C reductive anneal leaves all samples with a contact potential of approximately 0.6 V. This corresponds to a sum of work function and distance

from Fermi level to conduction band approximately equal to the electron affinity - thus, the Fermi level has seemingly entered the conduction band. This matches the assessment of the absorption spectra for these annealing conditions, which indicated the presence of a plethora of absorptive free carriers.

Overall, one of the most important takeaways from Figure 7.5 (b) is that there is a clear difference in the measured initial contact potential for individual samples after almost all of the different annealing steps. This is a clear indication that the Fermi levels of the samples as a whole have been affected by the treatments to which they are exposed. One important thing to note is that, for the three samples (Samples 3, 4, and 5) who were subjected to the 250^{o}C H_2 anneal after the 1000^{o}C O_2 anneal, there is almost no difference in contact potential present between the two conditions. This indicates that this anneal does not actually have any impact on overall Fermi level: a greater temperature is required during a reduction anneal to change it.

7.7.2 Peak During Ultraviolet Excitation

Figure 7.5 (c) represents the magnitude and sign of the resultant instantaneous peak upon ultraviolet illumination. A positive sign indicates that the Fermi level is being transiently raised, presumably due to the accumulation of negative charge carriers near the surface, whereas a negative sign indicates it is being transiently lowered. From the data taken from Samples 3, 4, and 5, it seems that while an initial anneal under O_2 at 250^{o}C slightly decreases the magnitude of the peak, the peak retains its positive value. This changes after additional O_2 anneals at higher temperatures. Samples 1, 2, and 3 - all sourced from the same vendor, MTI - all transition to negative peaks once the O_2 anneal at 500^{o}C has been performed, as was observed earlier in Figure 7.3 (a). Sample 5, sourced from PSC, still retains a positive peak under these conditions, though the magnitude has decreased further; the next anneal leaves the peak firmly negative. This discrepancy may be due to differences in impurity levels between the two vendors during their growth processes and/or post-growth annealing

conditions. Overall, however, one might link the loss of a positive peak during ultraviolet illumination to factors impacting the band bending that occurs in untreated samples. Since this band bending, and the incipient illumination-dependent accumulation of negative charge, have been hypothesized to relate to the presence of oxygen vacancies near the surface [42], removal of these vacancies via oxygen annealing may account for the change in transient behavior: the conduction band is no longer being bent downward, resulting in the lack of accumulated negative charge at the surface (potentially a 2DEG), and thus the negative sign of the peak is due to the positivity imbued on the surface as negative charges migrate deeper into the bulk.

The forming gas anneals, meanwhile, seems to more-or-less reverse this negative peak effect from the O_2 anneal, as was previously seen in Figure 7.3 (a). All samples behave essentially identically during these anneals, immediately taking on a positive-magnitude transient peak during ultraviolet illumination for all anneals below 1000^{o}C/1050^{o}C, as had previously been seen. This data set, however, further clarifies that even a weak (250^{o}C) anneal under H_2 is enough to reverse the effect of the oxygen anneals. All of them similarly have no peak appear after the 1050^{o}C anneal. The fact that there is still a positive peak for the three samples (Samples 3, 4, and 5) subjected to 750^{o}C annealing narrows down the temperature range within which the impact of optical gating is quenched: it must lie between 750^{o}C and 1000^{o}C.

Special attention should be paid to the Fe-doped sample when considering this subplot. Notably, throughout all the oxygen anneals, the instantaneous peak produced during ultraviolet illumination always retains a positive value. Thus, some iron-related defect is individually and transiently responsive to the ultraviolet light to a significant degree in comparison with the undoped samples. This is very plausibly a result of a larger population of the ultraviolet-responsive Fe^{3+}-V_O defect complex [34]. However, the Fe-doped sample behaves identically to all other samples during the four forming gas anneals, indicating a change in this defect's oxidation state - consistent with the absorption differences imparted

by these H_2 anneals which were seen in Figure 7.3 (c).

7.7.3 Change in Contact Potential Before/After Illumination

Figure 7.5 (d) depicts the overall change in the contact potential prior to ultraviolet exposure compared to the relaxed period after ultraviolet exposure has taken place. The magnitude of this change is relatively small compared to the instantaneous peak produced at illumination, indicating that the strongest impact of annealing is seen transiently during illumination, while the steady-state effect is much less intense. This difference is positive in nearly all cases, representing the decrease in Fermi level incurred by the illumination step, and corresponding to decreases in contact potential observed in Figure 7.3 (a); the only exceptions to this occurred during the highest-temperature forming gas anneal which destroys the effect.

7.7.4 Discussion of Iron-Doped Sample

As a whole, this experiment also enabled an observation of the effect that iron doping produced on the overall Fermi level, as well as during and after ultraviolet illumination, throughout annealing treatments. The only significant discrepancy which the iron-doped sample (Sample 4) showed relative to the others was during the instantaneous response to ultraviolet light portrayed in Figure 7.5 (c), where its peak was always non-negative in value; however, this doping had no effect on the steady-state parts of the effect, with the sample's behavior in Figures 7.5 (b) and (d) being more or less identical to the behavior of undoped samples. Also, in general annealing has no discernable effect on the samples' demonstration of optical gating (up to the 1000°C/1050°C forming gas anneal which destroys the effect), despite the fact that annealing is expected to change the charge state of iron defects [22], which is supported by the absorption data obtained for different anneals, as well as density functional theory calculations performed by Baker *et al.* [44] (further discussed in Section 7.7.6). Thus, we may conclude that while the iron-related defects in the sample appear to be

transiently responsive to ultraviolet light, they do not seem to be responsible for the most important aspects of the optical gating effect. However, these defects may play a role in charge transfer from the surface to a two-dimensional material on top of STO that may take place during the transient ultraviolet illumination, as hypothesized in the literature [92] and in Section 7.10.2, and thus may ultimately still be impactful to the *extent* of the effect as seen on such materials.

7.7.5 Visual Differences Due to Annealing

Clear visual differences were also qualitatively observed in the samples due to annealing (as are more quantitatively demonstrated for one sample in the absorption measurements shown in Figure 7.3).

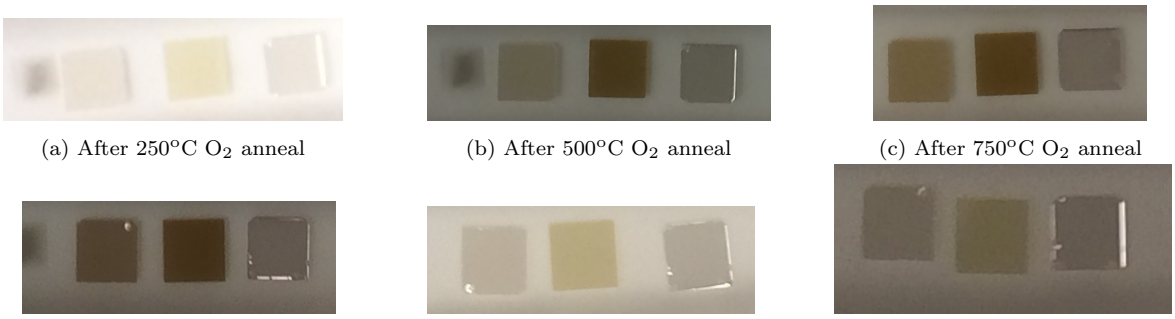

(a) After 250°C O_2 anneal (b) After 500°C O_2 anneal (c) After 750°C O_2 anneal

(d) After 1050°C O_2 anneal (e) After 250°C H_2 anneal (f) After 500°C H_2 anneal

Figure 7.6: Visual differences of STO samples due to annealing. Photographs of three samples (left to right: Sample 5, undoped from PSC; Sample 4, Fe-doped from MTI; Sample 3, undoped from MTI) after annealing at different conditions. Note that lighting conditions in the photographs were not identical.

Figure 7.6 depicts the visual effects of annealing on three samples of STO: two undoped (from different vendors), and the iron-doped sample (from left to right: Samples 5, 4, and 3). Although the photographs do not display identical lighting conditions, several qualitative differences can quickly be observed. Notably, the iron-doped sample, initially a light yellow after the 250°C O_2 anneal, quickly becomes a dark brown after the 500°C O_2 anneal; it retains this coloration, perhaps even darkening, for all subsequent oxygen anneals. The PSC sample also gradually takes on a brownish tinge after subsequent anneals, while the sample from MTI remains relatively colorless. Meanwhile, a single H_2 anneal at 250°C was sufficient

to return all samples to more-or-less their original coloration. One might expect that iron defects are responsible for the change in color of the sample from PSC, since it seems to be taking on a similar coloration to the iron-doped sample, albeit much more gradually reflecting its significantly lower dopant level; the MTI sample, meanwhile, seems to be relatively free of these defects.

This color change is similar to that observed by Wojtyniak *et al.* in their experiments with electro-coloring Fe-doped STO [33]. In that experiment, darker brown colors were associated with the more oxidized Fe^{4+} state, while the lighter yellow color indicated the presence of the Fe^{3+} state [33]. This brown color is also associated with the presence of iron defects without a conjugated oxygen vacancy, whereas the sample is expected to be transparent where iron-oxygen vacancy complexes are the dominant form of iron defect [44]. Thus, we see as might be expected the oxidation of the iron defects during oxygen annealing; the forming gas anneal, meanwhile, is sufficient to reduce these states and create iron-vacancy complexes. This indicates that our oxygen anneals were successful at removing oxygen vacancies, and that even a relatively-low-temperature anneal with H_2 is sufficient to reinstate them.

The color of the iron-doped sample was also observed to actively change as it cooled down from annealing. In the immediate aftermath of the anneal, while it was still hot, it retained a bright brick red color. This darkened as the sample cooled, until it reached the typical brown color seen in Figure 7.6.

7.7.6 Comparison with Literature Density Functional Theory Calculations

Our results showing the change in Fermi level upon annealing gives us information about the preferential charge state of iron defects when analyzed in conjunction with theoretical calculations. In this section, we will refer to the results from Baker *et al.* [44], who performed density functional theory calculations for the different charge states of iron defects in

STO, to help discuss our experimental results. These calculations tell us the most probable (lowest-energy) state of the iron defects, though there will be other states present in smaller concentrations in a given sample. Unfortunately, specific numbers are not provided for the transitions calculated in that paper, only plots; thus, our conclusions must be somewhat qualitative.

In oxygen annealing, we expect situations to be analogous to the calculations performed for oxygen-rich conditions. We note that the lowest position of the Fermi level achieved throughout the annealing experiment occurred for Samples 1 and 2, after the 750°C anneal, when their Fermi level fell to approximately 1.6 eV below the conduction band minimum. The calculations by Baker et al. indicate that this is close to the Fermi level where Fe^{3+} becomes less favorable than Fe^{4+}, making it likely that some significant fraction of defects present are undergoing this charge transition. The highest value for these samples was the initial value, 0.4 eV below the conduction band minimum, which the calculations indicate is in the regime where Fe^{3+} dominates. Thus, it is probable that some defects are undergoing a transition between Fe^{3+} and Fe^{4+} charge states for Samples 1 and 2 during the oxygen annealing steps.

Samples 3, 4, and 5 did not show such a significant change in Fermi level during experiments: the highest value attained was 0.3 eV below the conduction band minimum, and the lowest was between 0.6-0.8 eV below the conduction band minimum. The former is on the edge of the Fermi level regime where Fe^{2+} is the dominant charge state, whereas the latter is firmly in the Fe^{3+} regime. Thus, there is very plausibly a charge transition between the Fe^{2+} and Fe^{3+} states for these samples during oxygen annealing.

During reductive annealing, the vacancy defect complexes become more favorable, as may be seen in the calculations for oxygen-poor conditions. The samples measured under these anneals (2, 3, 4, and 5) displayed fairly consistent results in that the Fermi level consistently increases for each anneal. Initially, the Fermi level is at a minimum; for 3, 4, and 5, after the 250°C forming gas anneal, this minimum is approximately 0.6-0.8 eV below

the conduction band minimum – the same as after the oxygen anneal. Under reductive conditions, this would make the Fe^{3+}-V_O state the most favorable. However, the Fe^{2+}-V_O charge state becomes more favorable when the Fermi level is quite close to but still below the conduction band minimum. At the very least, Samples 4 and 5 appear to have entered this regime after the 750°C reductive anneal, being within 0.2 eV of the conduction band edge. Thus, we can safely conclude that a change in average charge state for this defect population has taken place in at least these samples.

The observed visual difference in the samples during oxygen annealing supports the assertion that the average charge state of the iron defects is indeed changing due to annealing, and that many iron defects present are no longer linked to vacancies; conversely, during reductive annealing, vacancy complexes become more favorable, as predicted. Therefore, we conclude that our anneals are successfully adjusting these parameters. Since there is no consistent change in optical gating response until the final reductive anneal, we must conclude that changes in the iron defects' charge state and vacancy conjugation have no impact on the optical gating effect. This discredits iron as the causative defect.

7.8 Effect of Red Illumination

Unlike for the ultraviolet response, the response to red showed a significant difference based on supplier, as may be seen in Figure 7.7 (a). Significantly, for samples from MTI and PSC, the illumination transiently causes a spike in contact potential analogous to ultraviolet illumination; one might infer that there is also the formation of a two-dimensional electron gas. However, this did not occur in the sample from Crystal, which had an oppositely-signed response to red light; conversely, all three had similar responses to ultraviolet illumination. In general, it was found that the red response was erratic and relatively inconsistent across samples; combined with the fact that in these experiments, the Fermi level was generally reset by a long red illumination to give consistency, which prevented the effect of the red from

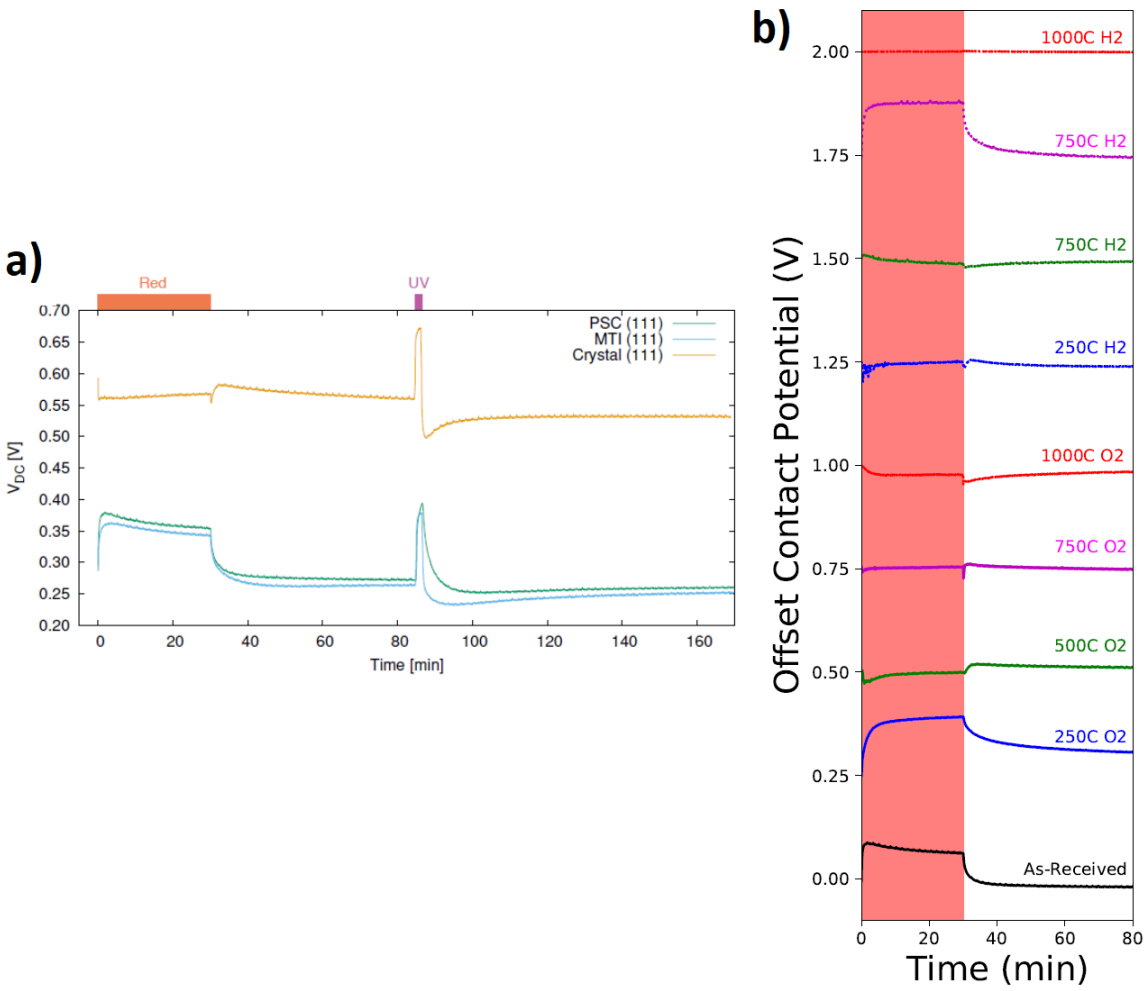

Figure 7.7: Contact potential response to red illumination. (a) Supplier comparison showing red response for samples from PSC, MTI, and Crystal. (b) Annealing comparison of red response for Sample 5 from PSC; note all results are offset by a constant and therefore are relative, not absolute.

being differentiated in a standard measurement, we chose to focus instead on the reaction to ultraviolet light.

However, for the purposes of comparison, Figure 7.7 (b) depicts how the response of Sample 5 (from PSC) to red illumination changes as a result of the different anneals performed. The positive sign of the red response is maintained for the initial 250°C anneal; higher-temperature oxygen anneals have mitigated responses, and the relation between illuminated period and the subsequent dark state varies without any clear dependence. The peak during illumination does not appear after the first two forming gas anneals; it is reinstated for the 750°C forming gas anneal, but vanishes (as all responses do) for the 1000°C

forming gas anneal. Overall, these results do not shed any real light on the effect, or show as clear of patterns as the ultraviolet responses.

7.9 Comparison of Different Crystal Orientations

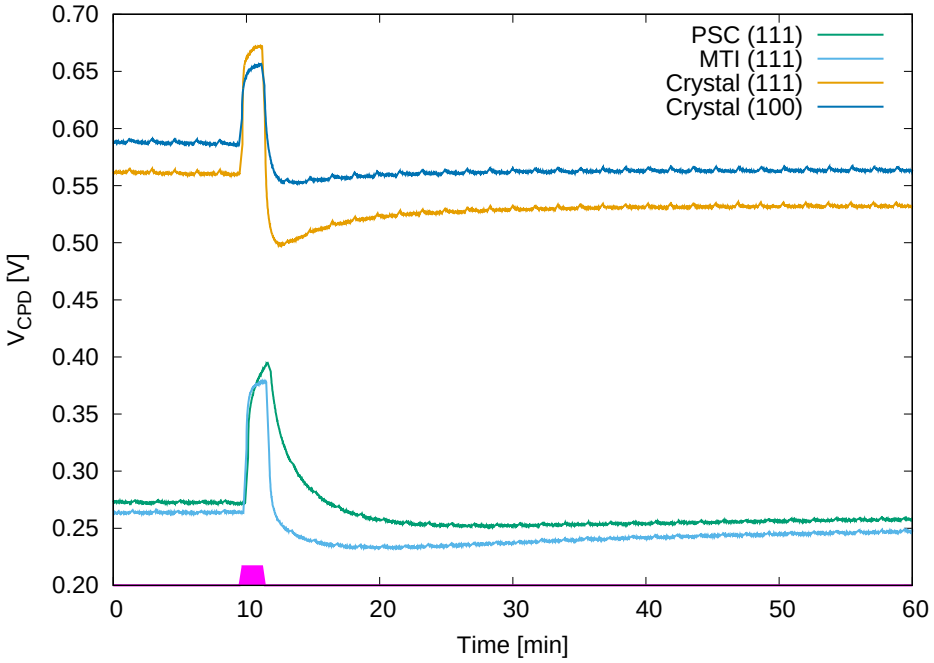

Figure 7.8: Comparison of ultraviolet response for different crystal orientation of STO. The response of two STO wafers with (111) and (100) orientations from Crystal are shown and additionally compared with (111)-oriented STO wafers from PSC and MTI.

It was possible to directly evaluate the impact of crystal orientation upon the optical gating effect to determine if the effect is directionally dependent. Both (111) and (100) STO wafers (from Crystal; also, (111)-oriented samples from MTI and PSC) were compared in a single point measurement to observe what (if any) difference was present. This data is presented in Figure 7.8. As may be easily observed, despite a slight offset in the magnitude of the contact potential across the two orientations, the resultant data have shapes that are essentially identical. Thus, it may be definitively concluded that the optical gating effect

indeed occurs in STO independently of crystal orientation, and thus is a bulk property non-dependent on specific surface termination. While there initially may appear to be some variation in the strength of some responses (i.e. the transient ultraviolet peak) according to crystal orientation, sample-to-sample variation showed differences of an equal magnitude to these differences, so we may discount the orientation as being a significant factor.

7.10 Measurements of Graphene on STO

7.10.1 Spatial Measurement of Graphene on STO

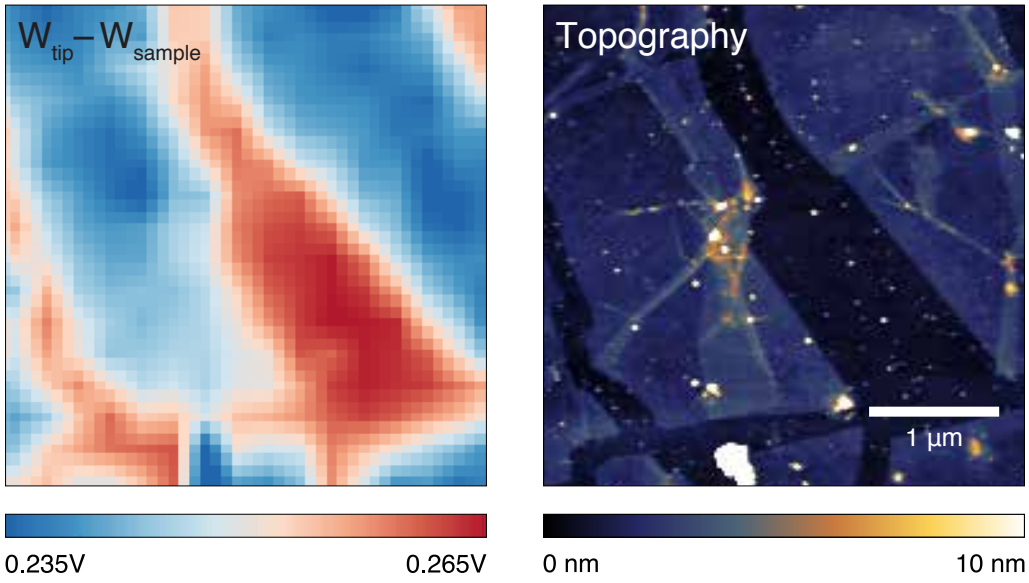

Figure 7.9: (a) KPFM image of graphene placed on STO subsequent to ultraviolet illumination. (b) Topographic image of the same area.

A layer of graphene was transferred onto a piece of STO and measured to ascertain how the contact potential differs between the two-dimensional material and the surface of the STO during optical gating. Figure 7.9 (b) depicts a topographical image of the graphene as measured by regular AFM (showing some dirt, as well as slight wrinkles in the graphene); in comparison, Figure 7.9 (a) depicts the spatially-measured contact potential, expressed as the difference between the work function of the tip and the measured surface, subsequent to

ultraviolet illumination. The STO has a noticeably distinct contact potential in comparison to the tip, while the difference on the graphene surface is smaller in magnitude. Accordingly, the two material types are easily distinguishable by work function value.

Interestingly, the work function of graphene is generally much higher in comparison to STO than this data would suggest, with literature values ranging from 4.62 eV (under a metal contact, regardless of what metal) to above 4.89 eV when exposed [117]. The difference in contact potential seen is therefore less than might be anticipated; however, graphene nonetheless has a lower contact potential, corresponding to the higher work function. It is possible that due to the thinness of the material, the observed work function via our measurement reflects a combination of work functions of graphene and STO, being significantly affected by the latter.

7.10.2 Single-Point Measurements of STO and Graphene

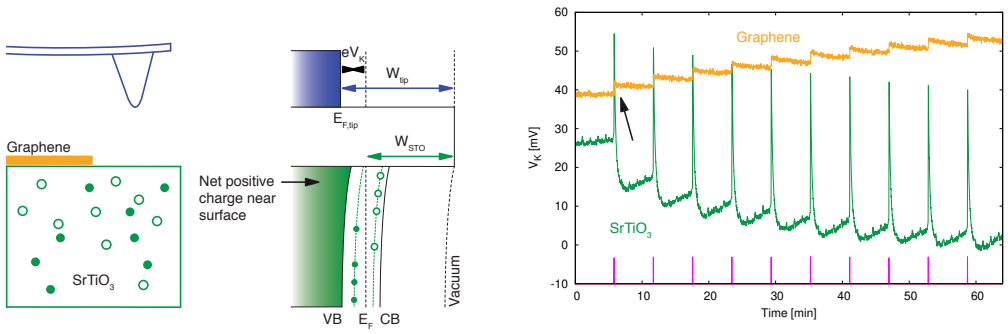

Figure 7.10: Contact potential response of graphene and STO to ultraviolet illumintion. (a) A cartoon schematic of the measurement, showing the AFM tip in proximity to the graphene on STO. (b) Cartoon depicting the band alignment of the STO and tip at equilibrium; the defects in the STO are represented by the filled and empty circles, and the sum of their distribution determines the bias V_k measured by the tip. (c) Data depicting the measured contact potential of bare STO (green) and graphene on STO (orange) when subjected to a series of 1.5 second ultraviolet pulses.

Single-point measurements were also taken both of bare STO as well as of graphene layered onto STO during a series of subsequent 1.5 second ultraviolet illuminations (see Figure 7.10 (a)). Figure 7.10 (c) plots the measured voltage for each of these situations. As usual

for untreated STO, although the potential shows a substantial increase in the transient case of illumination, after cessation of illumination, the contact potential drops significantly and remains relatively constant thereafter; with subsequent illuminations, the contact potential decreases in steps. This indicates that the surface of the STO is becoming more positive, and consequently that the Fermi level of the STO is being sequentially lowered with each illumination; presumably, the many negative defect states which are being continually re-excited near the surface of the STO during illumination are now also diffusing away into the substrate, leaving a relatively positively-charged surface.

In comparison, the measurement of graphene shows no peaks during ultraviolet illumination; instead, there is a step-by-step increase in contact potential – and by association, Fermi level – corresponding to each dose. Upon cessation of illumination, the resistance remains constant. This measurement is closely correspondent to the resistance measurements described in Chapter 6, which also demonstrated similar results. It is important to note that the changes in contact potential for the STO (after illumination ends) versus the graphene have opposite signs: on bare STO it decreases, whereas for graphene it increases. This may be in part due to transfer of the negative charge from the accumulation at the surface of the STO during illumination into the graphene, which acts as one possible diffusive outlet of the electrons, as well as due to the positively-charged surface inducing electron conductivity in the material.

7.10.3 The Effect of Red Illumination on Graphene

Some ambiguous results were obtained when measuring the response of the graphene sample to red light in the KPFM set-up. These are depicted in Figure 7.11 (a). As may be seen, when the red light is turned on, the sample's contact potential (and by extension, its Fermi level) clearly decrease from the prior value. However, while the red light is sustained, the Fermi level does not continuously decrease; instead, the value holds constant in some circumstances, while in others it shows a continuous upwards drift, albeit not returning to the initial value.

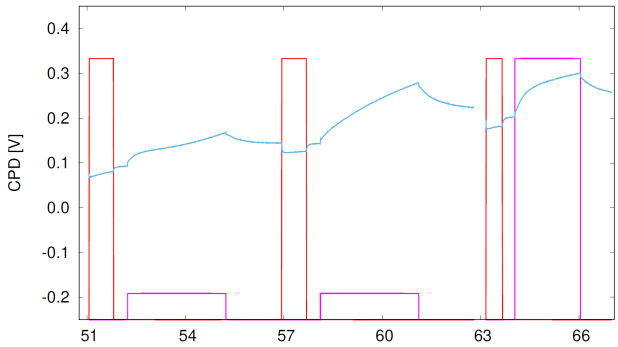

(a) Data depicting the reaction of graphene to ultraviolet and red light as a function of time, as measured via KPFM.

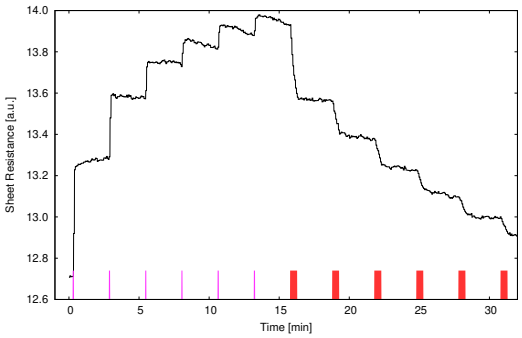

(b) Probe station measurement depicting the graphene's sheet resistance response to illumination by ultraviolet and red light.

Figure 7.11: Plots depicting the response of the graphene's contact potential to ultraviolet and red light as a function of illumination time. The vertical purple and red bars depict illumination periods; illumination power is depicted in arbitrary units.

This is puzzling because the Fermi level would be expected to continually decrease under red illumination, corresponding to the results obtained in Section 6.3.1. Cessation of red light results in an instantaneous increase in Fermi level, albeit not quite to the same level as it had previously held in the aftermath of ultraviolet illumination.

A comparative analysis of the effects of ultraviolet and red illumination on this sample was done in the probe station set-up, as may be seen in Figure 7.11 (b). Here, the sheet resistance may be seen to respond exactly as expected, with the resistance stepping upward in response to ultraviolet pulses, and correspondingly being stepped downward by red pulses. These changes in resistance would be reasonably expected to directly correspond to stepping the Fermi level up towards the Dirac point with ultraviolet illumination, and subsequently downwards again with red illumination. The resistance is presumably increased by the accumulation of electrons in the material due to potential charge transfer and the positive surface of STO; this accumulation suppresses hole-based conduction in graphene below the Dirac point, indicating that our graphene is p-type.

Although the root cause of the discrepancy between the red reaction in the two subplots of Figure 7.11 is unknown, it is possibly due to the difference in experimental set-up. The root cause of the drift visible in the KPFM measurements may be linked to the presence of the tip in proximity to the graphene, or alternatively to the effect of the bias at which the

sample is being held. Since red illumination by and large has a smaller impact on the effect than ultraviolet illumination, and since the drift is in the positive direction, these impacts may still be present but less perceptible during the ultraviolet sequences. It is important to note that the net effect of red illumination is still substantially in the negative direction, representing decrease in Fermi level, regardless of the minor subsequent drift, and that the drop in contact potential occurs immediately. Unfortunately, the exact cause of this behavior remains uncertain.

7.11 Analysis

This set of experiments provided the first known direct measurements of the optical gating effect on the surface of bare STO. This data indicates that during the application of a pulse of ultraviolet light, the surface of STO becomes temporarily much more negative, indicating that defects near the surface are being ionized to enable an increase in conductivity, and possibly corresponding to a temporary downwards bend in the conduction band of the STO and creation of a 2DEG. However, due to the relatively small penetration distance of the ultraviolet light, a net diffusion of carriers away from the surface results in a loss of negative carriers to deeper regions in the material, correspondingly leaving the equilibrium state after illumination as more positive (i.e. possessing a lower contact potential) compared to the equilibrium state prior to illumination. Thus, we see a downward stepping in the contact potential after each burst of ultraviolet light. This confirms the longstanding assertion that ultraviolet light causes the surface of STO to become positively-charged.

Figure 7.12 depicts how the bands are believed to react in response to ultraviolet light in the KPFM system. Initially, the Fermi level of the sample E_F is determined by the assortment of defects ambiently present in the sample and the bands are unbent. However, when stimulated with ultraviolet light, defects near the surface are ionized, causing a downward bending in the bands and the reduction of the material's work function. If the band bending

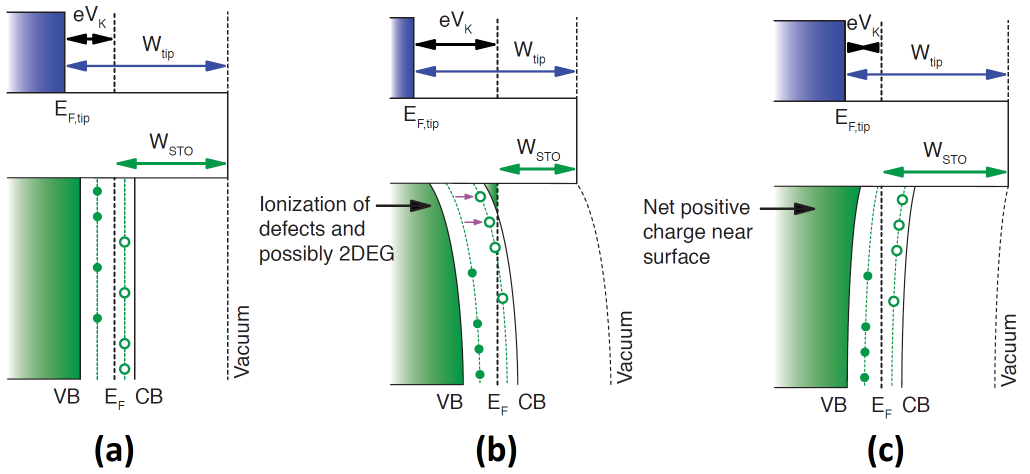

Figure 7.12: Cartoon depicting the band bending believed to take place during optical gating, as impacting the KPFM set-up. (a) shows the situation prior to illumination; (b) shows during illumination; and (c) shows after illumination. The material is depictied in green, with VB and CB indicating the valence and conduction bands respectively, and the open and full circles depicting random defects in the material. The work function and Fermi level of the tip and sample are denoted by W and E_F respectively. V_K denotes the measured bias. *Figure courtesy of Joost van Bree.*

is sufficiently deep, this could result in the accumulation of electrons at the surface in the form of a 2DEG. The migration of electrons throughout the material, meanwhile, leaves a net accumulation of positive charge at the surface, resulting in an alleviation of the downwards band bending, or possibly even upwards bending. The aftermath also leaves the work function higher than the initial state, as measured.

The annealing studies performed also demonstrate the effect of removing (with an oxygen-rich environment) and adding (with an oxygen-poor environment) oxygen vacancies into the STO. The effect of annealing is supported by the change in color of several samples, which becomes brown under oxygen anneals (indicating that more and more iron defects are oxidized and not associated with oxygen vacancies) and more transparent under forming gas anneals (indicating that the iron defects are becoming more reduced and conjugating with oxygen vacancies) [44]. The excess of oxygen vacancies, and their associated provision of electrons, provided by the H_2 annealing at 1050^{o}C is likely the cause of the free carriers seen in the absorption measurement for that treatment.

In assessing the transient part of the effect, oxygen annealing was broadly shown to

decrease the peak in contact potential that appeared under ultraviolet light for all samples, with all save the iron-doped sample actually showing a transition in peak sign from positive to negative. Such behavior suggests that the large accumulation of electrons occurring at the surface of untreated STO during illumination has been stifled, perhaps preventing or even reversing the downward band bending believed to be associated with this transient stimulus. Conversely, even a relatively low-temperature forming gas annealing reinstated this surface electron accumulation in all samples subjected to such treatment until the ultimate quenching of the effect seen in the 1000°C/1050°C anneal. This indicates that oxygen vacancies, or vacancy complexes, near the surface are very likely one of the defects being ionized by the ultraviolet light to create the strong negative surface charge seen in untreated STO during illumination.

However, oxygen annealing did not have a significant impact on the persistent part of the effect, which consistently showed a decrease in contact potential relative to the initial state after ultraviolet dosing. Since Tarun *et al.* only observed their persistent photoconductivity in reductively-annealed samples [36], we might expect oxygen annealing to suppress the persistent effect; no such result is observed. Regardless of oxygen annealing, the contact potential (and therefore Fermi level) consistently dropped in response to ultraviolet light after the dissipation of transient effects.

While iron doping was seen to impact the transient response to ultraviolet light, with the doped sample still experiencing a peak in contact potential during illumination even after annealing under oxygen at 1000°C (unlike all other sample measured), this sample also showed no substantial distinction from other samples in terms of its persistent effect, regardless of what oxidation state the iron defects were in (as was shown by absorption data and also easily visually observed, in accordance with the work of Baker *et al.* [44]); indeed, if anything, the iron-doped sample's associated data may be described as "typical". Despite the fact that annealing should alter the charge states of iron present in the STO [22], and may visually be concluded to do so, there is no clear impact of any annealing condition until

the final anneal; if a particular defect charge state was linked to the effect, one might expect the responsivity to significantly change. This all provides a strong argument that iron defect complexes are not responsible for the optical gating phenomenon. Nonetheless, the transient ultraviolet response indicates that they may still contribute to its extent, depending on the role that electron transfer from the STO to the overlying thin film material plays in the magnitude of the effect.

Finally, a high-temperature (1000°C or more) anneal under forming gas is sufficient to completely quench the effect. This is likely due to the large-scale creation of free carriers as the Fermi level enters the conduction band, an assertion supported by the fact that reduction annealing at 1100°C has been previously shown to be linked to increased carrier concentration in STO [13].

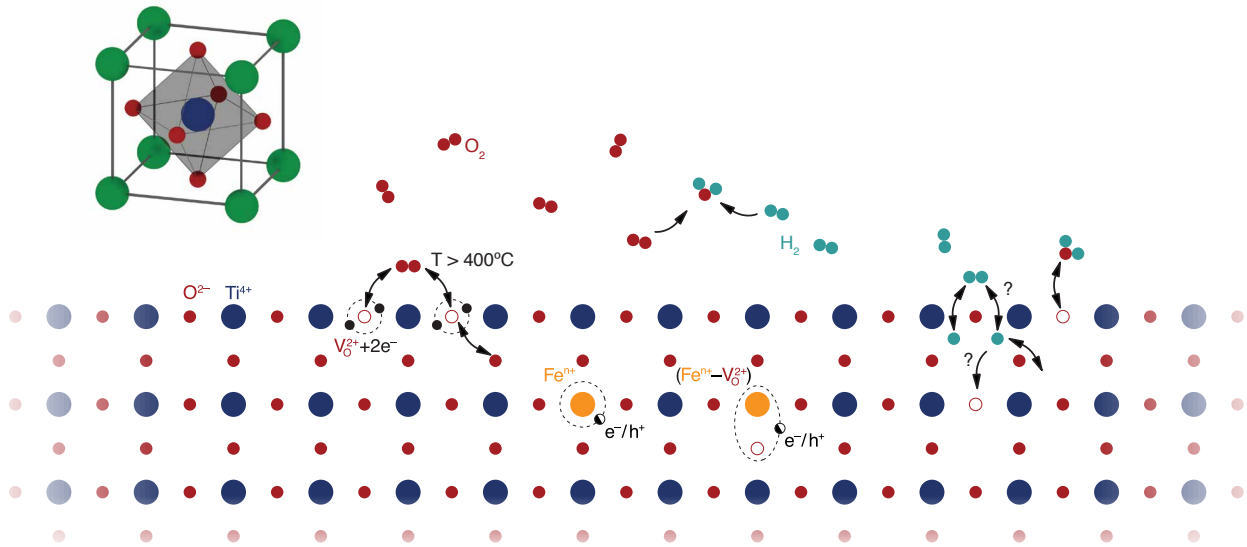

Figure 7.13: Cartoon depicting how annealing under different conditions might affect defects near the surface of STO. The regular pattern at the bottom of the image corresponds to the STO crystal lattice, while the relatively empty region above corresponds to the annealing atmosphere. Red circles represent oxygen atoms; blue circles represent titanium atoms; orange circles represent iron atoms; green circles represent hydrogen atoms; and small black/white circles represent electrons/holes. Vacancies are depicted by hollow circles; complexes are signified via an encompassing dotted line. *Figure courtesy of Joost van Bree.*

Figure 7.13 is a cartoon showing how the different annealing conditions to which the samples were subjected may have impacted the defect populations in the STO. On the left

side of the figure, the floating O_2 molecules represent their presence in an oxygen anneal, and we see how at higher temperatures, the ambient oxygens may have taken the place of oxygen vacancies near the surface of the STO, replacing them in the lattice. Here, we can see an iron defect surrounded by oxygens. Moving further right, we see how hydrogen-rich conditions during annealing may have lead to the ambient formation of water by pulling oxygen from the surface of STO, forming oxygen vacancies in the lattice. Additionally, the hypothetical formation of iron-vacancy complexes resulting from these oxygen-poor conditions is shown. Further possibilities, such as that hydrogen atoms diffused into the lattice during these annealing steps to create additional defects, are also depicted, since such defects are linked to persistent photoconductivity in STO [37]; however, the impact of these defects on this particular persistent effect is unknown.

This data further indicates that the 2.9 eV-stimulated persistent photoconductivity observed by the authors Tarun [36], McCluskey [35], and Poole [37] is unrelated to the optical gating effect. The observed persistent photoconductivity has alternately been linked to titanium vacancies [35] [36] or different hydrogen defects [37]; however, regardless of provenance, it is also ubiquitously linked to reductive annealing, and does not occur in its absence. Poole *et al.* observed that particularly annealing under water vapor, but also under H_2 atmosphere, at 1200^{o}C for an hour was associated with incurring the effect, and oxygen annealing did not stimulate it [37]. This is very different from what was observed in this dataset, where oxygen annealing only had an impact on the transient illumination part of the effect but still demonstrated the persistent aspect, and annealing under H_2 at 1050^{o}C destroyed the effect for all samples. Thus, we conclude that this persistent photoeffect has a distinctive mechanism.

This work also explicitly confirmed the longstanding assumption that the overall optical gating effect is crystal orientation-independent, being a bulk property unlinked to surface termination, as might be inferred by different crystal orientations being used in past works [1] [93].

The investigation of graphene's behavior on STO offered a more direct look at how two-dimensional materials are impacted by optical gating. These experiments gave similar results to those obtained in the measurements in the previous chapter, but provided more detailed information by providing a control measurement of the surface of the STO. The fact that the STO's contact potential transiently increases while graphene's is also increasing could indicate that as the surface of the STO transiently takes on a more negative character due to the pulses of ultraviolet light, the graphene is acting as the recipient of direct electron transfer (in addition to the net drift of carriers to deeper regions of the STO) and becoming increasingly negative as its chemical potential correspondingly increases. Regardless of whether or not direct transfer takes place, the net drift of negative carriers deeper into the bulk leaves the surface of the STO more positive, incurring electron conductivity (and stifling hole-based conduction).

The effect of red light on graphene was more ambiguously measured by the KPFM set-up. Although a dip in contact potential of graphene was measurable under red light as expected, this effect did not seem to be time-dependent and was subject to an upward drift in contact potential, opposite to what might be anticipated. This effect was confirmed not to be related to the sample itself, which behaved under a resistance measurement analogously to the sample in Section 6.3.1. Ultimately, this deviation in behavior is believed to be related to the KPFM set-up itself, but elides concrete explanation.

7.12 Calibrations and Controls

7.12.1 Tip Calibration

To ensure that the contact potential data produced would correlate directly to the work function, supporting our analysis, control measurements were made on a variety of different polycrystalline metals (Zn, Zr, Ti, W, and HOPG) and compared to tabulated values for these species found in the literature. This comparison may be found in Figure 7.14. Note

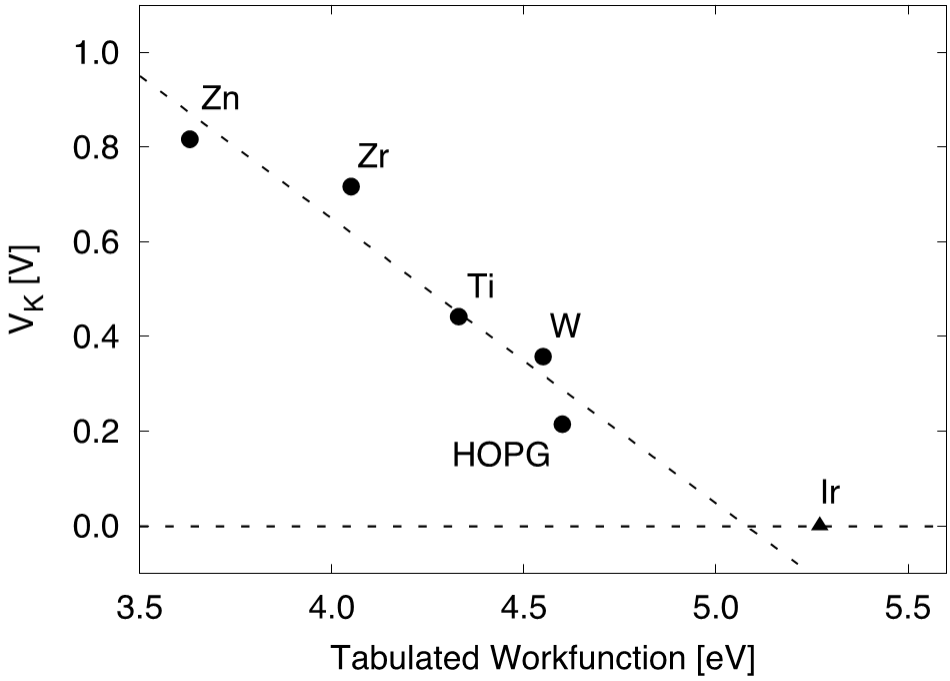

Figure 7.14: A calibration of the measured contact potentials of different metals versus their tabulated work functions.

that the point for iridium is given due to it being the composition of the tip, hence the zeroed potential. As may be seen, the two data sets have a relationship that is very close to linear, indicating a close negative correspondence between the two quantities. Thus, we may conclude that the contact potentials measured are indeed an accurate reflection of the work functions, with greater contact potential corresponding to reduced work function, and enabling us to make the appropriate conversions using the fit line.

7.12.2 Discounting Tip Interference

It is important during any measurement to ensure that the measurement apparatus itself not interfere with the data being obtained; thus, we sought to demonstrate that the conductive tip being used to conduct the KPFM measurements were not in any way affecting the results. Two factors were considered which might impact the data being obtained: the first was the distance of the charged tip from the measured surface, which might induce some related change in the substrate such as a tip-induced band bending; the second was the frequency of

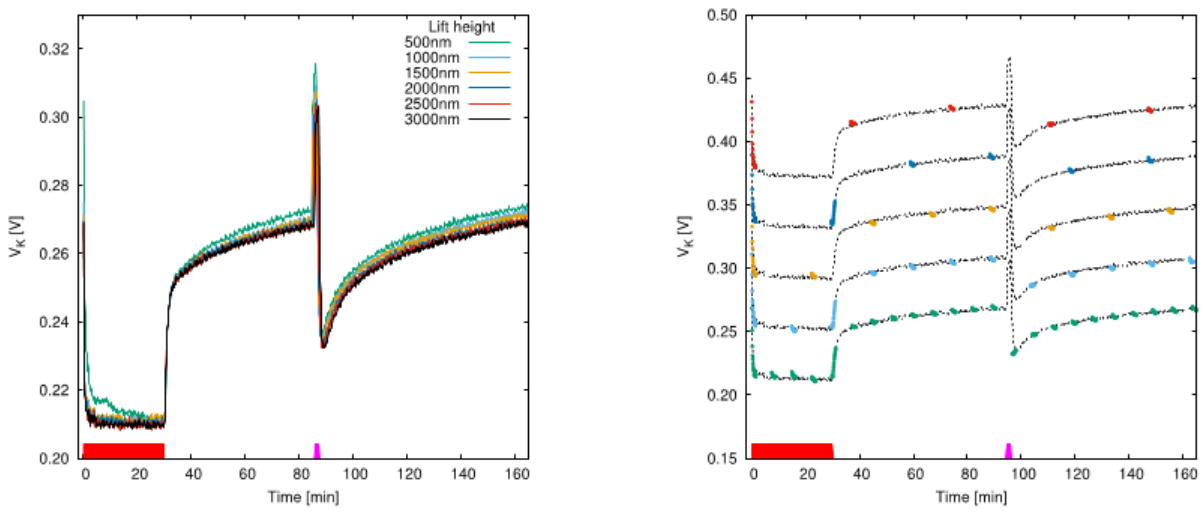

Figure 7.15: (a) Contact potential during an ultraviolet/red sequence as a function of tip liftoff height. (b) Comparison of measured contact potential for different series of measurements with different measurement frequencies (measurements are denoted by colored points). Curves offset for clarity.

the measurements taken, since between measurements the tip is subject to a certain amount of drift. Thus, these controls took the form of two distinct sets of measurements, which are depicted in Figure 7.15.

In Figure 7.15 (a), the impact of different tip distances during measurement was ascertained by performing a sequence of red illumination (30 min), followed by 60 minutes of darkness, followed by a brief (100 second) pulse of ultraviolet light, and finally allowing the measurement to continue in darkness again. The sequence used was particularly lengthy to observe any possible differences. Six different tip distances were used, separated by intervals of 500 nm: 500 nm, 1000 nm, 1500 nm, 2000 nm, 2500 nm, and 3000 nm. It may clearly be seen that all six distances result in roughly the same shape of data, identical to the expected function found in all previous measurements: a decrease in contact potential during red illumination which returns to a relatively constant value (with a period of relaxation) during darkness. Ultraviolet illumination imbues a spike in contact potential, followed by a sharp decrease in contact potential after cessation of illumination; this again relaxes, eventually approaching the pre-ultraviolet potential after many minutes. There is only a slight difference in shape observable in the minimum tip-distance measurement: a slight peak occurs

after the initiation of red illumination for only the 500 nm distance, which is not visible in any other data set. Otherwise, the data sets are nearly identical, with only very small discrepancies in that as the tip-sample distance decreases, the contact potential becomes comparatively very slightly higher. Nonetheless, these changes are not significant enough – despite the large range of distances used – to create a notable impact. Accordingly, tip distance is not a significant factor in the measurements taken.

The frequency of measurement was then evaluated as a possible source of influence. In Figure 7.15 (b), the same measurement sequence is used. A data set is used to act as a visual guide to show what a continuous measurement would show under the same conditions. Measurements taken at different frequencies are shown superimposed upon this set, with the offset data showing (from top to bottom) increasing frequency of measurement. Nonetheless, it may clearly be seen that regardless of the frequency chosen, all measurements fall neatly onto the expected curve. Accordingly, we may additionally dismiss this as a factor interfering with the KPFM measurements taken. This further rules out that the superluminescent diode used in the AFM to monitor tip deflection is playing any significant role, despite the fact that light from that source could plausibly be hitting the sample directly instead of reflecting off the cantilever, or alternately be scattered throughout the system.

7.12.3 Confirming the KPFM Mathematical Model

We performed measurements on a STO sample to confirm that the zeroth, first, and second harmonic components of the electrostatic force depend upon V_{CPD} and V_{AC} as described in Section 5.2.1. These measurements also did not indicate a notably different height dependence from the model. Thus, we conclude that the model in Section 5.2.1 is an accurate description of the measurements taken, confirming that the recorded DC bias measures the work function difference between the tip and STO.

Because the capacitance is dependent on the distance between tip and sample, the force correspondingly depends on height. Accordingly, the distance was maintained at a constant

value of 1 μm. This relatively large distance ensure consistency between measurements, as well as reducing the impacts of surface topography and geometric differences between tips. However, this greater distance also meant a sacrifice of some lateral resolution. Since most measurements were recorded at a single point on the sample surface, with a duration significantly longer than the thermal drift stability of the system, the AFM was programmed to periodically automatically approach the surface and then retract by a set distance between measurements.

Chapter 8

Conclusions

This work has served to further illuminate several aspects of the unique optical gating effect which is produced by STO when subjected to different wavelengths of light.

The first part of this work has contributed to a better understanding of how the optical gating effect impacts different materials by adding two significant categories of material - graphene and transition metal dichalcogenides - to those whose behavior under optical gating has been observed. In graphene, we saw that optical gating was directly equivalent to electrical gating, with behavior exactly corresponding to the expected performance for a material with a Dirac cone band structure: the Fermi level could be shifted up and down through the Dirac point by ultraviolet and red light, respectively. In MoS_2, optical gating enabled the creation of a switch with two ON states - during ultraviolet illumination, with an ON/OFF ratio exceeding 10^5, and after ultraviolet illumination, with an ON/OFF ratio of roughly 10^2. The magnitude of this former illuminated ON state is due to a transient photocurrent created by the illumination. The persistence of the latter ON state was further characterized over sixteen hours, with a fit showing a multiple-day lifetime, and its rapid quenching via the application of red light was demonstrated, confirming that the phenomenon is created by the STO substrate. Higher power densities of ultraviolet light seem to result in a faster decay of the persistent state. Optical gating was seen to be additive to electrical gating while the

material was in the persistent ON state, an effect erased by electrically gating the material into its OFF state. Furthermore, the effects of optical gating on the current in MoS_2 proved persistent through an increase in temperature up to ambient conditions, indicating that the effect when initiated at low temperatures persists to some extent up to room temperature. Changes in behavior during temperature sweeps at around 40-50 K indicate that the quantum paraelectric phase transition in that temperature regime has a negative impact on the persistent effects in the aftermath of ultraviolet illumination. However, the optical gating effect itself is not dependent on STO's phase, having been observed taking place both above and below this transition point, as well as above and below the structural phase transition point at 105 K.

We may now provide the following broad description of how different materials behave under optical gating based on our results in conjunction with the results in the literature and the corresponding authors' discussion:

- As initially demonstrated in Reference [1] and further demonstrated in this work, materials possessing a Dirac cone band structure may have their resistance continually tuned through the Dirac point and back via optical gating, showing a resulting characteristic resistance curve where the resistance steadily increases under ultraviolet illumination until the Dirac point is reached, whereupon the resistance continually falls as the Fermi level rises. In absence of illumination, these attained resistances are fairly constant (with some relaxation). The Fermi level may then be brought down below the Dirac point again via red illumination, with an analogous behavior to the increase.

- As preliminarily demonstrated in References [1] and [92], and more expansively demonstrated in this work, n-type materials experience an increase in current when subjected to ultraviolet illumination, corresponding to the increase of their Fermi level, and resulting in the creation of a switch. Some materials may furthermore experience an additional transient photocurrent amplification during the ultraviolet illumination (i.e. MoS_2), or alternately during red illumination (i.e. ZnO). Red light correspondingly de-

creases the Fermi level of the material, resulting in a dwindling and eventual cessation of current. Sensitive bidirectional control of the conductivity of an n-type material via pulses of ultraviolet and red light has been demonstrated for the first time in this work.

- As demonstrated and discussed in Reference [92], p-type materials respond oppositely to n-type materials under the two types of illumination as a direct result of their current being based on the motion of holes: lowering the Fermi level of the material under red light results in enhanced hole conduction, while raising its Fermi level under ultraviolet light quenches it. The strength of the ultraviolet response found in that work indicates that further experiments with lower power density ultraviolet light are necessary to demonstrate tunable bidirectional control in p-type materials, but the work in this thesis has given reason to believe that such control is possible.

- Parameters that may be controlled via the Fermi level, such as superconductivity in FeSe/STO as shown in Reference [93], or the coercive field in a topological insulator as shown in Reference [95], are non-invasively controllable in a way directly analogous to electrical gating via this technique.

These observations should prove useful to any researchers who might further seek to harness the optical gating technique for manipulating similar two-dimensional systems.

The fact that these observed changes correspond to an increase (under ultraviolet) and decrease (under red) in Fermi level of the two-dimensional material was supported by KPFM measurements on graphene on top of STO, during and after illumination. Correspondingly, ultraviolet light was shown to decrease the Fermi level of the STO in the aftermath of illumination. The surface of STO was also demonstrated to become transiently extremely negatively charged during ultraviolet illumination, which we believe to be due to the bending of the conduction band near the surface possibly leading to the formation of a 2DEG during stimulation. This potential 2DEG formation was seemingly prevented by oxygen annealing,

indicating a strong link to oxygen vacancies near the surface of STO as responsible for its creation. In the aftermath of ultraviolet illumination (and the dissipation of the accumulated negative charge), the surface of STO was left more positive with a decreased Fermi level, in keeping with the expectation that electrons excited by the light had diffused further into the bulk, leaving a depletion region at the surface with relatively positive charge. In the presence of a two-dimensional material on top, electron transfer may also occur during illumination, helping to increase that material's Fermi level.

Although this work was unable to conclusively identify the defect responsible for creating the optical gating effect, the data obtained during the KPFM measurements points away from iron-based defect complexes (such as Fe^{3+}-V_O) as likely causes of the optical gating effect. First, the contact potential before and after illumination at a series of annealing conditions does not seem to be affected by whether or not iron doping is present, indicating that additional iron defects do not play a role in the altering of the Fermi level that occurs during optical gating. Additionally, the iron defects may be put into different oxidation states without the effect's cessation. The only difference that additional iron doping seems to play is in the transient photoeffect on the contact potential of illumination - consistent with the defects' responsivity to that wavelength, and reminiscent of the response shown for Fe^{3+}-V_O by Zvanut *et al.* [22] - so it remains possible that iron defects could alter the extent of conductivity change in some two-dimensional materials during ultraviolet illumination by increasing surface electron transfer. However, undoped samples displayed similar transient behavior during ultraviolet illumination prior to being subjected to oxygen annealing, or following subjection to reductive annealing steps. Thus, it seems unlikely that iron-related defects play any important role in causing this effect overall.

Furthermore, this work has provided strong evidence that the optical gating effect is unrelated to the 2.9 eV-stimulated persistent photoconductivity in STO that has been observed by several authors [35] [36] [37]. The reductive annealing at higher temperatures associated with assisting the onset of that effect has been shown in all samples tested to

destroy the optical gating effect. Additionally, while oxygen annealed samples in those works did not show persistent photoconductivity [37], oxygen annealing did not have any effect on the persistent aspect of the optical gating effect. Thus, we conclude that the two effects are unrelated.

Chapter 9

Ideas for Future Work

Unfortunately, a graduate career is not long enough to complete every possible experiment one might wish to. Thus, I will use this section to discuss several projects relating to optical gating on which I was unable to embark during my time as a PhD candidate. I hope that these ideas may help inspire other scientists who may pick up this work in the future.

9.1 All-Optical Control of the T_c of FeSe/STO

This project idea may seem somewhat familiar; after all, one of the papers [93] I have discussed in the optical gating literature review in Section 5.1.3 is devoted to the manipulation of the superconducting T_c of FeSe/STO via ultraviolet light. However, this paper was seemingly unaware that the phenomenon being observed was related to this previously-discovered effect. As a result, while they demonstrated excellent scientific work, they omitted some key experiments which I would propose be performed on FeSe/STO, and also left open the door to other interesting manipulations of their discovery.

First and most importantly, the reversibility of the effect of ultraviolet light on superconductivity through the use of red light remains to be demonstrated. Based on other optical gating work that has showed how red light reverses the effect of the initial ultraviolet illumination, it seems highly likely that this experiment will proceed exactly as expected: while

ultraviolet light lowers T_c, red light will correspondingly return it to its initial value. Thus, an initial experiment would demonstrate all-optical control of T_c by taking measurements using a pulse sequence of ultraviolet and red light: demonstrating a lack of superconductivity at a given temperature, followed by superconductivity onset due to the ultraviolet illumination; showing again that this superconductivity persists in the dark; and then showing that it is turned off by red illumination, and does not recur in subsequent darkness. Repeating these experiments at a range of ambient temperatures will demonstrate the flexible range of T_c as moderated by the optical gating effect.

Spatially-localized experiments will provide further demonstration of the usefulness of this technique in controlling the T_c of FeSe/STO. Although the set-up this work used for cryogenic measurements does not allow for localized illumination, using another set-up with focused ultraviolet and red light would enable the illumination of specific areas of material. Placing several small, contacted strips of FeSe on a STO substrate in a cryostat held at a temperature slightly above T_c would enable first the blanket red illumination of the entire area. Then, ultraviolet illumination could be used on only one such strip to raise its T_c above the ambient temperature, allowing the onset of superconductivity for only that strip, enabling a demonstration of the localizability of this change and opening the door to the direct writing of superconducting circuits via light.

9.2 Looking for Other Substrates

Although up until this point, the optical gating effect has never been observed on any substrate other than STO, it seems improbable that no other material displays this same behavior. I think that it is incredibly likely that other such materials exist, and perhaps that such materials might prove even more useful for certain experiments. The predominant question remains, however: what materials could possibly demonstrate this behavior - how do we narrow down the vast number of materials extant to the very small number which can

display this special effect?

At least to start with, we should expect that the defect responsible in STO for creating the optical gating effect will be the same. It will be simplest to begin our search in the perovskite class of materials. Obviously, identification of the exact defect responsible for this effect will also help to narrow down candidate materials which host this defect, which may lay outside the perovskite class. Thus, this effort would be inextricably linked to the effort to find the culprit defect. Upon its identification, a list of other materials who are known to form the same defect could easily be compiled and ascertained.

Of course, identifying the relevant defect could go hand-in-hand with trying out a series of other substrates, using educated guesses as a basis, which might reciprocally help to shed light on the defect responsible. Perhaps the most important consideration when looking at any potential new substrate is the band gap of that material. In STO, the fact that the relevant band gap lies in the near-ultraviolet gives us a convenient range of wavelengths in working with the optical gating effect: ultraviolet turns it on, and red turns it off. We need to have a band gap of energy above the activation energy of the responsible defect, to ensure that recombination and diffusion throughout the material is possible; however, too high a band gap would make the initiation of the optical gating effect less useful, as the required wavelength may be more likely to induce effects in the two-dimensional material on its own. Thus, to begin with, a search of materials whose band gaps lie between the near-ultraviolet and near-infrared ranges would be optimal.

Another factor that may be relevant is the dielectric constant of the material, since the large value of STO's dielectric constant has been hypothesized to be related to the effect [1]. Accordingly, a search for high-dielectric perovskites with visible band gaps may reveal a new candidate substrate for this phenomenon. However, this must be balanced with trying lower dielectric materials as well, to determine if the dielectric constant is indeed relevant to the effect.

One possibility is investigating such structurally similar materials as $BaTiO_3$ ("BTO"),

which merely replaces strontium atoms with barium. BTO possesses a bulk band gap of approximately 3.2 eV [118], which puts it in the desirable optical range. The dielectric constant is also of order 10^4 at room temperature [119]. Furthermore, BTO has been predicted to display the same persistent photoconductivity at 2.9 eV as STO [41]; while we have argued that this photoconductivity is unrelated to the optical gating effect, since BTO may also display some of the other opto-electronic responses of STO, it might display the same physics as STO in this case as well.

One other initial possibility I would put forward for future consideration is that of lead zirconate titanate, $Pb(Zr_{1-x}Ti_x)O_3$ (generally shortened to PZT). PZT is a well-characterized material which may be produced in the perovskite phase [120]. Changes in annealing temperature during preparation [121] [122] as well as in composition [123] have provided a variety of band gap values as recorded in the literature, with many values observed lying in the range between 2.1 eV to 3.8 eV - thus offering a visible- to ultraviolet-band gap, as desired. Furthermore, it possesses an extremely high room-temperature dielectric constant of around 1,900 [124].

One plausible downside to this material is that it is piezoelectric with a relatively high Curie temperature [124]. Thus, the induction of an electric field in the sample as would be caused by optical gating will result in a change in its physical dimensions, possibly stretching any two-dimensional material placed upon it. However, this may not entirely be a negative: strain has been observed to impact the electronic properties of many two-dimensional materials [125], and the conjunction of strain engineering and optical gating could perhaps be utilized for novel applications.

9.3 Gating van der Waals Heterostructures

Until now, work on optical gating has been entirely focused on layers of single materials placed upon STO. While this set of materials offers a rich array of possibilities, examination

of multiply-layered materials could also provide many venues for future research. It is of course impossible to discuss all the potential systems which could be explored, so I will limit my discussion to a few interesting examples.

One example of simple heterostructures are multiple layers of graphene. Unlike the monolayer, bilayer graphene displays a very different, parabolic band structure; furthermore, its band gap may actually be widely tuned using electrical gating, with a band gap up to 250 meV having been engineered (though this high value was only achievable with a voltage of 100 V) [126]. Using this system in conjunction with optical gating would enable some light-controlled tuning of the material's band gap in conjunction with electrical gating. Additionally, trilayer graphene with Bernal stacking order is notably distinct from the monolayer and bilayer in that it is a semimetal, with partially overlapping conduction and valence bands; the extent of this overlap has been shown to be gating dependent [127] [128], and could thus also be controllable with this technique.

Work studying heterostructures composed of single- and bilayer phosphorene stacked on graphene found that the relative positions of the two materials' band structures was gate-tunable, allowing researchers to control the Schottky barrier height and type, to the extent that the bilayer phosphorene could be made into an ohmic contact [129]. Electron transfer from the phosphorene to graphene could furthermore be achieved with small electric fields, p-doping the phosphorene [129]. While merely achieving these results with electrical gating offers significant possibilities for future heterostructure devices, it is highly likely that these modifications could be identically achieved with optical gating, enabling light-driven modification of these material properties.

van der Waals heterostructures can also show interesting spintronic properties which may be controlled via gating, as in the case of a graphene/MoS_2 heterostructure which was shown to have gate-controllable spin current and lifetime at room temperature [130]. In the aforementioned experiment, a strip of MoS_2 was placed on top of a strip of graphene to form the heterostructure on a SiO_2/Si substrate. Since the substrate did not play a significant

role in the experiment, substitution of a STO substrate could potentially enable entirely-optical control of these spin parameters. Additionally, the data showed a significant amount of variation in the spin parameters at relatively low gate voltages, which further suggests that optical gating could be a viable replacement for electrical gating in manipulating similar systems [130].

References

[1] A L Yeats, Y Pan, A Richardella, P J Mintun, N Samarth, and D D Awschalom. Persistent optical gating of a topological insulator. *Science Advances*, 1(9):e1500640, Oct 2015.

[2] William D Callister and David G Rethwisch. *Materials Science and Engineering: An Introduction (10th Ed.)*. John Wiley and Sons Inc, 2018.

[3] H Seo, A L Falk, P V Klimov, K C Miao, G Galli, and D D Awschalom. Quantum decoherence dynamics of divacancy spins in silicon carbide. *Nature Communications*, 7(12935), 2016.

[4] G D Fuchs, G Burkard, P V Klimov, and D D Awschalom. A quantum memory intrinsic to single nitrogen-vacancy centres in diamond. *Nature Physics*, 7:789–793, 2011.

[5] Ben G Streetman and Sanjay Kumar Banerjee. *Solid State Electronic Devices (7th Edition)*. John Wiley and Sons Inc, 2015.

[6] Charles Kittel. *Introduction to Solid State Physics (8th Ed.)*. John Wiley and Sons Inc, 2005.

[7] J Wang, S Deng, Z Liu, and Z Liu. The rare two-dimensional materials with Dirac cones. *National Science Review*, 2(1):22–39, March 2015.

[8] A Kahn. Fermi level, work function and vacuum level. *Materials Horizons*, 3:7–10, 2016.

[9] S Stemmer and S J Allen. Two-Dimensional Electron Gases at Complex Oxide Interfaces. *Annual Review of Materials Research*, 44:151–171, 2014.

[10] K van Benthem, C Elasser, and R H French. Bulk electronic structure of $SrTiO_3$: Experiment and Theory. *Journal of Applied Physics*, 90(12), Dec 2001.

[11] D J Kok, K Irmscher, M Naumann, C Guguschev, Z Galazka, and R Uecker. Temperature-dependent optical absorption of $SrTiO_3$. *physica status solidi (a)*, 212(9):1880–1887, 2015.

[12] H E Weaver. Dielectric Properties of Single Crystals of $SrTiO_3$ at Low Temperatures. *J. Phys. Chem. Solids*, 11:274–277, 1959.

[13] A Spinelli, M A Torija, C Liu, C Jan, and C Leighton. Electronic transport in doped $SrTiO_3$: Conduction mechanisms and potential applications. *Physical Review B*, 81(155110), Apr 2010.

[14] T Sakudo and H Unoki. Dielectric Properties of $SrTiO_3$ at Low Temperatures. *Physical Review Letters*, 26(14):851–853, Apr 1971.

[15] Alastair George Hartley Smith. *Structural and Defect Properties of Strontium Titanate*. PhD thesis, University College London, 2011.

[16] K Szot, W Speier, G Bihlmayer, and R Waser. Switching the electrical resistance of individual dislocations in single-crystalline $SrTiO_3$. *Nature Materials*, 5:312–320, Mar 2006.

[17] J F Schooley, W R Hosler, and M L Cohen. Superconductivity in Semiconducting $SrTiO_3$. *Physical Review Letters*, 12(17):474–475, Apr 1964.

[18] C S Kooonce, M L Cohen, J F Schooley, W R Hosler, and E R Pfeiffer. Superconducting Transition Temperatures of Semiconducting $SrTiO_3$. *Physical Review*, 163:380–390, Nov 1967.

[19] M N Gastiasoro, J Ruhman, and R M Fernandes. Superconductivity in dilute $SrTiO_3$: A review. *Annals of Physics*, 417(168107), Jun 2020.

[20] T Ruste, E J Samuelsen, K Otnes, and J Feder. Critical behaviour of $SrTiO_3$ near the 105^oK phase transition. *Solid State Communications*, 9(17):1455–1458, 1971.

[21] S A Hayward and E K H Salje. Cubic-Tetragonal Phase Transition in $SrTiO_3$ Revisited: Landau Theory and Transition Mechanism. *Phase Transitions*, 68(3):501–522, 1999.

[22] M E Zvanut, S Jeddy, E Towett, G M Janowski, C Brooks, and D Schlom. An annealing study of an oxygen vacancy related defect in $SrTiO_3$ substrates. *Journal of Applied Physics*, 104(064122), Sep 2008.

[23] M I Marques, C Arago, and J A Gonzalo. Quantum paraelectric behavior of $SrTiO_3$: Relevance of the structural phase transition temperature. *Physical Review B*, 72(092103), Sep 2005.

[24] J F Scott and H Ledbetter. Interpretation of elastic anomalies in $SrTiO_3$ at 37 K. *Z Phys B*, 104:635–639, 1997.

[25] L F Zagonel, M Baurer, A Bailly, O Renault, M Hoffman, S-J Shih, D Cockayne, and N Barrett. Orientation dependent work function of *in situ* annealed strontium titanate. *Journal of Physics: Condensed Matter*, 21(314013), 2009.

[26] D Wrana, K Cieslik, W Belza, C Rodenbucher, K Szot, and F Krok. Kelvin probe force microscopy work function characterization of transition metal oxide crystals under ongoing reduction and oxidation. *Beilstein J Nanotechnol.*, 10:1596–1607, Aug 2019.

[27] V E Henrich, G Dresselhaus, and H J Zeiger. Surface defects and the electronic structure of $SrTiO_3$ surfaces. *Physical Review B*, 17(4908), Jun 1978.

[28] G W Dietz and W Antpohler. Electrode influence on charge transport through $SrTiO_3$ thin films. *Journal of Applied Physics*, 78(6113), 1995.

[29] M S J Marshall, A E Becerra-Toledo, L D Marks, and M R Castell. Defects on strontium titanate. In J Jupille and G Thornton, editors, *Defects at Oxide Surfaces*, chapter 11, pages 327–349. Springer, 2015.

[30] A Janotti, J B Varley, M Choi, and C G Van de Walle. Vacancies and small polarons in $SrTiO_3$. *Physical Review B*, 90(085202), Aug 2014.

[31] A Ohtomo and H Y Hwang. Growth mode control of the free carrier density in $SrTiO_{3-\delta}$ films. *Journal of Applied Physics*, 102(083704), Oct 2007.

[32] Y Kozuka, M Kim, C Bell, B G Kim, Y Hikita, and H Y Hwang. Two-dimensional normal-state quantum oscillations in a superconducting heterostructure. *Nature*, 462:487–490, Nov 2009.

[33] M Wojtyniak, K Szot, R Wrzalik, C Rodenbucher, G Roth, and R Waser. Electrodegradation and resistive switching of Fe-doped $SrTiO_3$ single crystal. *Journal of Applied Physics*, 113(083713), 2013.

[34] J Dashdorj, M E Zvanut, and L J Stanley. Iron-related defect levels in $SrTiO_3$ measured by photoelectron paramagnetic resonance spectroscopy. *Journal of Applied Physics*, 107(083513), Apr 2010.

[35] M D McCluskey and M C Tarun. Defects and persistent conductivity in $SrTiO_3$. *AIP Conference Proceedings*, 1583(319), 2014.

[36] M C Tarun, F A Selim, and M D McCluskey. Persistent Photoconductivity in Strontium Titanate. *Physical Review Letters*, 111(187403), Oct 2013.

[37] V M Poole, J Huso, and M D McCluskey. The role of hydrogen and oxygen in the persistent photoconductivity of strontium titanate. *Journal of Applied Physics*, 123(161545), 2018.

[38] C Itoh, M Sasabe, H Kida, and K Kan'no. Electric field-induced retardation of the drift mobility of the photocarriers in $SrTiO_3$ crystal. *Journal of Luminescence*, 112:263–266, Apr 2005.

[39] Y Kozuka, Y Hikita, T Susaki, and H Y Hwang. Optically tuned dimensionality crossover in photocarrier-doped $SrTiO_3$: Onset of weak localization. *Physical Review B*, 76(085129), Aug 2007.

[40] H Zhang, L Yan, and H-U Habermeier. Unusual ultraviolet photoconductivity in single crystalline $SrTiO_3$. *Journal of Condensed Matter Physics*, 25(3):035802, 2013.

[41] Z Zhang and A Janotti. Cause of Extremely Long-Lasting Room-Temperature Persistent Photoconductivity in $SrTiO_3$ and Related Materials. *Phys. Rev. Lett.*, 125(126404), 2020.

[42] W Meevasana, P D C King, R H He, S-K Mo, M Hashimoto, A Tamai, P Songsiriritthigul, F Baumberger, and Z-X Shen. Creation and control of a two-dimensional electron liquid at the bare $SrTiO_3$ surface. *Nature Materials*, 10:114–118, Jan 2011.

[43] W D Rice, P Ambwani, M Bombeck, J D Thompson, G Haugstad, C Leighton, and S A Crooker. Persistent optically induced magnetism in oxygen-deficient strontium titanate. *Nature Materials*, 13:481–487, 2014.

[44] J N Baker, P C Bowes, D M Long, A Moballegh, J S Harris, E C Dickey, and D L Irving. Defect mechanisms of coloration in Fe-doped $SrTiO_3$ from first principles. *Applied Physics Letters*, 110(122903), 2017.

[45] P Ajayan, P Kim, and K Banerjee. Two-dimensional van der Waals materials. *Physics Today*, 69(9):38–44, 2016.

[46] X Xi, Z Wang, W Zhao, J-H Park, K T Law, H Berger, L Forro, J Shan, and K F Mak. Ising pairing in superconducting $NbSe_2$ atomic layers. *Nature Physics*, 12:139–143, 2016.

[47] C Cui, F Xue, W-J Hu, and L-J Li. Two-dimensional materials with piezoelectric and ferroelectric functionalities. *npj 2D Materials and Applications*, 2(18), 2018.

[48] S Das, W Zhang, M Demarteau, A Hoffman, M Dubey, and A Roelofs. Tunable Transport Gap in Phosphorene. *Nano Letters*, 14(10):5733–5739, Aug 2014.

[49] J Qiao, X Kong, Z Hu, F Yang, and W Ji. High-mobility transport anisotropy and linear dichroism in few-layer black phosphorus. *Nature Communications*, 5(4475), 2014.

[50] X Duan, C Wang, A Pan, R Yu, and X Duan. Two-dimensional transition metal dichalcogenides as atomically thin semiconductors: opportunities and challenges. *Chemical Society Reviews*, 44(24):8859–8876, Oct 2015.

[51] K S Novoselov, A Mischenko, A Carvalho, and A H Castro Neto. 2D materials and van der Waals heterostructures. *Science*, 353(6298), Jul 2016.

[52] K Kang, S Xie, L Huang, Y Han, P Y Huang, K F Mak, C-J Kim, D Muller, and J Park. High-mobility three-atom-thick semiconducting films with wafer-scale homogeneity. *Nature*, 520:656–660, Apr 2015.

[53] A K Geim and I V Grigorieva. Van der Waals heterostructures. *Nature*, 499:419–425, 2013.

[54] Y Cao, V Fatemi, S Fang, K Watanabe, T Taniguchi, E Kaxiras, and P Jarillo-Herrero. Unconventional superconductivity in magic-angle graphene superlattices. *Nature*, 556:43–50, 2018.

[55] K S Novoselov, A K Geim, S Morozov, D Jiang, Y Zhang, S V Dubonos, I V Grigorieva, and A A Firsov. Electric Field Effect in Atomically Thin Carbon Films. *Science*, 306(5696):666–669, Oct 2004.

[56] M J Allen, V C Tung, and R B Kaner. Honeycomb Carbon: A Review of Graphene. *Chemical Reviews*, 110(1):132–145, Jul 2009.

[57] A Zurutuza. Graphene and Graphite - How Do They Compare? Published online at https://www.graphenea.com/pages/graphene-graphite ; accessed: 2021-08-04.

[58] S Wakeland, R Martinez, J K Grey, and C C Luhrs. Production of graphene from graphite oxide using urea as expansion-reduction agent. *Carbon*, 48(12):3463–3470, Oct 2010.

[59] L Jiao, L Zhang, L Ding, J Liu, and H Dai. Aligned graphene nanoribbons and crossbars from unzipped carbon nanotubes. *Nano Research*, 3:387–394, Apr 2010.

[60] P-Y Teng, C-C Lu, K Akiyama-Hasegawa, Y-C Lin, C-H Yeh, K Suenaga, and P-W Chiu. Remote Catalyzation for Direct Formation of Graphene Layers on Oxides. *Nano Letters*, 12(3):1379–1384, Feb 2012.

[61] A Ismach, C Druzgalski, S Penwell, A Schwartzberg, M Zheng, A Javey, J Bokor, and Y Zhang. Direct Chemical Vapor Deposition of Graphene on Dielectric Surfaces. *Nano Letters*, 10(5):1542–1548, Apr 2010.

[62] J Sun, Y Chen, M K Priydarshi, Z Chen, A Bachmatiuk, Z Zou, Z Chen, X Song, Y Gao, M H Rummeli, Y Zhang, and Z Liu. Direct Chemical Vapor Deposition-Derived Graphene Glasses Targeting Wide Ranged Applications. *Nano Letters*, 15(9):5846–5854, Aug 2015.

[63] Q-Q Zhuo, Q Wang, Y-P Zhang, D Zhang, Q-L Li, C-H Gao, Y-Q Sun, L Ding, Q-J

Sun, S-D Wang, J Zhong, X-H Sun, and S-T Lee. Transfer-Free Synthesis of Doped and Patterned Graphene Films. *ACS Nano*, 9(1):594–601, Dec 2014.

[64] M A Fanton, J A Robinson, C Puls, Y Liu, M J Hollander, B E Weiland, M LaBella, K Trumbull, R Kasarda, C Howsare, J Stitt, and D W Snyder. Characterization of Graphene Films and Transistors Grown on Sapphire by Metal-Free Chemical Vapor Deposition. *ACS Nano*, 5(10):8062–8069, Sep 2011.

[65] J Sun, T Gao, X Song, Y Zhao, Y Lin, H Wang, D Ma, Y Chen, W Xiang, J Wang, Y Zhang, and Z Liu. Direct Growth of High-Quality Graphene on High-κDielectric SrTiO3 Substrates. *Journal of the American Chemical Society*, 136(18):6574–6577, Apr 2014.

[66] M I Katnelson, K S Novoselov, and A K Geim. Chiral tunneling and the Klein paradox in graphene. *Nature Physics*, 2:620–625, 2006.

[67] K Bolotin, K J Sikes, Z Jiang, M Klima, G Fudenberg, J Hone, P Kim, and H L Stormer. Ultrahigh Electron Mobility in Suspended Graphene. *Solid State Communications*, 146(9-10):351–355, Feb 2008.

[68] G Yang, L Li, W B Lee, and M C Ng. Structure of graphene and its disorders: a review. *Science and Technology of Advanced Materials*, 19(1), Aug 2018.

[69] K F Mak, K L McGill, J Park, and P L McEuen. The valley Hall effect in MoS_2 transistors. *Science*, 344(6191):1489–1492, Jun 2014.

[70] J R Schaibley, H Yu, G Clark, P Rivera, J S Ross, K L Seyler, W Yao, and X Xu. Valleytronics in 2D materials. *Nature Reviews Materials*, 1(16055), Aug 2016.

[71] D Gupta, V Chauhan, and R Kumar. A comprehensive review on synthesis and applications of molybdenum disulfide (MoS_2) material: Past and recent developments. *Inorganic Chemistry Communications*, 121(108200), Nov 2020.

[72] B Radisavljevic, A Radenovic, J Brivio, V Giacometti, and A Kis. Single Layer MoS_2 Transistors. *Nature Nanotechnology*, 6:147–150, 2011.

[73] Y P Venkata Subbaiah, K J Saji, and A Tiwari. Atomically Thin MoS_2: A Versatile Nongraphene 2D Material. *Advanced Functional Materials*, 26:2046–2069, 2016.

[74] A Castellanos-Gomez, M Poot, G A Steele, H S J van der Zant, N Agrait, and G Rubio-Bollinger. Elastic Properties of Freely Suspended MoS_2 Nanosheets. *Advanced Materials*, 24(6):772–775, Jan 2012.

[75] A Splendiani, L Sun, Y Zhang, T Li, J Kim, C-Y Chim, G Galli, and F Wang. Emerging Photoluminescence in Monolayer MoS_2. *Nano Letters*, 10(4):1271–1275, 2010.

[76] M S Ullah, A H Bin Yousuf, A D Es-Sakhi, and M H Chowdhury. Analysis of Optical and Electronic Properties of MoS_2 for Optoelectronics and FET Applications. *AIP Conference Proceedings*, 1957(020001), 2018.

[77] D Kong, Y Chen, J J Cha, Q Zhang, J G Analytis, K Lai, Z Liu, S S Hong, K J Koski, S-K Mo, Z Hussain, I R Fisher, Z-X Shen, and Y Cui. Ambipolar field effect in the ternary topological insulator $(Bi_xSb_{1-x})_2Te_3$ by composition tuning. *Nature Nanotechnology*, 6:705–709, Nov 2011.

[78] Y Pan, Q-Z Wang, A L Yeats, T Pillsbury, T C Flanagan, A Richardella, H Zhang, D D Awschalom, C-X Liu, and N Samarth. Helicity dependent photocurrent in electrically gated $(Bi_{1-x}Sb_x)Te_3$ Thin Films. *Reports on Progress in Physics*, 8(1037), Oct 2017.

[79] P Chen, N Li, X Chen, W-J Ong, and X Zhao. The rising star of 2D black phosphorus beyond graphene: synthesis, properties and electronic applications. *2D Materials*, 5(1), Oct 2017.

[80] G Cheng, M Tomczyk, A B Tacla, H Lee, S Lu, J P Veazey, M Huang, P Irvin, S Ryu,

C-B Eom, A Daley, D Pekker, and J Levy. Tunable Electron-Electron Interactions in $LaAlO_3/SrTiO_3$ Nanostructures. *Physical Review X*, 6(041042), Dec 2016.

[81] Y-Y Pai, A Tylan-Tyler, P Irvin, and P Levy. Physics of $SrTiO_3$-based heterostructures and nanostructures: a review. *Reports on Progress in Physics*, 81(036503), Feb 2018.

[82] N Y Chan, M Zhao, N Wang, K Au, J Wang, L W H Chan, and J Dai. Palladium Nanoparticle Enhanced Giant Photoresponse at $LaAlO_3/SrTiO_3$ Two-Dimensional Electron Gas Heterostructures. *ACS Nano*, 7(10):8673–8679, 2013.

[83] K A Brown, S He, D J Eichelsdoerfer, M Huang, I Levy, H Lee, S Ryu, P Irvin, J Mendez-Arroyo, C-B Eom, C A Mirkin, and J Levy. Giant conductivity switching of $LaAlO_3/SrTiO_3$ heterointerfaces governed by surface protonation. *Nature Communications*, 7(10681), 2016.

[84] A D Caviglia, S Gariglio, N Reyren, D Jaccard, T Schneider, M Gabay, S Thiel, G Hammerl, J Mannhart, and J-M Triscone. Electric field control of the $LaAlO_3/SrTiO_3$ interface ground state. *Nature*, 456(7222):624–627, Dec 2008.

[85] D Huang and J E Hoffman. Monolayer FeSe on $SrTiO_3$. *Annual Review of Condensed Matter Physics*, 8(17):1–26, Feb 2017.

[86] S Tan, Y Zhang, M Xia, Z Ye, F Chen, X Xie, R Peng, D Xu, Q Fan, H Xu, J Jiang, T Zhang, X Lai, T Xiang, J Hu, B Xie, and D Feng. Interface-induced superconductivity and strain-dependent spin density waves in $FeSe/SrTiO_3$ thin films. *Nature Materials*, 12:624–640, May 2013.

[87] B Lei, J H Cui, Z J Xiang, C Shang, N Z Wang, G J Ye, X G Liu, T Wu, Z Sun, and X H Chen. Evolution of High-Temperature Superconductivity from a Low-T_c Phase Tuned by Carrier Concentration in FeSe Thin Flakes. *Physical Review Letters*, 116(077002), Feb 2016.

[88] T Liu, C Han, D Xiang, K Han, A Ariando, and W Chen. Optically Controllable 2D Material/Complex Oxide Heterointerface. *Advanced Science*, 7(21), Aug 2020.

[89] G R Bhimanapati, Z Lin, V Meunier, Y Jung, J Cha, S Das, D Xiao, Y Son, M S Strano, V R Cooper, L Liang, S G Louie, E Ringe, W Zhou, S S Kim, R R Naik, B G Sumpter, H Terrones, F Xia, Y Wang, J Zhu, D Akinwande, N Alem, J A Schuller, R E Schaak, M Terrones, and J A Robinson. Recent Advances in Two-Dimensional Materials beyond Graphene. *ACS Nano*, 9(12):11509–11539, Dec 2015.

[90] Z Lin, A McCreary, N Briggs, S Subramanian, K Zhang, Y Sun, X Li, N Borys, H Yuan, and S K Fullerton-Shirey. 2D materials advances: from large scale synthesis and controlled heterostructures to improved characterization techniques, defects and applications. *2D Materials*, 3(4):042001, Dec 2016.

[91] Y Lui, Z Qiu, A Carvalho, Y Bao, H Xu, S J R Tan, W Liu, A H Castro Neto, K P Loh, and J Lu. Gate-Tunable Giant Stark Effect in Few-Layer Black Phosphorus. *Nano Letters*, 17(3):1970–1977, 2017.

[92] F Liu, C Zhu, L You, S-J Liang, S Zheng, J Zhou, Q Fu, Y He, Q Zeng, H J Fan, L K Ang, J Wang, and Z Liu. 2D Black Phosphorus/SrTiO3-Based Programmable Photoconductive Switch. *Advanced Materials*, 28(35):7768–7773, Jul 2016.

[93] M Yang, C Yan, Y Ma, L Li, and C Cen. Light induced non-volatile switching of superconductivity in single layer FeSe on $SrTiO_3$ substrate. *Nature Communications*, 10(85), Jan 2019.

[94] M Capizzi and A Frova. Optical Gap of Strontium Titanate (Deviation from Urbach Tail Behavior). *Physical Review Letters*, 25(18):1298–1302, Jun 1970.

[95] A L Yeats, P J Mintun, Y Pan, A Richardella, B B Buckley, N Samarth, and D D Awschalom. Local optical control of ferromagnetism and chemical potential in a topo-

logical insulator. *Proceedings of the National Academy of Sciences*, 114(39):10379–10383, 2017.

[96] Asylum Research. Version 16, Revision: A-2053; Dated 09/28/2018.

[97] W Melitz, J Shen, A C Kummel, and S Lee. Kelvin probe force microscopy and its application. *Surface Science Reports*, 66(1):1–27, Jan 2011.

[98] S Vahabi, B H Salman, and A Javanmard. Atomic Force Microscopy Application in Biological Research: A Review Study. *Iran Journal of Medical Sciences*, 38(2):76–83, Jun 2013.

[99] M Salerno and S Dante. Scanning Kelvin Probe Microscopy: Challenges and Perspectives towards Increased Application on Biomaterials and Biological Samples. *Materials*, 11(6):951, Jun 2018.

[100] H-J Butt, B Cappella, and M Kappl. Force measurements with the atomic force microscope: Technique, interpretation and applications. *Surface Science Reports*, 59(1-6):1–152, 2005.

[101] S Maghsoudy-Louyeh, M Kropf, and B R Tittmann. Review of Progress in Atomic Force Microscopy. *The Open Neuroimaging Journal*, 12(Suppl 1: M3), Dec 2018.

[102] S Hudlet, M Saint Jean, B Roulet, J Berger, and C Guthmann. Electrostatic forces between metallic tip and semiconductor surfaces. *Journal of Applied Physics*, 77(3308), 1995.

[103] E Bonaccurso, F Schonfeld, and H-J Butt. Electrostatic forces acting on tip and cantilever in atomic force microscopy. *Physical Review B*, 74(085413), 2006.

[104] L Polak and R J Wijngaarden. Two competing interpretations of Kelvin probe force microscopy on semiconductors put to test. *Physical Review B*, 93(195320), 2016.

[105] K Kang, K-H Lee, Y Han, H Gao, S Xie, D A Muller, and J Park. Layer-by-layer assembly of two-dimensional materials into wafer-scale heterostructures. *Nature*, 550:229–233, 2017.

[106] B B Zhou, P C Jerger, K-H Lee, M Fukami, F Mujid, J Park, and D D Awschalom. Spatiotemporal Mapping of a Photocurrent Vortex in Monolayer MoS_2 Using Diamond Quantum Sensors. *Physical Review X*, 10(011003), Jan 2020.

[107] H Wang, Y Wu, C Cong, J Shang, and T Yu. Hysteresis of Electronic Transport in Graphene Transistors. *ACS Nano*, 4(12):7221–7228, 2010.

[108] J Zaumseil and H Sirringhaus. Electron and Ambipolar Transport in Organic Field-Effect Transistors. *Chem Rev*, 107:1296–1323, 2007.

[109] B W H Baugher, H O H Churchill, Y Yang, and P Jarillo-Herrero. Intrinsic Electronic Transport Properties of High Quality Monolayer and Bilayer MoS_2. *Nano Letters*, 13(9):4212–4216, 2013.

[110] S Ghatak, A N Pal, and A Ghosh. Nature of Electronic States in Atomically Thin MoS_2 Field-Effect Transistors. *ACS Nano*, 5(10):7707–7712, 2011.

[111] D-H Kang, M-S Kim, J Shim, J Jeon, H-Y Park, W-S Jung, H-Y Yu, C-H Pang, S Lee, and J-H Park. High-Performance Transition Metal Dichalcogenide Photodetectors Enhanced by Self-Assembled Monolayer Doping. *Advanced Functional Materials*, 25(27):4219–4227, 2015.

[112] O Lopez-Sanchez, D Lembke, M Kayci, A Radenovic, and A Kis. Ultrasensitive photodetectors based on monolayer MoS_2. *Nature Nanotechnology*, 8:497–501, 2013.

[113] H Li, C Liu, Y Zhang, C Qi, G Ma, T Wang, S Dong, and M Huo. Modulation of 1MeV electron irradiation on ultraviolet response in MoS_2 FET. *Nanotechnology*, 32(475205), 2021.

[114] K Cho, T-Y Kim, W Park, J Park, D Kim, J Jang, H Jeong, S Hong, and T Lee. Gate-bias stress-dependent photoconductive characteristics of multi-layer MoS_2 field-effect transistors. *Nanotechnology*, 25(155201), 2014.

[115] User Instruction Manual. Manual found online at https://www.graphenea.com/products/easy-transfer-monolayer-graphene-on-polymer-film-1-cm-x-1-cm ; accessed: 2021-09-19.

[116] T Bieger, J Maier, and R Waser. An Optical In-Situ Method to Study Redox-Kinetics in $SrTiO_3$. *Phys Chem*, 97(9):1098–1104, 1993.

[117] S M Song, J K Park, O J Sul, and B J Cho. Determination of Work Function of Graphene under a Metal Electrode and Its Role in Contact Resistance. *Nano Letters*, 12(8):3887–3892, 2012.

[118] K Suzuki and K Kijima. Optical Band Gap of Barium Titanate Nanoparticles Prepared by RF-Plasma Chemical Vapor Deposition. *Japanese Journal of Applied Physics*, 44(4):2081–2082, 2005.

[119] S Roberts. Dielectric and Piezoelectric Properties of Barium Titanate. *Physical Review*, 71(12):890–895, 1947.

[120] L B Kong, W Zhu, and O K Tan. Preparation and characterization of $Pb(Zr_{0.52}Ti_{0.48})O_3$ ceramics from high-energy ball milling powders. *Materials Letters*, 42(4):232–239, Feb 2000.

[121] V Batra, S Kotru, M Varagas, and C V Ramana. Optical constants and band gap determination of $Pb_{0.95}La_{0.05}Zr_{0.54}Ti_{0.46}O_3$ thin films using spectroscopic ellipsometry and UV-visible spectroscopy. *Optical Materials*, 49:123–128, Nov 2015.

[122] M C Rodriguez-Aranda, F Calderon-Pinar, M A Hernandez-Landaverde, J Heiras,

R Zamorano-Ulloa, D Ramirez-Rosales, and J M Yanez-Limon. Photoluminescence of sol-gel synthesized PZT powders. *Journal of Luminescence*, 179:280–286, 2016.

[123] S Samanta, V Sankaranarayanan, and K Sethupathi. Band gap, piezoelectricity and temperature dependence of differential permittivity and energy storage density of PZT with different Zr/Ti ratios. *Vacuum*, 156:456–462, 2018.

[124] Z Gubinyi, C Batur, A Sayir, and F Dynys. Electrical properties of PZT piezoelectric ceramic at high temperatures. *Journal of Electroceramics*, 20:95–105, 2008.

[125] B Amorim, A Cortijo, F de Juan, A G Grushin, F Guinea, A Gutierrez-Rubio, H Ochoa, V Parente, R Roldan, P San-Jose, J Schiefele, M Sturla, and M A H Vozmediano. Novel effects of strains in graphene and other two dimensional materials. *Physics Reports*, 617:1–54, Mar 2016.

[126] Y Zhang, TT Tang, C Girit, Z Hao, M C Martin, A Zettl, M F Crommie, Y R Shen, and F Wang. Direct observation of a widely tunable bandgap in bilayer graphene. *Nature*, 549:820–823, Jun 2009.

[127] M F Craciun, S Russo, M Yamamoto, J B Oostinga, A F Morpurgo, and S Tarucha. Trilayer graphene is a semimetal with a gate-tunable band overlap. *Nature Nanotechnology*, 4:383–388, 2009.

[128] C H Lui, Z Li, K F Mak, E Capelluti, and T F Heinz. Observation of an electrically tunable band gap in trilayer graphene. *Nature Physics*, 7:944–947, 2011.

[129] J E Padilha, A Fazzio, and A J R da Silva. van der Waals Heterostructure of Phosphorene and Graphene: Tuning the Schottky Barrier and Doping by Electrostatic Gating. *Physical Review Letters*, 114(066803), Feb 2015.

[130] A Dankert and S P Dash. Electrical gate control of spin current in van der Waals heterostructures at room temperature. *Nature Communications*, 8(16093), 2017.